



**NATIONAL TECHNICAL
UNIVERSITY OF ATHENS**
INTERDISCIPLINARY INTERDEPARTMENTAL
POSTGRADUATE PROGRAM (IIPP)

“MATERIALS SCIENCE AND TECHNOLOGY”

**“COMPARATIVE STUDY OF STRUCTURE
AND PROPERTIES OF THERMAL SPRAY
COATINGS USING CONVENTIONAL AND
NANOSTRUCTURED HYDROXYAPATITE
POWDER, FOR APPLICATIONS IN
MEDICAL IMPLANTS”**

MASTER THESIS

PARASKEVI A. GKOMOZA

Graduate Mechanical Engineer at UTH

SUPERVISOR:

D. PANTELIS

Professor at NTUA

Athens, June 2017



**NATIONAL TECHNICAL
UNIVERSITY OF ATHENS**
INTERDISCIPLINARY INTERDEPARTMENTAL
POSTGRADUATE PROGRAM (IIPP)

“MATERIALS SCIENCE AND TECHNOLOGY”

**“COMPARATIVE STUDY OF STRUCTURE
AND PROPERTIES OF THERMAL SPRAY
COATINGS USING CONVENTIONAL AND
NANOSTRUCTURED HYDROXYAPATITE
POWDER, FOR APPLICATIONS IN
MEDICAL IMPLANTS”**

MASTER THESIS

PARASKEVI A. GKOMOZA

Graduate Mechanical Engineer at UTH

THREE-MEMBER COMMITTEE OF INQUIRY:

D. PANTELIS, Professor at NTUA

A. TSETSEKOY, Professor at NTUA

K. KORDATOS, Associate Professor at NTUA

Athens, June 2017

ACKNOWLEDGEMENTS

This thesis was submitted to fulfill part of the requirements for the acquisition of M.Sc. degree in “Materials Science and Technology” and it was elaborated at the Shipbuilding Technology Laboratory of the School of Naval Architecture and Marine Engineering, National Technical University of Athens, under the supervision of Professor D. Pantelis. With the end of my diplomatic work, I would like to thank the people who contributed to its completion. First of all, I would like to thank Mr. D. Pantelis, Professor at NTUA, for the opportunity he gave me to deal with this subject, as well as the confidence he showed me throughout the diploma thesis.

In addition, I would like to thank Mr. M. Vardavoulias, Managing Director at PYROGENESIS SA, for providing the samples to be examined and also his useful observations upon the results.

I would like to offer special thanks to Mrs. Ch. Sarafoglou, Dr. Mechanical Engineer at NTUA, for her patience during the time spent for examination of the samples via SEM and for her helpful suggestions regarding management of the specimens.

I am particularly grateful to Mrs. D. Tsiourva, Mr. A. Markoulis and Mr. Ch. Xanthis, Technical Staff of the Shipbuilding Technology Laboratory, NTUA and Mr. P. Karakizis, Candidate Doctor at NTUA, for the very good cooperation and the pleasant working environment.

I wish to acknowledge the help provided by Mrs. A. Karamperi, member of the Laboratory Teaching Staff of the Department of Chemical Sciences, School of Chemical Engineering, NTUA, for her help throughout X-ray diffraction analysis of the samples.

I wish to thank Mr. A. Karagiannis-Mpakolas, Assistant Professor at the Department of Materials Science and Engineering, School of Chemical Engineering, NTUA, for his assistance regarding the process of mercury porosimetry.

I am particularly grateful to Mrs. A. Tsetsekou, Professor at School of Mining and Metallurgical Engineering, NTUA, for her permission to use equipment located at the Laboratory of Physical Metallurgy, Mrs. F. Petrakli, Candidate Doctor at NTUA, for her valuable aid during gold sputtering and also, fellow student and friend Mrs. M. Panou, Postgraduate Student at the Laboratory of Physical Metallurgy, NTUA, for her contribution through SBF preparation.

Finally, I would like to express my very great appreciation to my family and friends for their genuine concern and constant support in life and of course, in the course of the diplomatic work.

Paraskevi A. Gkomoza

ABSTRACT

The aim of this paper is to study and compare the structure and properties of thermal spray coatings prepared with conventional and nanostructured hydroxyapatite powder, regarding their use in medical implants. More specifically, four specimens were prepared via atmospheric plasma spray process (APS) at PYROGENESIS SA. Two kinds of feedstock material were employed for the spray process, namely, commercial XPT-D-703 hydroxyapatite powder for half the samples and nanostructured PYRO 4 hydroxyapatite powder, which was mechanically treated on the premises of PYROGENESIS SA, for the remaining samples. The substrate of all the samples is stainless steel 304. Finally, the plasma spray parameters were altered for two out of the four specimens, each with a coating made of a different type of powder, in order for a greater amount of porosity to be achieved.

Subsequently, the percentage of coating porosity, as well as the mean pore radius were evaluated by two different methods; MIPAR image analysis program and mercury porosimetry, at the Department of Materials Science and Engineering, School of Chemical Engineering, NTUA, by Mr. A. Karagiannis-Mpakolas. Image analysis provides information regarding the "closed" porosity content, which is enclosed within the body of the coating, while mercury porosimetry measures the "open" porosity content, which is present on the surface of the coating. Both methods showed that Specimen No. 4 had the highest percentage of total porosity, although none of the four specimens owned neither sufficient porosity, nor desirable pore size, in order to meet the required specifications for immediate use in medical implants.

In addition, the specimens were examined with regard to their microstructure, roughness, crystallinity and microhardness, at the Shipbuilding Technology Laboratory, School of Naval Architecture and Marine Engineering, NTUA. Specimen No. 4 is characterized by the highest roughness values, which comes in agreement with the roughness values that accompany medical implants already accommodated on the market. At the same time, it is observed that the specific specimen retained, after spraying, the crystallinity of the corresponding hydroxyapatite powder prior to spraying, as revealed by the intensity peaks of the spectra resulted from X-ray diffraction, acquired with the aid of Mrs. A. Karamperi, at the Department of Chemical Sciences, School of Chemical Engineering, NTUA. The measured microhardness values were the same for all the samples, except for a minimum deviation.

Furthermore, *in vitro* bioactivity test was performed on the hydroxyapatite coatings, by immersion of the specimens, for seven consecutive days, into a solution that emulates the composition and properties of somatic fluids (SBF solution), which was prepared at the Laboratory of Physical Metallurgy, School of Mining and Metallurgical Engineering, NTUA. Subsequently, the samples were retrieved from the solution and examined by scanning electron microscopy, at the Shipbuilding Technology Laboratory, School of Naval Architecture and Marine Engineering, NTUA, with the assistance of Mrs. Ch. Sarafoglou, when the formation of apatite phase was detected on the surface of all the specimens.

Finally, based on the adhesion tests that were carried out in PROGENESIS SA, as well as through observation of the microstructure via optical and also, scanning electron microscopy, it is revealed that the samples coming from spraying of the nanostructured PYRO 4 hydroxyapatite powder, present the most satisfying adhesion of the coating onto the underlying substrate.

ΠΕΡΙΛΗΨΗ

Αντικείμενο της παρούσας εργασίας αποτελεί η μελέτη της δομής και των ιδιοτήτων επικαλύψεων θερμικών ψεκασμών συμβατικού και νανοδομημένου υδροξυαπατίτη, με απώτερο σκοπό τη χρήση του σε ιατρικά εμφυτεύματα. Συγκεκριμένα, παρήχθησαν τέσσερα δοκίμια με την τεχνική ψεκασμού με τόξο πλάσματος στις εγκαταστάσεις της ΠΥΡΟΓΕΝΕΣΙΣ Α.Β.Ε.Ε.. Στα δύο εκ των τεσσάρων δοκιμών το υλικό που χρησιμοποιήθηκε για τη δημιουργία του επιστρώματος ήταν εμπορική σκόνη υδροξυαπατίτη ΧΡΤ-D-703, ενώ για τα υπόλοιπα χρησιμοποιήθηκε νανοδομημένη σκόνη υδροξυαπατίτη ΡΥΡΟ 4, η οποία έχει δεχθεί μηχανική κατεργασία στην ΠΥΡΟΓΕΝΕΣΙΣ Α.Β.Ε.Ε.. Το υπόστρωμα όλων των δοκιμών είναι ανοξείδωτος χάλυβας 304. Τέλος, οι συνθήκες ψεκασμού για τα δύο εκ των τεσσάρων δοκιμών, το κάθε ένα με επίστρωμα κατασκευασμένο από διαφορετικό τύπο σκόνης, επιλέχθηκαν διαφορετικές με στόχο την επίτευξη μεγαλύτερου ποσοστού πορώδους.

Στη συνέχεια, το πορώδες της επίστρωσης, καθώς και η μέση ακτίνα των πόρων εκτιμήθηκαν με δύο διαφορετικές μεθόδους, την ανάλυση εικόνας με το πρόγραμμα MIPAR και την ποροσιμετρία υδραργύρου, η οποία πραγματοποιήθηκε στο εργαστήριο του Τομέα Επιστήμης και Τεχνικής των Υλικών της Σχολής Χημικών Μηχανικών Ε.Μ.Π., από τον κ. Α. Καραγιάννη-Μπακόλα. Η ανάλυση εικόνας παρέχει πληροφορίες για το «κλειστό» πορώδες στο εσωτερικό των επιστρωμάτων, ενώ η ποροσιμετρία υδραργύρου για το «ανοιχτό» πορώδες στην επιφάνεια των επιστρωμάτων. Και οι δύο μέθοδοι έδειξαν πως το δοκίμιο Νο. 4, κατείχε το υψηλότερο ποσοστό συνολικού πορώδους, ωστόσο κανένα από τα τέσσερα δοκίμια δεν κατείχε επαρκές πορώδες και ικανοποιητικό μέγεθος πόρων, ώστε να καλύψει τις απαιτούμενες προδιαγραφές για άμεση χρήση του σε ιατρικά εμφυτεύματα.

Συν τοις άλλοις, τα δοκίμια εξετάστηκαν ως προς τη μικροδομή τους, την τραχύτητα, την κρυσταλλικότητα και τη μικροσκληρότητά τους, στο Εργαστήριο Ναυπηγικής Τεχνολογίας της Σχολής Ναυπηγών Μηχανολόγων Μηχανικών Ε.Μ.Π.. Το δοκίμιο Νο. 4 χαρακτηρίστηκε από τη μεγαλύτερη τιμή τραχύτητας, η οποία έρχεται σε συμφωνία με την τιμή της τραχύτητας επιστρωμάτων ιατρικών εμφυτευμάτων που ήδη κυκλοφορούν στην αγορά. Παράλληλα, παρατηρείται πως το συγκεκριμένο δοκίμιο μετά τον ψεκασμό, διατήρησε σε πολύ μεγάλο βαθμό την κρυσταλλικότητα της αντίστοιχης σκόνης υδροξυαπατίτη πριν τον ψεκασμό, στα φάσματα που προέκυψαν από την περίθλαση ακτίνων Χ, η οποία έγινε με τη συμβολή της κα. Α. Καραμπέρη, στον Τομέα Χημικών Επιστημών της Σχολής Χημικών Μηχανικών Ε.Μ.Π.. Η τιμές της μικροσκληρότητας που μετρήθηκαν ήταν ίδιες για όλα τα δοκίμια, με ελάχιστη απόκλιση.

Ακόμη, πραγματοποιήθηκε έλεγχος βιοδραστικότητας *in vitro* της επίστρωσης των δοκιμών, μέσω της εμβάπτισής τους, για επτά συνεχόμενες μέρες, σε διάλυμα που προσομοιάζει τη σύσταση και τις ιδιότητες των σωματικών υγρών (SBF solution), το οποίο παρασκευάστηκε στο Εργαστήριο Μεταλλογνωσίας της Σχολής Μηχανικών Μεταλλείων-Μεταλλουργών Ε.Μ.Π.. Στη συνέχεια, τα δοκίμια εξετάστηκαν με το μικροσκόπιο σάρωσης ηλεκτρονίων, στο Εργαστήριο Ναυπηγικής Τεχνολογίας της Σχολής Ναυπηγών Μηχανολόγων Μηχανικών Ε.Μ.Π., με τη βοήθεια της κα. Χ. Σαράφου, οπότε και ανιχνεύθηκε ο σχηματισμός απατιτικής φάσης στην επιφάνεια και των τεσσάρων επιστρωμάτων.

Τέλος, με βάση τις δοκιμές πρόσφυσης που πραγματοποιήθηκαν στην ΠΥΡΟΓΕΝΕΣΙΣ Α.Β.Ε.Ε., αλλά και μέσω της παρατήρησης της μικροδομής στο οπτικό μικροσκόπιο και στο μικροσκόπιο σάρωσης ηλεκτρονίων, διαπιστώθηκε η αποτελεσματικότερη πρόσφυση του

επιστρώματος στο υπόστρωμα, των δοκιμίων που προήλθαν από ψεκασμό της νανοδομημένης σκόνης PYRO 4.

TABLE OF CONTENTS

ACKNOWLEDGEMENTS	2
ABSTRACT.....	3
ΠΕΡΙΛΗΨΗ	4
LIST OF FIGURES	10
LIST OF TABLES	16
CHAPTER 1: INTRODUCTION.....	17
CHAPTER 2: THEORETICAL PART.....	18
2.1) BIOMATERIALS	18
2.1.1) What is a biomaterial?.....	18
2.1.2) Types of biomaterials	19
2.1.2a) Metallic biomaterials	19
2.1.2b) Ceramic biomaterials.....	20
2.1.2c) Polymeric biomaterials	22
2.1.2d) Composite biomaterials.....	23
2.2) HYDROXYAPATITE (HAP).....	24
2.2.1) Chemical synthesis of hydroxyapatite	27
2.2.1a) Conventional chemical precipitation method.....	27
2.2.1b) Sol-gel synthesis method.....	28
2.2.1c) Hydrothermal method	28
2.2.2) Why nanosized HAP?.....	30
2.2.3) In vitro bioactivity investigation	31
2.3) THERMAL SPRAYING.....	32
2.3.1) Thermal spray techniques	32
2.3.1a) Atmospheric plasma spraying (APS)	33
2.3.1b) Vacuum plasma spraying (VPS).....	33
2.3.1c) High velocity oxygen fuel (HVOF) spraying	34
2.3.1d) Cold spraying.....	35
2.3.1e) Other coating techniques	36
2.3.2) Microstructural characteristics after thermal spraying	37
2.3.2a) Splat formation.....	37
2.3.2b) Porosity	38
2.3.2c) Surface roughness.....	39
2.4) Plasma spray problems.....	40
CHAPTER 3: EXPERIMENTAL PROCEDURES AND METHODOLOGY.....	42

3.1) Materials	43
3.1.1) Powders.....	43
3.1.1a) Optical microscope	43
3.1.1b) Scanning Electron Microscopy (SEM)	45
.....	45
3.1.1c) Energy Dispersive Spectroscopy (EDS)	48
3.1.2) Coatings and plasma spray parameters.....	51
3.2) Characterization of the coatings.....	52
3.2.1) Coating roughness.....	52
3.2.2) Preparation of the samples	52
3.2.3) Stereoscope.....	54
3.2.4) Optical microscope.....	55
3.2.5) Scanning Electron microscopy (SEM).....	55
3.2.6) X-ray Diffraction (XRD)	56
3.2.7) Microhardness.....	57
3.2.8) Porosimetry	57
3.2.8a) Image Analysis	57
3.2.8b) Mercury (Hg) Porosimetry	58
3.2.9) Bioactivity check.....	60
3.2.9a) Preparation of SBF	60
3.2.9b) In vitro test	60
3.2.10) Adhesion strength test	61
CHAPTER 4: RESULTS AND DISCUSSION	63
4.1) Coating roughness.....	63
4.2) Thickness measurements using stereoscope.....	64
4.3) Optical microscope.....	66
4.3.1) Specimen No. 1.....	66
4.3.2) Specimen No. 2.....	67
4.3.3) Further stereoscopical and microscopical examination of specimen No.1.....	69
4.3.4) Specimen No. 3.....	71
4.3.5) Specimen No. 4.....	73
4.4) Scanning Electron microscopy (SEM) and Energy Dispersive Spectroscopy (EDS).....	75
4.4.1) Cross-section related results before immersion into the SBF solution	75
4.4.1a) Specimen No. 1.....	75
4.4.1b) Specimen No. 2.....	77
4.4.1c) Specimen No. 3	79

4.4.1d) Specimen No. 4.....	81
4.4.2) Cross-section related results after immersion into the SBF solution (observation via stereoscope and optical microscope).....	83
4.4.2a) Specimen No. 1.....	83
4.4.2b) Specimen No. 2.....	84
4.4.2c) Specimen No. 3.....	85
4.4.2d) Specimen No. 4.....	86
4.4.3) Coating surface related results before immersion into the SBF solution.....	88
4.4.3a) Specimen No. 1.....	88
4.4.3b) Specimen No. 2.....	90
4.4.3c) Specimen No. 3.....	92
4.4.3d) Specimen No. 4.....	94
4.4.3e) Energy Dispersive Spectroscopy (EDS).....	96
4.4.4) Coating surface related results after immersion into the SBF solution	99
4.4.4a) Specimen No. 1.....	99
4.4.4b) Specimen No. 2.....	100
4.4.4c) Specimen No. 3.....	101
4.4.4d) Specimen No. 4.....	103
4.4.4e) Energy Dispersive Spectroscopy (EDS).....	104
4.4.5) Comparison and differences.....	107
4.5) X-ray Diffraction (XRD)	108
4.5.1) Powders.....	108
4.5.2) Specimens No. 1 and 2	110
4.5.3) Specimens No. 3 and 4	112
4.6) Microhardness.....	114
4.7) Porosity	115
4.7.1) Porosimetry via image analysis.....	115
4.7.1a) Specimen No. 1.....	115
4.7.1b) Specimen No. 2.....	118
4.7.1c) Specimen No. 3.....	121
4.7.1d) Specimen No. 4.....	124
4.7.2) Mercury (Hg) porosimetry	128
4.7.2a) Specimen No. 1.....	128
4.7.2b) Specimen No. 2.....	129
4.7.2c) Specimen No. 3.....	130
4.7.2d) Specimen No. 4.....	131

4.8) Adhesion strength test	133
CHAPTER 5: CONCLUSIONS.....	134
REFERENCES	136
CURRICULUM VITAE	141

LIST OF FIGURES

Figure 1: 3D printed custom-made prosthesis made of surgical grade titanium alloy [7].	19
Figure 2: Knee replacement femoral component made of zirconia ceramics [12].	21
Figure 3: Bioabsorbable implants that have potential applications throughout the spine [14].	22
Figure 4: Artificial hip joints made of a combination of materials [15].	23
Figure 5: Chemical composition of bone tissue [4].	24
Figure 6: Preferred rearrangement of hydroxyl groups within the hydroxyapatite structure (O = red, Ca = green, P = yellow, H = white) [23].	26
Figure 7: Depiction of the hole zones present throughout the collagen fiber bundle and the size and orientation of the carbonated hydroxyapatite crystals relative to the fibril direction [29].	30
Figure 8: Comparison of the processing temperatures and material transport velocities for the various thermal spray processes [43].	32
Figure 9: Principle of the atmospheric plasma spray process [48].	33
Figure 10: Schematic diagram of a controlled atmosphere plasma process [50].	34
Figure 11: Schematic diagram of High Velocity Oxygen Fuel (HVOF) spray with (a) gas fuel [52] and (b) liquid fuel [53].	35
Figure 12: Principle of a cold gas spray process [55].	36
Figure 13: Typical thermal spray splat structures. Flattened splat with rounded edges (upper left corner), disk-shape splat (first row in the middle) and flattened splat with elongated fringes (upper right corner). Depiction of the relative splats above, as seen from the side (middle row). Magnification of the side of the centre splat (bottom row) [49].	38
Figure 14: Thermal spray coating parameters involved in splat formation [63].	38
Figure 15: Thermal spray porosity forms [64].	39
Figure 16: Cross-section of thermally sprayed layer [77].	41
Figure 17: Twenty diameter measurements of the XPT-D-703 powder particles, via optical microscope.	43
Figure 18: Twenty diameter measurements of the PYRO 4 powder particles, via optical microscope.	44
Figure 19: (a), (b), (c) SEM images of commercial XPT-D-703 hydroxyapatite powder at different magnification, (d) agglomerated particles with diameter less than 10 μm , (e), (f) powder particle in different magnification, (g) cross-section of XPT-D-703 powder particles, (h) cross-section of particle with diameter of around 2 μm .	45
Figure 20: (a), (b), (c) SEM images of nanostructured hydroxyapatite powder at different magnification, (d) powder particle at larger magnification, (e), (f) surface of powder particle, (g), (h) cross-section of powder particles at different magnification.	47
Figure 21: EDS spot analysis on particle of commercial XPT-D-703 hydroxyapatite powder.	48
Figure 22: EDS spot analysis on particle of nanostructured PYRO 4 hydroxyapatite powder.	49
Figure 23: EDS spot analysis on particle of commercial XPT-D-703 hydroxyapatite powder.	49
Figure 24: EDS spot analysis on particle of nanostructured PYRO 4 hydroxyapatite powder.	50
Figure 25: Principle of the plasma spray process (photograph acquired at PYROGENESIS SA).	51
Figure 26: Surface roughness testers TR-100 (left) and TR-200 (right).	52
Figure 27: Struers Discotom-50.	52

Figure 28: (a) Sample No. 1 with XPT-D-703 and hydroxyapatite powder and (b) sample No. 2 with PYRO 4 hydroxyapatite powder, both before and after cut.	53
Figure 29: Sample No. 3 with XPT-D-703 hydroxyapatite powder (left) and sample No. 2 with PYRO 4 hydroxyapatite powder (right), both before and after cut.	53
Figure 30: Struers LaboForce-1 and LaboPol-5 semiautomated grinding machine with fixed holders.	54
Figure 31: Leica DMILM optical microscope (left) and Leica Mz6 stereoscope (right).....	55
Figure 32: Agar Auto Sputter Coater.	55
Figure 33: SEM JEOL JSM-6390 and EDS Oxford Instruments INCAx-sight elemental detector.	56
Figure 34: Brucker D8 Advance diffractometer.	56
Figure 35: Wolpert and Wilson Vickers tester.	57
Figure 36: Schematic representation of pores [83].	58
Figure 37: ThermoFinnigan Pascal 440 porosimeter.	59
Figure 38: Adhesion test according to ASTM 4541.	61
Figure 39: Preparation of the specimens before the adhesion test.	62
Figure 40: Adhesion test specimens after the adhesion test.	62
Figure 41: (a), (b) Sample No. 1 with XPT-D-703 hydroxyapatite powder at different magnifications, (b) five thickness measurements obtained by LAS image analysis are shown.	64
Figure 42: (a), (b) Sample No. 2 with PYRO 4 hydroxyapatite powder at different magnifications, (b) five thickness measurements obtained by LAS image analysis are shown.	64
Figure 43: (a), (b) Sample No. 3 with XPT-D-703 hydroxyapatite powder at different magnifications, (b) five thickness measurements obtained by LAS image analysis are shown.	65
Figure 44: (a), (b) Sample No. 4 with PYRO 4 hydroxyapatite powder at different magnifications, (b) five thickness measurements obtained by LAS image analysis are shown.	65
Figure 45: (a), (b) Sample No. 1 with XPT-D-703 hydroxyapatite powder at different magnification. Deep crack in the interface border, between the coating and the substrate, parallel to the substrate, is pointed by the arrow at both pictures.	66
Figure 46: Sample No. 1 with XPT-D-703 hydroxyapatite powder. Microcracks parallel and perpendicular to the interface line.	66
Figure 47: Sample No. 2 with PYRO 4 hydroxyapatite powder.	67
Figure 48: Sample No. 2 with PYRO 4 hydroxyapatite powder. Visible microcrack in the coating parallel to the interface, near the interface border.	67
Figure 49: Sample No. 2 with PYRO 4 hydroxyapatite powder. Visible microcrack in the coating parallel to the interface.	68
Figure 50: (a), (b) Stereoscopical images of sample No. 1 with XPT-D-703 hydroxyapatite powder at different magnification, (b) with thickness measurements.	69
Figure 51: Image acquired via optical microscope of the sample No. 1 with XPT-D-703 hydroxyapatite powder. Thin crack in the interface border, between the coating and the substrate, parallel to the substrate.	70
Figure 52: Image acquired via optical microscope of the sample No. 1 with XPT-D-703 hydroxyapatite powder. Thin crack in the interface border, between the coating and the substrate, parallel to the substrate.	70

Figure 53: Sample No. 3 with XPT-D-703 hydroxyapatite powder. Microcracks perpendicular to the coating-substrate interface are visible (right-side arrow). No visible crack in the interface border, between the coating and the substrate (bottom-left arrow). 71

Figure 54: Sample No. 3 with XPT-D-703 hydroxyapatite powder. Microcracks perpendicular to the coating-substrate interface are visible (right-side arrows). 71

Figure 55: Sample No. 3 with XPT-D-703 hydroxyapatite powder. Microcracks perpendicular to the coating-substrate interface are visible (right-side arrow). No visible crack in the interface border, between the coating and the substrate (bottom-left arrow). 72

Figure 56: Sample No. 4 with PYRO 4 hydroxyapatite powder. No visible crack in the interface border, between the coating and the substrate (bottom-left arrow). 73

Figure 57: Sample No. 4 with PYRO 4 hydroxyapatite powder. Microcracks perpendicular to the coating-substrate interface are visible (right-side arrow). No visible crack in the interface border, between the coating and the substrate (bottom-left arrow). Clusters of small pores (white circles) in the coating. 73

Figure 58: Sample No. 4 with PYRO 4 hydroxyapatite powder. Microcracks perpendicular to the coating-substrate interface are visible (right-side arrow). Cluster of small pores (white circle) in the coating. 74

Figure 59: SEM images of cross-section of specimen No. 1, (a) overall cross-section at low magnification, (b) porosity content tends to gather at the upper part of the coating, (c) impurities accumulated at the coating-substrate interface, (d) part of the coating with fair adherence, pores and microcracks, (e) lamellar microstructure and fine microcracks perpendicular to the coating-substrate interface..... 75

Figure 60: SEM images of cross-section of specimen No. 2, (a) overall cross-section at low magnification, (b) consistent coating with no presence of microcracks, lamellar microstructure, (c) and (d) zone of different phase at the coating-substrate interface, (e) ribbon-like regions, large pore due to pullout of unmelted particle core. 77

Figure 61: SEM images of cross-section of specimen No. 3, (a) overall cross-section at low magnification, (b) impurities dispersed near or onto the coating-substrate interface, (c) large pore due to pullout of unmelted particle core, (d) lamellar microstructure, voids and microcracks perpendicular to the coating-substrate interface..... 79

Figure 62: SEM images of cross-section of specimen No. 4, (a) overall cross-section at low magnification, (b) consistent coating with no presence of microcracks, large pore due to pullout of unmelted particle core, (c) zone of different phase at the coating-substrate interface, (d) microporosity, (e) and (f) ribbon-like regions. 81

Figure 63: Cross-section of specimen No. 1, after immersion into the SBF solution. Images acquired via stereoscope with thickness measurements included (top row) and via optical microscope at different magnifications (middle and bottom row). 83

Figure 64: Cross-section of specimen No. 2, after immersion into the SBF solution. Images acquired via stereoscope with thickness measurements included (top row) and via optical microscope at different magnifications (middle and bottom row). 84

Figure 65: Cross-section of specimen No. 3, after immersion into the SBF solution. Images acquired via stereoscope with thickness measurements included (top row) and via optical microscope at different magnifications (middle and bottom row). 85

Figure 66: Cross-section of specimen No. 4, after immersion into the SBF solution. Images acquired via stereoscope with thickness measurements included (top row) and via optical microscope at different magnifications (middle and bottom row). 86

Figure 67: SEM images of the coating surface of specimen No. 1, prior to immersion into the SBF solution at different magnifications, (a) porous microstructure, dispersed unmolten and

semi-molten particles, (b) semi-molten particle with molten shell and unmelted core, (c) and (d) well-flattened splats with rounded fringes, (e) microstructure of a partially molten particle.88

Figure 68: SEM images of the coating surface of specimen No. 2, prior to immersion into SBF solution at different magnifications, (a) porous microstructure, dispersed unmolten and semi-molten particles, (b) semi-molten particle with molten shell and unmelted core, (c) and (d) well-flattened splats with rounded fringes, (d) and (e) microstructure of a partially molten particle.90

Figure 69: SEM images of the coating surface of specimen No. 3, prior to immersion into SBF solution at different magnifications, (a) well-flattened splats that form glassy surfaces, (b) zoom-in of an (a) region, (c) splats with elongated fringes, presence of microcracks, (d) shattered molten and resolidified particles, (e) and (f) interior of an open pore.92

Figure 70: SEM images of the coating surface of specimen No. 4, prior to immersion into SBF solution at different magnifications, (a) porous coating, fine microcrack within flattened splats, (b) glassy surfaces and unmelted or semi-molten particles, (c) splat with rounded fringes, (d) porous structure of partially molten powder particle, (e) open pore, (f) unmelted particle, semi-molten particle covered by flattened splat.94

Figure 71: EDS spot analysis on coating of specimen No. 1, before immersion into the SBF solution.96

Figure 72: EDS spot analysis on coating of specimen No. 2, before immersion into the SBF solution.96

Figure 73: EDS spot analysis on coating of specimen No. 3, before immersion into the SBF solution.97

Figure 74: EDS spot analysis on coating of specimen No. 4, before immersion into the SBF solution.97

Figure 75: SEM images of the coating surface of specimen No. 1, after immersion into the SBF solution at different magnifications, (a) porous and inhomogeneous coating, (b) glassy surface with rectangular shape, (c) glassy surface with undefined shape, (d) spheroid nanosized HAP particles.99

Figure 76: SEM images of the coating surface of specimen No. 2, after immersion into SBF solution at different magnifications, (a) salt crystals, (b) apatite formation, (c) and (d) nanosized apatite particle agglomerations.100

Figure 77: SEM image of the coating surface of specimen No. 3, after immersion into SBF solution at low magnification. Both the area that reacted within the solution (upper) and the undisturbed area (lower) are shown.101

Figure 78: SEM images of the coating surface of specimen No. 3, after immersion into SBF solution. The images refer to the area of the specimen that did not react with the solution. (a) inhomogeneous coating with the form of scaffold, (b) interior of an open pore.101

Figure 79: SEM images of the coating surface of specimen No. 3, after immersion into the SBF solution at different magnifications. The images refer to the area of the specimen that reacted with the solution. (a) and (b) salt residues amongst apatite formations.....102

Figure 80: SEM images of the coating surface of specimen No. 4, after immersion into SBF solution at different magnifications.103

Figure 81: EDS spot analysis on coating specimen No. 1, after immersion into the SBF solution.104

Figure 82: EDS spot analysis on coating of specimen No. 2, after immersion into the SBF solution.105

Figure 83: EDS spot analysis on coating of specimen No. 4, after immersion into the SF solution.	105
Figure 84: Coating surface of specimen No. 1 (a) before and (b) after immersion into the SBF solution.	107
Figure 85: XRD spectra of (a) commercial XPT-D-703 hydroxyapatite powder and PYRO 4 hydroxyapatite powder. In both spectra the diffraction patterns of synthetic hydroxyapatite (red line) is also provided.	108
Figure 86: XRD spectra of (a) commercial XPT-D-703 hydroxyapatite coating and (b) PYRO 4 hydroxyapatite coating (black lines). All of the phases identified are also depicted (synthetic HAP= red, calcium phosphate- α = green, tetracalcium phosphate= purple, calcium oxide=brown).	110
Figure 87: Aggregated graph of hydroxyapatite powder and its respective hydroxyapatite coating for (a) commercial XPT-D-703 powder and (b) PYRO 4 powder.	111
Figure 88: XRD spectra of commercial XPT-D-703 hydroxyapatite coating (black lines). All of the phases identified are also depicted (synthetic HAP= red, whitlockite= blue, calcium phosphate- α =light green, calcium oxide= brown, calcium phosphate- β = green, tetracalcium phosphate= purple, calcium hydride= orange).	112
Figure 89: XRD spectra of PYRO 4 hydroxyapatite coating (black lines). All of the phases identified are also depicted (synthetic HAP= red, tetracalcium phosphate= purple, calcium oxide= brown, calcium phosphate- β = blue, whitlockite= green).	113
Figure 90: Original photo of sample No. 1 with XPT-D-703 hydroxyapatite powder acquired by the optical microscope.	115
Figure 91: Cropped image of the original photo for ease of processing, (b) with pore outline, (c) on black and white display.	115
Figure 92: Original photo of sample No. 1 with XPT-D-703 hydroxyapatite powder acquired by the optical microscope.	116
Figure 93: (a) Cropped image of the original photo for ease of processing, (b) with pore outline, (c) on black and white display.	116
Figure 94: Original photo of sample No. 1 with XPT-D-703 hydroxyapatite powder acquired by the optical microscope.	117
Figure 95: (a) Cropped image of the original photo for ease of processing, (b) with pore outline, (c) on black and white display.	117
Figure 96: Original photo of sample No. 2 with PYRO 4 hydroxyapatite powder acquired by the optical microscope.	118
Figure 97: (a) Cropped image of the original photo for ease of processing, (b) with pore outline, (c) on black and white display.	118
Figure 98: Original photo of sample No. 2 with PYRO 4 hydroxyapatite powder acquired by the optical microscope.	119
Figure 99: (a) Cropped image of the original photo for ease of processing, (b) with pore outline, (c) on black and white display.	119
Figure 100: Original photo of sample No. 2 with PYRO 4 hydroxyapatite powder acquired by the optical microscope.	120
Figure 101: (a) Cropped image of the original photo for ease of processing, (b) with pore outline, (c) on black and white display.	120
Figure 102: Original photo of sample No. 3 with XPT-D-703 hydroxyapatite powder acquired by the optical microscope.	121
Figure 103: Cropped image of the original photo for ease of processing, (b) with pore outline, (c) on black and white display.	121

Figure 104: Original photo of sample No. 3 with XPT-D-703 hydroxyapatite powder acquire by the optical microscope.	122
Figure 105: (a) Cropped image of the original photo for ease of processing, (b) with pore outline, (c) on black and white display.	122
Figure 106: Original photo of sample No. 3 with XPT-D-703 hydroxyapatite powder acquired by the optical microscope.	123
Figure 107: (a) Cropped image of the original photo for ease of processing, (b) with pore outline, (c) on black and white display.	123
Figure 108: Original photo of sample No. 4 with PYRO 4 hydroxyapatite powder acquired by the optical microscope.	124
Figure 109: (a) Cropped image of the original photo for ease of processing, (b) with pore outline, (c) on black and white display.	124
Figure 110: Original photo of sample No. 4 with PYRO 4 hydroxyapatite powder acquired by the optical microscope.	125
Figure 111: (a) Cropped image of the original photo for ease of processing, (b) with pore outline, (c) on black and white display.	125
Figure 112: Original photo of sample No. 4 with PYRO 4 hydroxyapatite powder acquired by the optical microscope.	126
Figure 113: (a) Cropped image of the original photo for ease of processing, (b) with pore outline, (c) on black and white display.	126
Figure 114: Pore size distribution in commercial XPT-D-703 hydroxyapatite coating.	128
Figure 115: Pore size distribution in PYRO 4 hydroxyapatite coating.	129
Figure 116: Pore size distribution in commercial XPT-D-703 hydroxyapatite coating.	130
Figure 117: Pore size distribution in PYRO 4 hydroxyapatite coating.	131

LIST OF TABLES

Table 1: Ceramics used in biomedical applications [9].	20
Table 2: Comparative composition, crystallographic and mechanical properties of human enamel, bone and HAP [8].	25
Table 3: Comparison of the different methods for the preparation of HAP nanoparticles [25], [26].	29
Table 4: Compositions of Kokubo solution and Hank's balanced salt solution. The ingredients appear in chronological order of preparation [38].	31
Table 5: Ion concentration of SBFs and relative ion concentration of human blood plasma [40].	31
Table 6: Average diameter of powder particles (in μm).	44
Table 7: Type of powder and divergence of the plasma spray parameters for each sample.	51
Table 8: Dimensions of the samples before and after cut.	53
Table 9: Quantities of the reactants required for preparation of the SBF solution.	60
Table 10: Roughness parameters Ra, Rz and Rmax.	63
Table 11: Average coating thickness of the samples.	65
Table 12: Average coating thickness (in mm) of the samples, after immersion into the SBF solution.	87
Table 13: Dominant elements detected (mean weight percentages) on the coating of each specimen, before their immersion into the SBF solution.	98
Table 14: Dominant elements detected (mean weight percentages) on the coating of each specimen, before their immersion into the SBF solution.	106
Table 15: Microhardness measurements.	114
Table 16: Porosity measurements on XPT-D-703 hydroxyapatite coating of sample No. 1.	117
Table 17: Porosity measurements on PYRO 4 hydroxyapatite coating of sample No. 2.	120
Table 18: Porosity measurements on XPT-D-703 hydroxyapatite coating of sample No. 3.	123
Table 19: Porosity measurements on PYRO 4 hydroxyapatite coating of sample No. 4.	126
Table 20: Porosity percentage and average pore diameter (in μm) of all four specimens, acquired by image analysis.	127
Table 21: Porosity percentage and average pore radius (in μm) of all four specimens, measured by mercury porosimetry.	132
Table 22: Adhesion strength test results (in MPa) of commercial and nanostructured hydroxyapatite.	133
Table 23: Comparative table of porosity and pore diameter values, between theoretical prerequisite values and those of the four specimens.	135

CHAPTER 1: INTRODUCTION

The objective of the specific master thesis is to investigate the structure and the properties of thermal spray coatings, using conventional and nanostructured hydroxyapatite powder. The plasma spray parameters have been opted carefully, for both the two types of powder, namely commercial XPT-D-703 and nanostructured PYRO 4 hydroxyapatite powder. Additionally, it is being further explored if the latter, PYRO 4, excels in any points of the commercial type of powder, considering their use in medical implants.

The course of this project consists of five chapters. The first chapter, serves as an introduction, in order to present the aim and elaborate on the structure of the thesis.

In the second chapter, distinction between the already existent biomaterials is made and particular interest is gathered to bioactive hydroxyapatite and its synthesis methods. In addition, the need for nanosized coatings is emphasized and the basic principles of thermal spraying technology are presented. Moreover, microstructural characteristics that are detected and are expected on thermal spray coatings, based on the literature are presented. Finally, possible difficulties arisen due to plasma spray process are mentioned.

In the third chapter, the employed starting materials and the utilized plasma spray parameters are introduced. In specific, powder characteristics, such as the respective synthesis method, microstructure and elemental composition are presented. The experimental apparatuses and the procedures used for the characterization of the coatings are described in detail, as well.

The fourth chapter consists of results obtained during the laboratory work. The information provided, address microstructural characteristics of the plasma spray coatings, mechanical properties and chemical properties (e.g. bioactivity), porosity content and morphology of the pores. Figures regarding the detected microstructure and also tabulated data acquired throughout the experimental process complete this section. Analysis of the results is an essential step in this chapter.

In the final chapter, the estimated porosity content and pore size for each of the examined specimens are presented in summary. Comparative conclusions regarding the samples are drawn and a more complete estimation about their structure and properties is offered.

Finally, the references cited throughout the body of the thesis are listed after chapter five, at the end of this work.

CHAPTER 2: THEORETICAL PART

2.1) BIOMATERIALS

2.1.1) What is a biomaterial?

Biomaterial is a natural or synthetic material that is suitable for introduction into a biological system, especially as part of a medical device. For this exact reason not only their biocompatibility, but also biomedical devices themselves and relative response of the biomaterial to such devices should be considered.

Biomaterials had not always the form they have today. About 4000 years ago, linen threads were used as sutures by ancient Egyptians, while Mayans used sea shells to create artificial teeth around 600 AD. In the orthopaedics sector, the first hip replacement was allegedly performed in 1891 by Theodore Gluck, though the procedure was not successful. Later, John Charnley (1911-1982) invented the first effective hip joint prosthesis, while between 1968 and 1972 successful surgical operations with total knee replacements were performed by surgeons Frank Gunston and John Insall, among others [1].

When trying to understand the evolution of biomaterials research and their clinical availability during the last 60 years, three different generations seem to be clearly marked [2]. The first generation biomaterials, which were invented around 1980, are comprised by bioinert materials, as they present minimum immune response and the foreign body reaction. Second generation biomaterials include bioactive and biodegradable materials and were developed between 1980 and 2000. Such biomaterials enhance biological response and tissue surface bonding and undergo progressive degradation with healing and regeneration of tissues. Finally, third generation biomaterials appeared in 2002 and are aimed to stimulate specific cellular responses at the molecular level and also, signal and stimulate specific cellular activity. One such example of third generation biomaterials is the design of third generation bioactive glasses and macroporous foams with the ability to activate genes that stimulate regeneration of living tissues, so as both tissue engineering and in situ tissue regeneration are feasible [3].

Biomaterials can be metals, ceramics, polymers and composite materials and have the form of molded or machined parts, coatings, fibers, films, foams and fabrics. Typical examples of contemporary medical devices comprised of biomaterials are hip, knee and finger joints, heart valves, artificial hearts, breast implants and intraocular lenses (IOL).

2.1.2) Types of biomaterials

2.1.2a) Metallic biomaterials

According to the literature [4], [5], metals such as titanium and its alloys (Fig. 1), stainless steels (such as 316L), tantalum, magnesium and its alloys, Nickel-Titanium alloy (Nitinol), and cobalt- chromium alloys, are biocompatible and also the ones mostly used in dental and orthopaedic applications. Metallic biomaterials originated from the metals listed above, are particularly preferred due to their excellent mechanical properties, namely high mechanical strength and resistance to fatigue degradation. In addition, those metals have shape memory, can be sterilized easily before use and are resistant to corrosion due to the presence of a passive oxide layer covering their surface.

However, this protective oxide layer is in continuous contact with corrosive physiological environments such as blood, synovial fluids, or saliva [6] and is therefore prone to dissolution. As a result, metal ions and/or particles are able to escape into the blood stream and cause an inflammatory or allergic reaction, accompanied by reduction in biocompatibility and also tissue loss. Another issue for metallic prosthesis is that their elevated elastic moduli, sometimes much greater than that of the bone, causes an uneven distribution of stress between the implant and the adjacent hard tissue. Thus, relative motion of the implant-tissue interface takes place, leading to stress shielding of the bone.

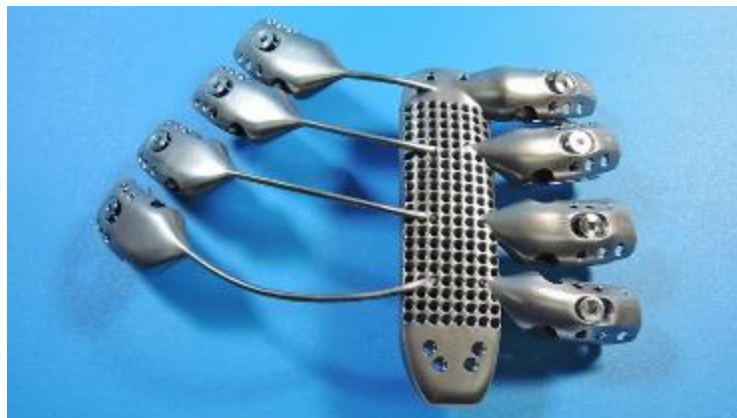


Figure 1: 3D printed custom-made prosthesis made of surgical grade titanium alloy [7].

2.1.2b) Ceramic biomaterials

Once again literature suggests that calcium phosphates (CaP), glasses and glass ceramics are the three material groups that constitute ceramic biomaterials. However, apart from division based on their type of ceramic, bioceramics can also be divided according to their degree of interaction with the surrounding host tissue or in other words their chemical reactivity. Consequently, three more categories of bioceramics arise [5], [6], [8], namely bioinert, bioactive and bioresorbable (elsewhere mentioned as biodegradable [9]).

Bioinert ceramics when inserted as implants into the body, they initiate a protective response that leads to encapsulation by a non-adherent fibrous coating about 1 μm thick. Over time this leads to complete isolation of the implant. Bioceramics that present the specific feature are alumina (Al_2O_3) and zirconia (ZrO_2). Although not ceramics, metallic and polymeric implants are also bioinert materials.

Bioactive ceramics induce a chemical reaction between the implant and the surrounding host tissue after implantation. In this way, a bond forms across the implant-tissue interface that imitates the body's natural repair process, thus bone tissue regeneration occurs. Such ceramics are bioactive glasses, bioactive glass-ceramics and hydroxyapatite ($\text{Ca}_{10}(\text{PO}_4)_6(\text{OH})_2$, also known as HAP).

Bioresorbable or else biodegradable ceramics are either resorbed or dissolved (by hydrolytic breakdown) with time and replaced by advancing host tissue. The chemical non-toxic by-products of the degrading materials are absorbed and released via metabolic processes of the body. A common example of bioresorbable ceramic is tricalcium phosphate ($\text{Ca}_3(\text{PO}_4)_2$, also referred as TCP).

Table 1: Ceramics used in biomedical applications [9].

Ceramic	Chemical Formula	Comment
Alumina Zirconia Pyrolytic carbon	Al_2O_3 ZrO_2	Bioinert
Bioglass Hydroxyapatite (sintered at high temperature)	$\text{Na}_2\text{OCaOP}_2\text{O}_3\text{-SiO}$ $\text{Ca}_{10}(\text{PO}_4)_6(\text{OH})_2$	Bioactive
Hydroxyapatite (sintered at low temperature) Tricalcium phosphate	$\text{Ca}_{10}(\text{PO}_4)_6(\text{OH})_2$ $\text{Ca}_3(\text{PO}_4)_2$	Biodegradable

Furthermore, bioceramic performance can be accessed by the utilization of osseointegration, osseointegration and osseointegration [10]. Osseointegration is the process by which osteogenesis is induced and suggests the recruitment of immature cells and their subsequent stimulation in order for them to develop into preosteoblasts. Therefore, osteoinductive bioceramics may induce bone formation, even when they are implanted in nonosseous tissue. Osseointegration is the capacity of bone growth onto a surface. Thus, osteoconductive bioceramics provoke hard tissue development in an osseous porous site. Finally, osseointegration is the fixation of an implant by the formation of surrounding bony

tissue without preceding growth of fibrous tissue at the bone-implant interface.

Apart from their biocompatibility, bioceramics have the potential to form a porous structure. Apparently, this capability is beneficial to bioceramic scaffolds, as highly interconnected porosity allows new tissue growth into and through the scaffold. In this way, osseointegration of the implant is enhanced [11].

On the other hand, ceramic biomaterials, although resistant to compressive stress, they respond extremely inefficiently in tension or bending, even at low stress. Such poor mechanical properties, along with brittleness of ceramics, make them unsuitable as load-bearing implants [9].



Figure 2: Knee replacement femoral component made of zirconia ceramics [12].

2.1.2c) Polymeric biomaterials

Compared to metals and ceramics, polymers are characterized by considerably lower strengths and moduli, but they can be plastically deformed to a greater extent before failure. As a result, polymers are generally not used in load-bearing biomedical applications [9], unless combined in order to form metal-ceramic-polymer hybrid materials [4].

However, ultra-high-molecular-weight polyethylene (UHMWPE) is an exception, as it constitutes a semi-crystalline polymer with superior strength, creep and wear resistance, that is used as a bearing surface in hip and knee replacements [9], [13]. Apart from UHMWPE, common polymeric biomaterials are synthetic polymers, such as polyesters and polyamides in synthetic suture materials or completely resorbable polymers in craniomaxillofacial, neurological, general surgical, and orthopedic procedures [13], [14] (Fig. 3). Other synthetic polymers are polypropylene (PP), ePTFE, PET/Dacron and nylon, which are used for ligament or tendon repair. Moreover, synthetic polymer of polymethyl methacrylate (PMMA) bone cement serves as an anchorage for artificial joint prosthesis to the bone and provides a homogeneous load transfer from the implant to the bone.

Nevertheless, two possible risks emerge from the use of polymeric biomaterials. Firstly, incomplete polymerization and/or onset of degradation process are often held responsible for leachable toxic rest-monomers inside the human body. Secondly, steam sterilization process is limited, due to low endurance and progressive degradation of polymers at high temperatures.



Figure 3: Bioabsorbable implants that have potential applications throughout the spine [14].

2.1.2d) Composite biomaterials

As it is denoted from all the above there is not any ideal biomaterial that acts as a panacea for construction of every implant meant to be used in orthopaedic or dental applications. However, combination of biomaterials might be the solution in this case (Fig. 4). More specifically, if ceramic coatings are applied onto metallic substrates, the resulting biomaterial is about to have improved surface biocompatibility and thus, better implant fixation. In addition, the underlying metal carries the load, whereas the surrounding bone strongly bonds to the ceramic coating and therefore, possibility of rupture of the implant is decreased. Moreover, the mismatch of the elastic moduli between the implant and the surrounding hard tissue is declined, as there is a smoother transition of values of Young's modulus from the higher ones respective to the metal substrate to the lower ones referred to the bone. Consequently, the possibility of stress shielding occurrence is also reduced.

Nevertheless, a hurdle arising from combination of biomaterials is the degree of their interconnectivity. Lack of adherence of the ceramic coating to the underlying metal substrate, can cause delamination of the coating and lead to implant failure.



Figure 4: Artificial hip joints made of a combination of materials [15].

2.2) HYDROXYAPATITE (HAP)

Composition of both bones and teeth is in essence consisted of the same two phases, one organic and one inorganic in different quantities and also, water (Fig. 5). For bones the organic phase, including water percentage, can reach up to 30 % by weight [4]. The organic phase is mostly Collagen type I, an insoluble fibrous protein that is one of the most abundant proteins in the body [16]. Collagen forms a matrix which serves as a template for calcium (Ca^{2+}) and phosphorous ions (PO_4^{3-}) that precipitate upon the matrix and form biological hydroxyapatite [17]. Additionally, the organic phase contains bone cells, namely osteoblasts, osteocytes and osteoclasts. Osteoblasts are the primary bone cells which stimulate bone formation by synthesis and secretion of the collagen matrix (bone-forming cells). Later, the same cells are trapped inside the matrix (inactive osteoblasts) and maintain bone formation activity. Therefore, they are evolved into osteocytes (bone-maintaining cells). Finally, osteoclasts hold responsibility for the destruction of bones (bone-destroying cells) and are necessary throughout bone growth during the development stages of the body [18].

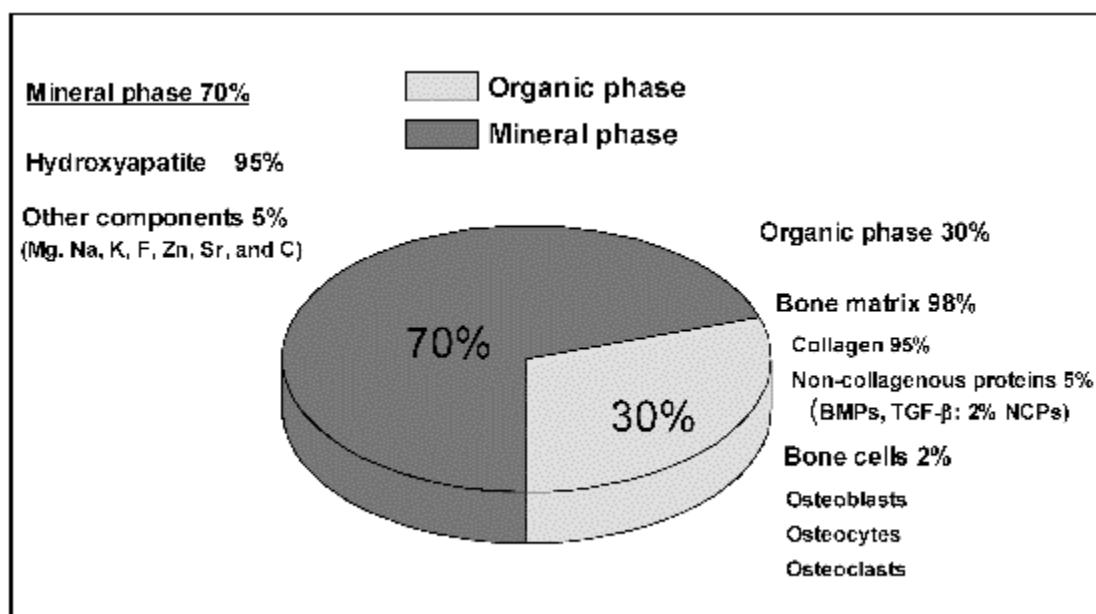


Figure 5: Chemical composition of bone tissue [4].

The rest of the bone tissue composition (about 70 %) is the mineral phase which is, as denoted above, biological hydroxyapatite. Biological hydroxyapatite, contains sodium, magnesium, fluorine and chlorine ions that substitute calcium and phosphorous ions in the crystal lattice. Moreover, biological HAP is always carbonate substituted (PO_4^{3-} is replaced by CO_3^{2-}), thus biological HAP might also be referred to as carbonate hydroxyapatite [8], [19]. This carbonate content is around 4 % and increases with age to approximately 8 %, while hydrogen phosphate ion decreases [18]. In addition, biological HAP is non-stoichiometric (the molar Ca/P ration is lower than 1,67) and less crystalline, compared to synthetic hydroxyapatite (see table 2).

Synthetic hydroxyapatite is one of the most used bioceramics in dental and orthopaedic implants, due to its similarity to the mineral component of bone. Synthetic HAP is stoichiometric, meaning the Ca/P ration is 1,67 and crystalline (see table 2). Ca/P ratio varies among the different calcium phosphates used as orthopaedic materials and is an indicator of grate significance as it can be correlated with acidity and solubility. More specifically, acidity and solubility of the mixture increase as the Ca/P ratio decreases, while both parameters decrease substantially for Ca/P ratios close to 1,67. Furthermore, solubility is also affected by pH values and is enhanced as pH is diminished.

Table 2: Comparative composition, crystallographic and mechanical properties of human enamel, bone and HAP [8].

	Enamel	Cortical bone	HA
Constituents (wt%)			
Calcium, Ca ²⁺	36.0	24.5	39.6
Phosphorus, P	17.7	11.5	18.5
(Ca/P) molar	1.62	1.65	1.67
Sodium, Na ⁺	0.5	0.7	Trace
Potassium, K ⁺	0.08	0.03	Trace
Magnesium, Mg ²⁺	0.44	0.55	Trace
Carbonate, CO ₃ ²⁻	3.2	5.8	—
Fluoride, F ⁻	0.01	0.02	—
Chloride, Cl ⁻	0.30	0.10	—
Total inorganic	97.0	65.0	100
Total organic	1.0	25.0	—
Absorbed H ₂ O	1.5	9.7	—
Crystallographic properties			
Lattice parameters (±0.03nm)			
<i>a</i>	0.9441	0.9419	0.9432
<i>c</i>	0.6882	0.6880	0.6880
Crystallinity index	70–75	33–37	100
Crystallite size, nm	130 × 30	25 × 2.5–5.0	
Products after sintering >800°C			
	HA + TCP	HA + CaO	HA
Mechanical properties			
<i>E</i> (GPa)	14	20	10
Tensile strength (MPa)	70	150	100

According to bibliography [20], the crystal system of hydroxyapatite (HAP) can be either monoclinic or hexagonal. Monoclinic crystal system of HAP presents pseudo-hexagonal symmetry, and therefore the crystal system of HAP is usually considered to be hexagonal. In addition, it has been reported that HAP undergoes reversible phase transition from monoclinic (low temperature phase) to hexagonal crystal system (high temperature phase) at approximately 480 K. Finally, it is indicated that the structure of HAP is sensitive to its chemical composition and preparation methods, as well.

While in hexagonal crystal system, HAP (Ca₁₀(PO₄)₆(OH)₂) is organized in small crystal plates of about 50 nm in length, around 25 nm wide and on average 3 nm thick [18], [21]. A single unit cell of HAP consists of 44 atoms, which include 10 calcium atoms (Ca), 6 (PO₄) tetrahedra, and 2 OH⁻ groups [21]. Elsewhere [22], it is suggested that the general formula of HAP is Ca₁₄Ca₂₆(PO₄)₆(OH)₂, where Ca₁ and Ca₂ are two different crystallographic positions for the 10 calcium atoms present in the unit cell. More specifically, four calcium atoms are

placed in the Ca_1 site, and they are surrounded by nine oxygen atoms, which are part of the PO_4 tetrahedra. The rest six calcium atoms are situated in the Ca_2 position and are surrounded by the six oxygen atoms of the PO_4 tetrahedra and by one of the hydroxyl ions.

Regarding arrangement of different atoms inside the unit cell of HAP, it has also been mentioned [23] that hydroxyl groups (OH^-) can also take different configurations. In other words, the hydroxyl group can deviate away from the symmetry position, thus obtaining four possible locations in the unit cell, on either side of two symmetry positions and consequently causing disorder of the oxygen and hydrogen ions. Nevertheless, among these possible locations of the hydroxyl group, there is a preferred arrangement (Fig. 6), in which all OH^- groups line up with oxygen and hydrogen ions alternate in a column parallel to the c-axis.

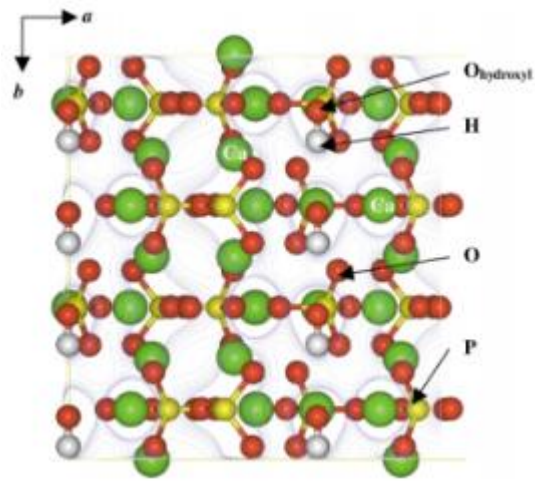


Figure 6: Preferred rearrangement of hydroxyl groups within the hydroxyapatite structure (O = red, Ca = green, P = yellow, H = white) [23].

Finally, biological and synthetic hydroxyapatite has a hexagonal crystal structure with corresponding crystal lattice parameters $a = b = 9.432$, $c = 6.881 \text{ \AA}$, $\alpha = \beta = 90^\circ$, $\gamma = 120^\circ$ [23], [24].

2.2.1) Chemical synthesis of hydroxyapatite

Several methods have been developed for the synthesis of HAP powders, a reasonable classification of which, according to M. Sadat-Shojai et al. [25], can be:

- Dry methods
 - Solid-state method
 - Mechanochemical method
- Wet methods
 - Chemical precipitation
 - Hydrolysis method
 - Sol-gel method
 - Hydrothermal method
 - Emulsion
 - Sonochemical method
- High temperature processes
 - Combustion method
 - Pyrolysis method
- Synthesis from biogenic resources
- Combination of procedures

Three methods, namely chemical precipitation, sol-gel synthesis and hydrothermal method that were mostly encountered through the literature review, for synthesis of HAP nanoparticles, are presented below.

2.2.1a) Conventional chemical precipitation method

In order for chemical precipitation to occur, typically two types of reagents are used. These reagents are aqueous solutions of Ca^{2+} and PO_4^{3-} ions, respectively, and are mixed under continuous stirring, while the Ca/P molar ratio is stoichiometrically maintained. It is noted [26] that, supersaturation is necessary for nucleation start and crystal growth. During precipitation of HAP nanoparticles pH value is kept above 7 and temperature values extend from room temperature to approximately boiling temperature of water [25], [27]. Subsequently, the precipitate solution undergoes aging under atmospheric pressure or it is alternatively subjected to filtering, washing with water and ethanol, drying at 40-50 °C and crushing to obtain powder form. Acquired powders may be typically calcined at 400-600 °C for refinement of the crystal structure.

Process parameters that are of great importance during chemical precipitation are pH and reaction temperature of the solution and seem to correlate in an inversely proportional way. It is for higher purity of the produced HAP powders, that pH and/or reaction temperature are kept relatively high throughout the process. However, when a specific morphology (e.g. crystallinity) of the powder is targeted then lower values for the abovementioned parameters are preferred [25]. It is specifically mentioned [28] that for synthesis of monocryalline HAP particles reaction temperature should be lower than 60 °C.

Main advantages of the chemical precipitation method are availability of starting materials, low operating cost and better control on morphology and mean size of the produced powders. On the contrary, maintenance of a stoichiometric Ca/P molar ratio, during synthesis process, is inhibited by process variables.

2.2.1b) Sol-gel synthesis method

Sol-gel synthesis method is a technique through which synthesis of nanoscaled ceramic powders is enabled. During sol-gel method the precursor materials, that are usually metal alkoxides (tetraethyl orthosilicate or TEOS ($\text{Si}(\text{OC}_2\text{H}_5)_4$) and tetramethyl orthosilicate or TMOS ($\text{Si}(\text{OCH}_3)_4$)) are in dispersion in a colloidal liquid, also known as “sol”. Through processes of hydrolysis, condensation and polymerization both viscosity and density of the “sol” is increased and therefore a “gel” is resulted (gelation process). This “gel” is in essence a biphasic mixture in which, the liquid phase is entrapped within the solid phase (inorganic network). Subsequently, “gel” undergoes aging as so long the liquid part is segregated from the solid part, while condensation is continued. Then follows drying, during which removal of the interstitial liquid phase is occurred, accompanied by shrinkage and densification of the solid phase. Finally thermal treatment (sintering) of the material is performed and thus, chemical stabilization is achieved. Further densification due to sintering is also present.

Sol-gel synthesis method is preferred among others, as it provides nanosized end products characterized by higher homogeneity and purity. Additionally, it constitutes an energy saving method, as low processing temperatures ($<400^\circ\text{C}$) [26] are acquired. In this way, degradation during sintering is avoided as well [25].

On the other hand, drawbacks of this method are the high cost of starting materials and higher processing times (e.g. aging). Furthermore, volatile substances may be present during process (e.g. solvents). Finally, shrinkage phenomena and also possible secondary phases present in the end products, are not desirable.

2.2.1c) Hydrothermal method

During hydrothermal method chemicals in an aqueous solution with precursor soluble ions, react under elevated temperature ($T > 25^\circ\text{C}$) and pressure ($P > 100\text{ kPa}$) [28], inside a pressure vessel, and thus, crystallized ceramic substances are produced.

Once again pH and reaction temperature are critical factors regarding determination of morphology and size of the synthesized HAP particles. Although it is mentioned [25] that hydrothermal method usually yields rod-like HAP particles (nanorods), different value combinations of pH and reaction temperature present particles with different morphological and structural characteristics.

Hydrothermal method is advantageous among other wet methods, like chemical precipitation and sol-gel synthesis, as no further thermal processing is required in order for crystalline HAP to be produced [26]. However, the already risen values of both temperature and pressure, achieved during hydrothermal method, set the necessity of costly equipment. Finally, the specific method lacks control over morphology and size distribution of the synthesized HAP powder particles [25].

Table 3: Comparison of the different methods for the preparation of HAP nanoparticles [25], [26].

Synthesis method	Duration (</> 24h)	T (°C)	Particle size (µm)	Cost	Reproducibility
solid-state	>	1050 - 1250	> 2,0	low	medium
chemical precipitation	>	RT* - 85	> 0,1	low	high
sol-gel	>	37 - 85	> 0,001	variable	low
hydrothermal	<	150 - 400	> 0,05	usually high	low
emulsion	>	RT* - 50	> 1,0	high	low - medium
combustion	<	170 - 500	> 0,45	usually low	low

*RT= Room Temperature

2.2.2) Why nanosized HAP?

It has been proposed [29], [30] that, the organic phase of the bone, namely, collagen fibers are compiled into parallel rows, thus forming a bundle of rows with successive fibers along each row. However, these fibers although parallel to each other are not arranged on the same point in the row, thus small gaps known as “hole zones” are formed. These gaps are about 40 nm in length and 5 nm in width and serve as mineralization spots for the inorganic phase of the bone (Fig. 7). As it has already been mentioned [18],[21], natural bone hydroxyapatite phase consists of non- stoichiometric carbonated apatite crystals, that are in the form of nanosized plates or needles with average dimensions of 45 nm length, 20 nm width and 3nm thickness. Therefore, production of nanostructured HAP powders and composites for construction of medical implants is a logical step for desirable development in the field of orthopaedics.

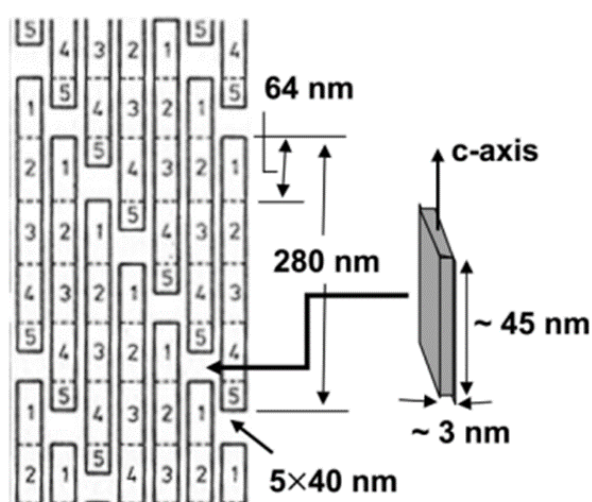


Figure 7: Depiction of the hole zones present throughout the collagen fiber bundle and the size and orientation of the carbonated hydroxyapatite crystals relative to the fibril direction [29].

The positive response and long-term functions of osteoblasts on nanoceramics with grain sizes less than 100 nm, have been confirmed by a novel (at the time) in vitro study [31], that has led researches [32], [33] to claim that nanostructured biomaterials promote osteoblast adhesion and proliferation, osseointegration, and the deposition of calcium containing minerals on the surface of these materials.

More specifically, nanosized HAP particles are characterized by greater specific surface area compared to that of larger sized particle counterparts. Greater surface area allows greater degree of interaction with the surrounding environment and taking into consideration that “the first and immediate biologic reaction to a foreign body is its coating with proteins” [34], the absorbed quantity amongst the available proteins of the surrounding physiological environment is increased [35], [36]. As a result, both cell adhesion and proliferation are enhanced.

Finally, it is mentioned that, higher specific surface area enables effective aggregation [36], as nanostructured ceramics can be sintered at a lower temperature. Subsequently, problems associated with high temperature sintering processes, such as degradation of mechanical properties, are diminished [32], [37].

2.2.3) In vitro bioactivity investigation

Upon the construction of a new type of biomaterial, check of its physiological reaction before its commercial release seems to be preliminary. Regarding hydroxyapatite coatings, bioactivity investigations are performed on samples that are candidate medical implants in orthopaedics, via utilization of a simulated body fluid (SBF).

More specifically, T. Kokubo and his colleagues developed, in 1990 [38], an acellular simulated body fluid that has inorganic ion concentrations similar to those of human extracellular fluid, in order to stimulate the formation of apatite on bioactive materials in vitro [39]. An alternative commercial simulated body fluid solution is known as the Hank's balanced salt solution (HBSS). The compositions of both the abovementioned solutions are presented in the following table (table 4), for preparation of 1 L of each solution accordingly.

Table 4: Compositions of Kokubo solution and Hank's balanced salt solution. The ingredients appear in chronological order of preparation [38].

Number	Kokubo solution (after Ohtsuki ^a), pH = 7.4		Hank's balanced salt solution, pH = 7.0	
	Reactant ^b	Quantity	Reactant ^b	Quantity
1	Ultra-pure water	0.75 l	Deionized water	1 l
2	NaCl	7.996 g	NaCl	8.0 g
3	NaHCO ₃	0.35 g	MgSO ₄	1.0 g
4	KCl	0.224 g	KCl	0.4 g
5	K ₂ HPO ₄ ·3H ₂ O	0.228 g	CaCl ₂	0.14 g
6	MgCl ₂ ·6H ₂ O	0.305 g	MgCl ₂	0.10 g
7	1 kmol/m ³ HCl	40 cm ³	Na ₂ HPO ₄	0.06 g
8	CaCl ₂	0.278 g	K ₂ HPO ₄	0.06 g
7	Na ₂ SO ₄	0.071 g	—	—
8	(CH ₂ OH) ₃ CNH ₂	6.057 g	—	—
9	1 kmol/m ³ HCl	To adjust to pH = 7.25 at T = 36.5°C	—	—

Up to date, corrections and suggestions for improvement of the Kokubo solution have been made [40], in relation to the ion concentrations of the SBF, some of which are shown in the following table (table 5).

Table 5: Ion concentration of SBFs and relative ion concentration of human blood plasma [40].

	Ion concentration (mm)							
	Na ⁺	K ⁺	Mg ²⁺	Ca ²⁺	Cl ⁻	HCO ₃ ⁻	HPO ₄ ²⁻	SO ₄ ²⁻
Human blood plasma	142.0	5.0	1.5	2.5	103.0	27.0	1.0	0.5
Original SBF	142.0	5.0	1.5	2.5	148.8	4.2	1.0	0
Corrected SBF (c-SBF)	142.0	5.0	1.5	2.5	147.8	4.2	1.0	0.5
Revised SBF (r-SBF)	142.0	5.0	1.5	2.5	103.0	27.0	1.0	0.5
Newly improved SBF (n-SBF)	142.0	5.0	1.5	2.5	103.0	4.2	1.0	0.5

Usually, time of about 28 days is prerequisite for the new apatite layer to cover the existing hydroxyapatite coating [41], although satisfying results within 14 days have been reported [42]. In addition, in order for the coating method to be made more cost-effective and also to accelerate apatite formation, SBF with higher ion concentrations, such as 1,5x, 2x, 2,5x, 5x and even 10x ion concentration of SBF, have been utilized.

2.3) THERMAL SPRAYING

2.3.1) Thermal spray techniques

Thermal spraying is a group of processes that make use of thermal and kinetic energy in order to melt the feedstock material and then propel it onto a prepared substrate material. In the beginning, the feedstock material can either be solid in the form of wire or powder, or in the molten state inside a crucible. The most common thermal spray techniques for hydroxyapatite application are atmospheric plasma spraying (also known as air plasma spraying or APS), vacuum plasma spraying (VPS, also known as low pressure plasma spraying- LPPS or controlled atmosphere plasma spray), high velocity oxygen fuel spraying (HVOF) and cold spraying (or cold gas spraying). The following figure presents a comparative diagram of the processing temperatures and material transport velocities for the various thermal spray processes (Fig. 8).

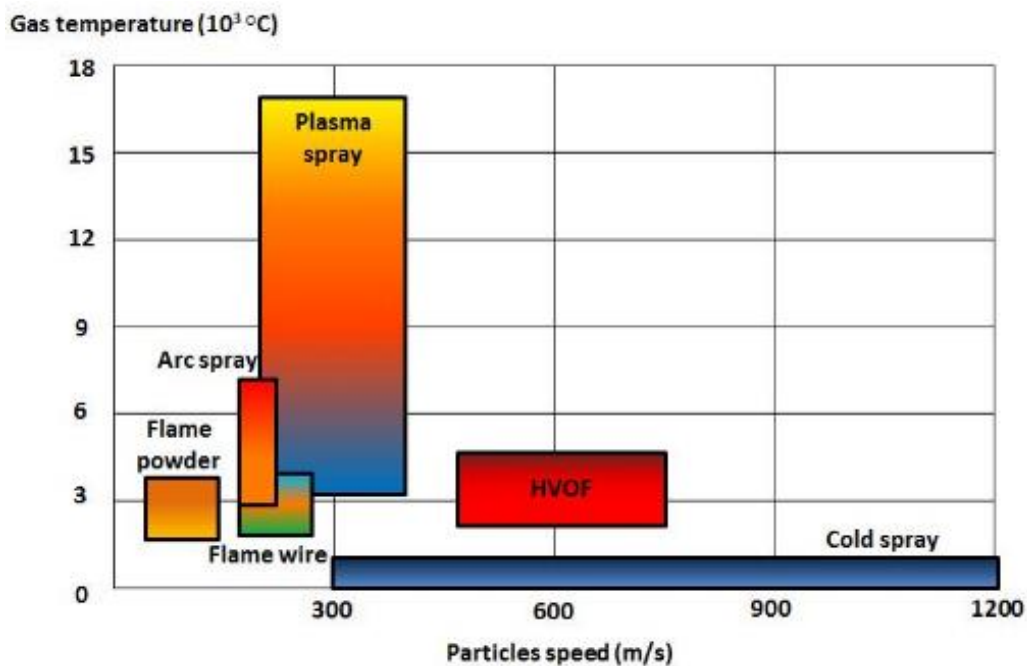


Figure 8: Comparison of the processing temperatures and material transport velocities for the various thermal spray processes [43].

2.3.1a) Atmospheric plasma spraying (APS)

In atmospheric plasma spraying a plasma gun/torch creates an electric arc current of high energy which is started by high frequency high voltage ignition between a cathode and an anode [44]. The plasma gun utilizes a chamber with one or more cathodes (electrodes) and an anode (nozzle) [45] (Fig. 9). An inert gas is directed through the space between the cathode and the anode, and subsequently the arc current ionizes the gas, and a plasma plume is formed. More specifically, monoatomic gases like argon or helium are partially ionized and molecular gases like hydrogen or nitrogen are dissociated prior to ionization [46]. The electrons and ions in this plasma plume are separated from each other and are accelerated toward the cathode and anode, respectively. These rapidly moving particles then collide with other atoms or molecules in the gas and recombine. As a result, energy is emitted and the temperature of the plasma jet rises up to 16000 °C in the core at the gun exit [47]. Thus, a plasma flame is formed that emerges from the gun toward the substrate at velocities approaching or exceeding the speed of sound (up to 450 m/s). The feedstock material is injected into the plasma flame, where it is melted and propelled towards the target substrate to form the coating.

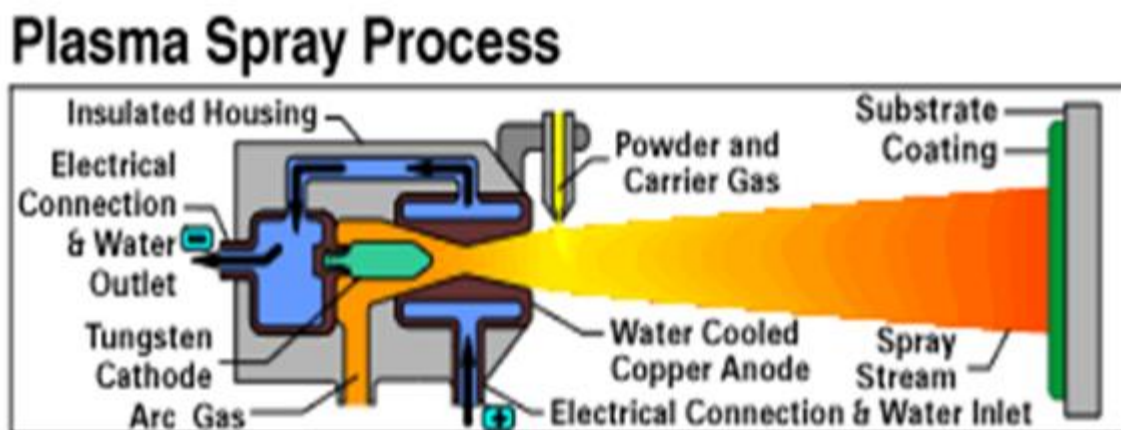


Figure 9: Principle of the atmospheric plasma spray process [48].

2.3.1b) Vacuum plasma spraying (VPS)

In vacuum plasma spraying the spraying environment, namely pressure, is controlled, so as the melted particles oxidize far less, thus resulting in coatings of considerably higher quality. The spray equipment consists of a conventional plasma spray gun (insulated to prevent low-pressure arc discharges) fitted with a nozzle modified for higher pressure expansion ratios. The plasma jet exhausts into a chamber (Fig. 10) at below atmosphere pressure, typically in the range of 30 to 300 torr (0.6 to 5.8 psia) [49], while other reports mention 2 kPa as a lower value of the chamber pressure during the coating operation [44]. Arc temperature reaches approximately 16000 °C and particle velocity ranges between 200 to 400 m/s [50].

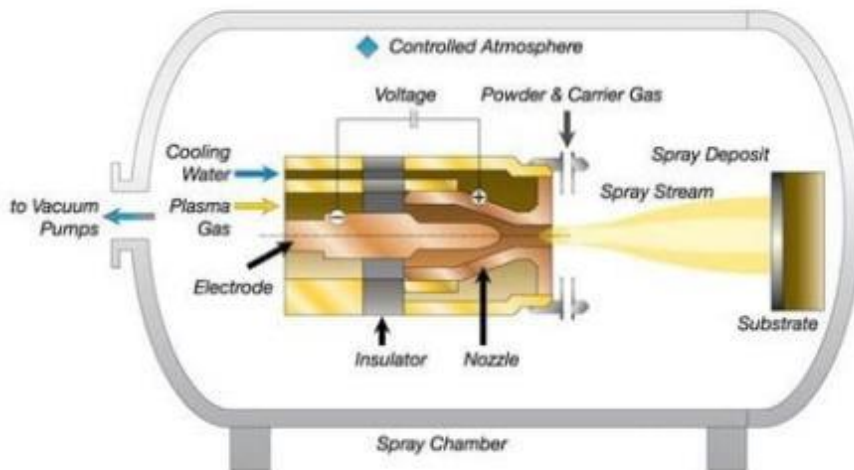


Figure 10: Schematic diagram of a controlled atmosphere plasma process [50].

2.3.1c) High velocity oxygen fuel (HVOF) spraying

In HVOF spraying, high-volume combustible gaseous fuels (e.g. hydrogen, methane, ethylene, acetylene, propylene, propane) or a liquid fuel such as kerosene, are fed into a combustion chamber, into an 8 to 30 cm (3 to 12 in.) long confining nozzle (barrel) (Figs. 11a and 11b). Fuel and oxygen are mixed and combusted under controlled pressure. Different combustibles and also fuel to oxygen flow rate ratios can determine the maximum achievable flame temperature. Subsequently, the coating powder, is introduced into the nozzle and is uniformly heated by the hot mixture gas stream to a molten or semi-molten condition. The flame and powder, assisted by the geometry of the nozzle (converging/diverging) and the risen combustion pressure are accelerated to near supersonic velocities (e.g. 400 to 800 m/s). Therefore, the powder particles are propelled toward the substrate by much higher velocities than plasma spray (by such high velocities) that, the resulted coating is characterized by increased density and adhesion and also low oxide content [51].

Lower average particle temperatures (around 3000 ° C), compared to plasma spray, reduce the degree of particle melting and oxidation. However, in spite of the decreased temperature values of the particles, high coating densities are still achieved through HVOF, due to the beforementioned high particle impact velocities. In this way, powder particles that may have not been melt are further heated on impact with the substrate, by the conversion of kinetic energy into thermal energy. Thus, the specific particles deform and contribute to the formation of a dense coating [49].

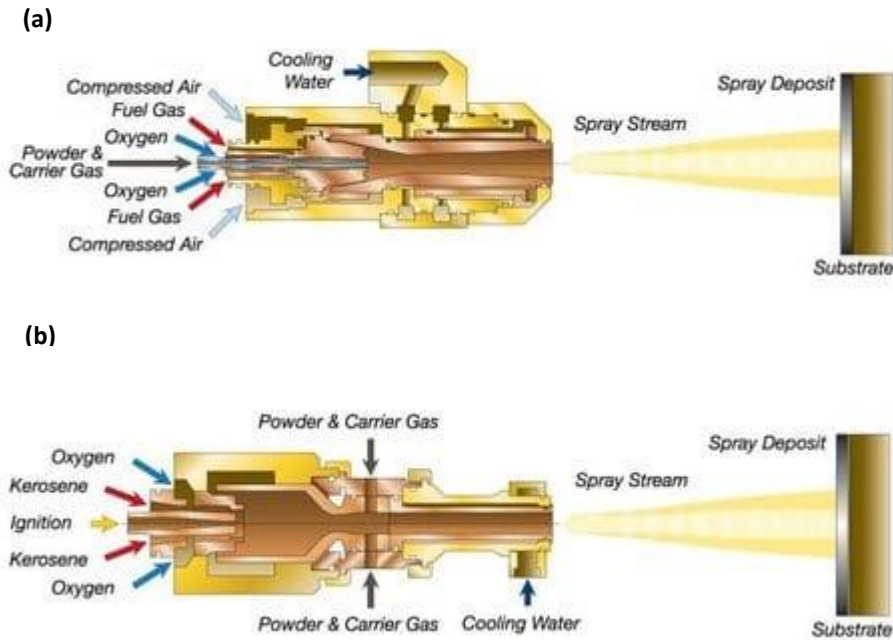


Figure 11: Schematic diagram of High Velocity Oxygen Fuel (HVOF) spray with (a) gas fuel [52] and (b) liquid fuel [53].

2.3.1d) Cold spraying

In cold spraying, also referred to as cold gas dynamic spraying, the powder feedstock is inserted in a solid state along with the carrier gas into a powder feeder and propelled to a converging/diverging type nozzle (Fig. 12). Cold spraying is a process based on conversion of thermal energy to kinetic energy and as such, both the powder feedstock and the carrier gas are being pressurized and heated, at typical inlet pressures up to 4 MPa [44] and relatively low temperatures, in the range from 0 to 800 °C [44], [49], although still below the melting point of the powder particles. The powder particles are therefore accelerated at supersonic speeds through the gas medium and while carrier gas expands at the end of the nozzle, the particles impact onto the substrate and undergo plastic deformation and also, consolidation. Typically acquired speeds of the process gas during cold spraying are 300 to 1200 m/s [49], [54], while the process gases mostly used are helium or nitrogen.

It should be noted that in order to achieve satisfying adhesion of the particles onto the substrate, they need to be accelerated, so as a critical value of velocity is reached. This critical value is material dependent and is high enough to induce sticking of the particles and avoidance of substrate corrosion, as well. Particle velocity can vary according to the chosen carrier gas. An additional important factor that affects the successful deposition of the particles is their deformability degree. Ceramics lack deformability and thus, higher velocities are required for ceramic coating deposition.

The main advantage of cold spraying is the use of elevated velocities instead of advanced heating and therefore, decreased tensile residual stresses, oxidation phenomena and phase transitions within the coating material. Moreover, nanostructured coatings are possibly favored due to additional refinement of the grain size of the sprayed particles. However, careful control of particle velocity is required, that presupposes adjustments in the

process gas, namely temperature, pressure and composition and also check of the size of the sprayed particles.

Finally, two variations of cold spray technique are high pressure cold spray (HPCS) in which particles are injected prior to the spray nozzle throat (inlet pressure up to 4 MPa and induced particle velocities up to 1200 m/s) and low pressure cold spray (LPCS) in which powders are injected in the diverging part of the spray nozzle (inlet pressure less than 1 MPa and particle velocities in the range of 300 to 600 m/s).

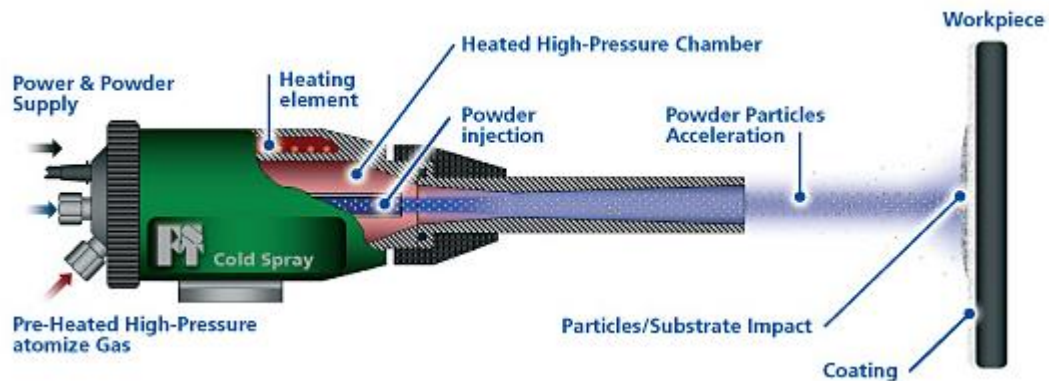


Figure 12: Principle of a cold gas spray process [55].

2.3.1e) Other coating techniques

In spite of thermal spraying techniques being extremely popular nowadays, for coating hydroxyapatite on substrate materials, a variety of other coating methods have been developed. Some of these techniques are magnetron sputtering, sol-gel processing, and biomimetic coating methods. Such techniques outweigh the rest in a sense that they enable coating of complex shapes, better control of the coating thickness, and utilization of lower coating production temperatures [56].

2.3.2) Microstructural characteristics after thermal spraying

2.3.2a) Splat formation

It is suggested that adhesion between a coating and the adjacent substrate is achieved through diffusion, chemical reaction (formation of a new adhesive chemical compound) and mechanical interlocking [57].

During thermal spraying, powder particles are accelerated and deposited in a molten or semi-molten state upon the prepared surface of the substrate and thus, mechanical interlocking occurs. Each one of these impacted particles is known as a splat and their collective microstructure defines the structure of the bulk coating [58].

Splats undergo deformation and rapid solidification (a few microseconds [59]) upon impact. Moreover, droplet liquid separation from the solid (substrate)/liquid (particle) interface is occurred. In further detail, the molten or semi-molten droplet is flattened while spreading on the substrate and part of its mass is fixed upon it, due to applied shear stress [60]. Their thermal energy is also decreased as the substrate is relatively larger and cooler than the impinging droplets. It is considered that solidification (also referred as freezing) of the splats is completed individually for each splat and therefore each one of them acts as a "hotter" substrate for the subsequent ones [61]. As a result, a bulk coating is formed that bears the characteristic lamellar structure present in thermal spray coatings.

Regarding good adherence of the coating onto the substrate, key factors such as acquired particle velocity and also temperature of both the substrate and the particle, prior to impact, are to be considered. When the particle velocity is increased, then the formed droplet has more time to adequately spread before its solidification takes place and thus, a disk-shape splat is formed (Fig. 13). On the contrary, when particle velocity is decreased, the droplet partially freezes before impact with the substrate and as a result, fragmented splats are formed that lack flattening extend and consequently adhesion to the substrate [60], [62]. In some cases [49], splats were even found to be completely disintegrated, when particle velocities exceed 400 m/s, during HVOF spraying [58].

In a similar way, when either the substrate temperature is risen (200-400 °C, [61]) or the sprayed particle is fully melted (meaning particle temperature is elevated) flattening of the droplet is enhanced, and satisfying adhesion is achieved. Alternatively, flattening is restricted and splat separation from the substrate is accelerated. In general, splat formation during thermal spray process can be a subject of study by itself, since the amount of thermal spray coating parameters that affect splat formation is numerous (Fig. 14).

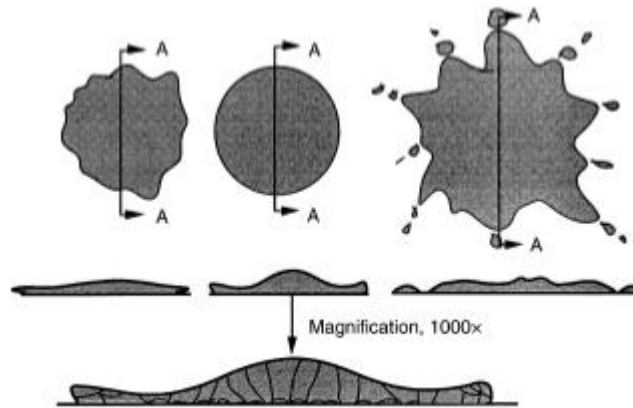


Figure 13: Typical thermal spray splat structures. Flattened splat with rounded edges (upper left corner), disk-shape splat (first row in the middle) and flattened splat with elongated fringes (upper right corner). Depiction of the relative splats above, as seen from the side (middle row). Magnification of the side of the centre splat (bottom row) [49].

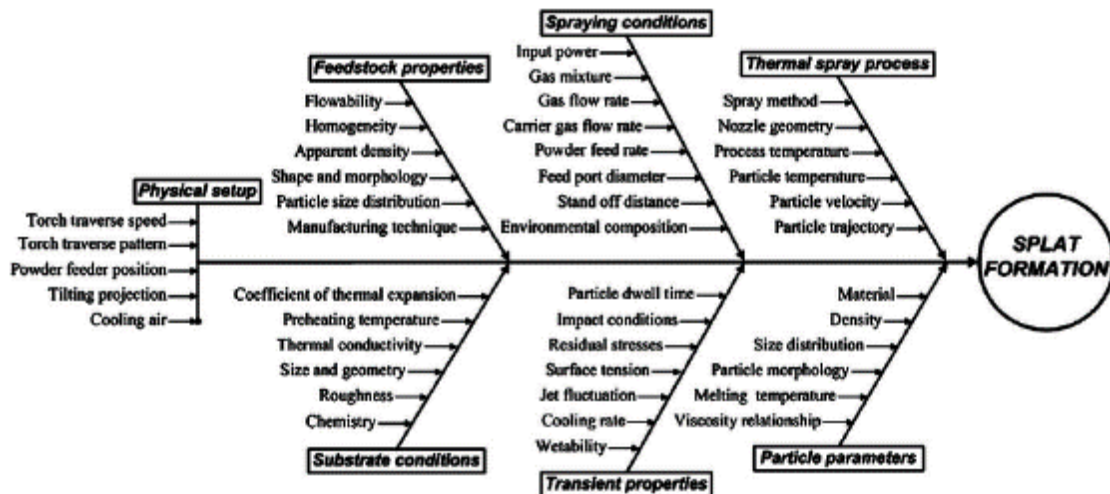


Figure 14: Thermal spray coating parameters involved in splat formation [63].

2.3.2b) Porosity

When impingement of splats occurs, four possible pore formations are utilized, namely, micropores, open pores, through-thickness pores and sealed pores (Fig. 15). Micropores have a size of about 1-2 μm and may already be present in the powder particles prior to thermal spraying. It is a usual course for such micropores to aggregate during deposition and evolve into larger pores of about 7 μm in size, inside the splat. Open pores as well as through-thickness pores are utilized due to release of gas entrapped within the liquid droplet, during thermal spraying. As for sealed pores (also known as closed pores), they constitute the unrealized pores, in which expansion of the entrapped gas was intercepted by rapid solidification rate.

It should also be noted that, during impingement open or through-thickness pores on already formed splats are often filled with liquid mater from the subsequent splats and therefore, healing effect is occurred. Furthermore, internal pressure from gas bubbles

entrapped in sealed pores can lead to numerous defects like microcracks, fragmentation and residual stresses. From the above, it is concluded that porosity of a bulk coating is determined as the total of the sealed pores and the unbonded areas among splats [58]. Finally, it is mentioned that according to ASM HandBook [49], as much as 40 % porosity is intentionally included in porous coatings constructed for medical implant prostheses, while other sources [8] state that 65 % of interconnected porosity is ideal for cortical bone regeneration.

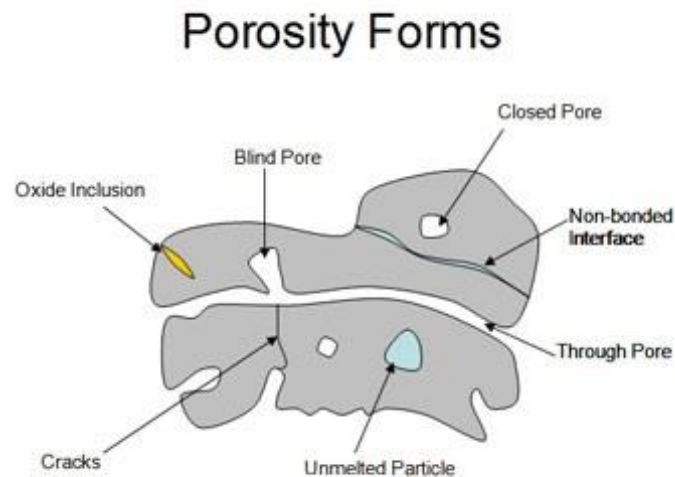


Figure 15: Thermal spray porosity forms [64].

2.3.2c) Surface roughness

After meticulous study of the literature, it is revealed that surface roughness of the coating bears great importance, regarding the suitability of an implant. More specifically, it is mentioned that surface roughness holds a key role concerning cellular response, by enhancing cell adhesion, proliferation and detachment strength. Amongst previous studies there were authors who even supported the idea that topology is the dominant factor governing bone apposition to hydroxyapatite-coated implants [65].

Composition and structure of the implant surface influence the kinetics of protein adsorption, the structure [66], nature and quantity of the adsorbed proteins [67]. After implantation, the surface of the material is adsorbed by proteins circulating in the biological fluids. These proteins serve as a substrate for cell surface receptors, for the cells to adhere at the surface of implant [67]. In other words, the type of the existing substrate determines which integrins and extracellular matrix proteins are expressed by osteoblasts and thereby, osteoblastic differentiation is achieved [68]. It is mentioned that, among all extracellular matrix proteins, nanostructured surfaces preferentially adsorb vitronectin (due to its relatively small, linear and non-complicated molecule), and this protein is preferentially recognized by osteoblasts over other cell types [69].

Moreover, surface roughness is responsible for enhancement of microscopic interlocking. According to S. Hansson and M. Norton [70] a rough surface can be regarded as a total of pits with varying sizes, shapes and densities. Hard tissue is expected to grow into these pits and therefore, stabilize the implant by interlocking.

In conclusion, cell adhesion, proliferation and detachment strength seem to be relational to surface roughness intensity and are increased as the roughness of HA increased [68]. According to the literature, plasma sprayed hydroxyapatite coatings generally possess a surface roughness of $R_a = 3$ to $8 \mu\text{m}$ [65]. However, there are commercial hip implants, such as “twinSys Uncemented” stem, that bear specification of surface roughness $R_a \approx 10 \mu\text{m}$ [71].

2.4) Plasma spray problems

Some of the main issues that arise during plasma spraying of hydroxyapatite powders are the biocompatibility and integrity of the resulted coating. To begin with, it has been stated that [72], [73], [74], if sufficient bonding between the coating material and the hard bone tissue is wished to achieve, adequate crystallinity and simultaneous low dissolution rates of the coating are required. This is justified, as bone-derived HAP is crystalline and therefore, a phase mismatch of the coating/bone interface could impair consistency of the system. Moreover, partial dissolution of the HAP coating is essential to trigger bone growth. Bone self-destruction is a naturally occurring mechanism, in order for growth of self-generating hard tissue to take place. However, vast dissolution rates can cause insufficient bonding and coating disintegration.

During elevated temperatures of plasma spraying, new phases are generated from the HAP phase, such as amorphous calcium phosphate (ACP), tetracalcium phosphate (TTCP), tricalcium phosphate transitional phases (α -TCP and β -TCP), metastable crystalline products such as oxy-hydroxyapatite or oxy-apatite (OHA) and calcium oxide (CaO), that present greater dissolution than crystalline HA. The amorphous hydroxyapatite phase is connected to dextroxylation of HAP, according to the reaction: $\text{Ca}_{10}(\text{PO}_4)_6(\text{OH})_2 \leftrightarrow \text{Ca}_{10}(\text{PO}_4)_6(\text{OH})_{2-2x}\text{Ox}[\]_x + x\text{H}_2\text{O}$, where [] is a vacancy. Finally, while at temperatures above $1050 \text{ }^\circ\text{C}$ there exists equilibrium for HAP with TCP and TTCP ($\text{Ca}_{10}(\text{PO}_4)_6(\text{OH})_2 \leftrightarrow 2\text{Ca}_3(\text{PO}_4)_2 + \text{Ca}_4\text{P}_2\text{O}_9 + \text{H}_2\text{O}$), phase transitions still occur. More specifically, β -TCP phase is stable for temperatures up to $1120 \text{ }^\circ\text{C}$, while for temperatures between 1120 and $1470 \text{ }^\circ\text{C}$, α -TCP prevails [75].

Furthermore, although porosity is a desirable characteristic of the coating, in a sense that it provides pathways for the flow of body fluids and enhances bone fixation upon the implant, large pores and cavities lead to decreased coating integrity and consequently, mechanical weakening of the implant. Pores that normally promote bone ingrowth are generally in the 200 - $400 \mu\text{m}$ range [72], [76]. However, 70% [72] of the overall porosity is consisted of fine pores that have a diameter of less than $1 \mu\text{m}$ and are formed between successive lamellae of the coating. As it is implied if the as sprayed powder particles that are not adequately melted, tend to form non-flattened splats (Fig. 16), while the unmelted particles have scarce interparticle cohesion. Thus, large interlamellar pores and cavities (also known as voids) are formed.

Both the above repercussions can be somewhat controlled with better sizing of the sprayed powder particles [72]. Finer starting powder particles may provide a well melted coating characterized by coherence, although the formed amorphous and transitional

phases are bioresorbable and thus the coating lacks biocompatibility. On the contrary, relatively larger particles help the crystalline HAP phase to be preserved and consequently provide optimum attachment of the implant to the bone, although unmelted crystalline phases suggest the existence of a porous microstructure. As a conclusion, biocompatibility and coating integrity are two contradictory components, achievement of which is not always possible to be equally fulfilled.

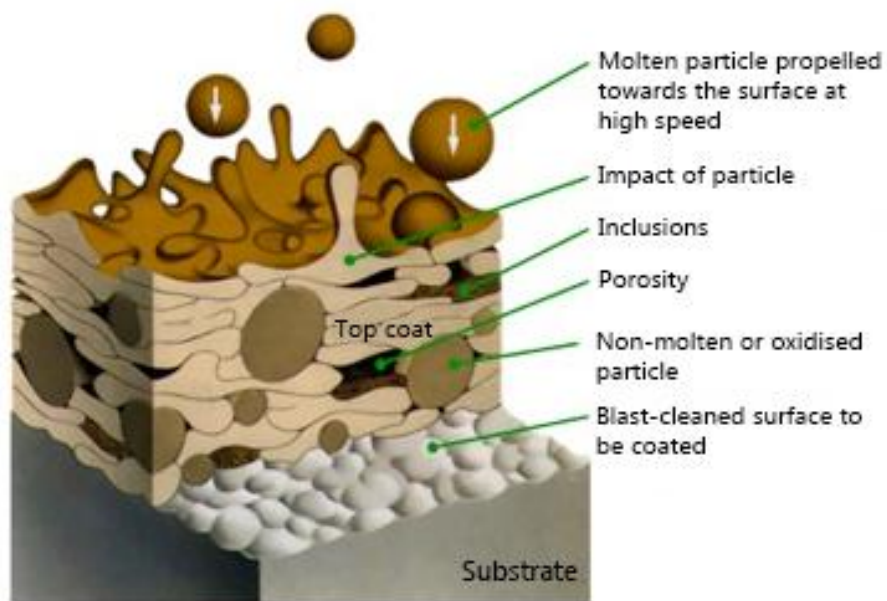


Figure 16: Cross-section of thermally sprayed layer [77].

CHAPTER 3: EXPERIMENTAL PROCEDURES AND METHODOLOGY

After exposition of the literature in Chapter 2, the methodology and also experimental procedures that were employed for completion of this thesis are presented in this chapter. More specifically, the acquired equipment and analyzing techniques, along with their purpose of use are displayed. Four specimens were prepared via atmospheric plasma spray process (APS) at PYROGENESIS SA and delivered to the Shipbuilding Technology Laboratory, School of Naval Architecture and Marine Engineering, NTUA. Two kinds of feedstock material were employed for the spray process, namely, commercial XPT-D-703 hydroxyapatite powder for half the samples and nanostructured PYRO 4 hydroxyapatite powder, which was mechanically treated in PYROGENESIS SA, for the remaining samples. The substrate of all the samples is stainless steel 304. The plasma spray parameters were altered for two out of the four specimens, each with a coating made of a different type of powder, in order for a greater amount of porosity to be achieved.

Microstructural examination of both the powders and the coated specimens was conducted, via optical microscopy and scanning electron microscopy at the Shipbuilding Technology Laboratory, School of Naval Architecture and Marine Engineering, NTUA and X-ray diffraction at the Department of Chemical Sciences, School of Chemical Engineering, NTUA, with the aid of Mrs. A. Karamperi. Regarding the coated specimens procedures precedent to microstructural observation, such as cutting, boxing, grinding and polishing were utilized. Additionally, assessment of thickness, roughness and microhardness was conducted. Moreover, Hg porosimetry was performed at the Department of Materials Science and Engineering, School of Chemical Engineering, NTUA, by Mr. A. Karagiannis-Mpakolas and also, bioactivity check of the specimens, at the Laboratory of Physical Metallurgy, School of Mining and Metallurgical Engineering, NTUA, with the assistance of Mrs. M. Panou, in order to further characterize the coatings. Finally, adhesion strength tests were carried out on the premises of PYROGENESIS SA, conducive to determination of the best adhesion performance of the coatings, between the ones prepared with XPT-D-703 or PYRO 4 powder.

In the next chapter (chapter 4) all the obtained data from the abovementioned examination are presented and discussed in further detail, according to the literature. Relative tables with acquired measurements and also figures are available.

In the final chapter (chapter 5) the main conclusions of this study have properly been extracted and summarized.

Finally, the references mentioned throughout the text are displayed in the order of appearance, after chapter 5.

3.1) Materials

3.1.1) Powders

Overall, four specimens were examined. The hydroxyapatite powder on specimen No. 1 and specimen No. 3, was commercial hydroxyapatite powder XPT-D-703 (Figs. 19a to 19h) with particle size of around 38,31 μm . XPT-D-703 HAP powder has a cost of around 500 €/kg and was bought from Sulzer Metco Company by PYROGENESIS SA.

Specimens No. 2 and No. 4 were prepared with pharmaceutical hydroxyapatite powder, which is produced via classic chemical synthesis that yields very fine particle sizes of below 5 μm . The specific hydroxyapatite powder has a much lower cost that ranges from 10 to 20 €/kg and although much cheaper than XPT-D-703 HAP powder, it has the same performance with that of conventional hydroxyapatite powder. Pharmaceutical hydroxyapatite powder was bought from Sigma-Aldrich Company by PYROGENESIS SA and subsequently, undergone high energy ball milling, on the premises of PYROGENESIS SA, so as its grain size would be decreased to the nanoscale size, due to continuous generation of disturbances/defects at the grain boundaries and also fracture of the grains during the milling process. In the same time the powder nanoparticles were agglomerated into larger particles, due to sintering of the grains during high energy ball milling. The final agglomerated powder particles (PYRO 4) (Figs. 20a to 20h) are characterized by a more elongated rhomboid or tear-like shaped morphology with magnitude of the order of 57,08 μm .

3.1.1a) Optical microscope

Small quantities of each powder were used and observed through the optical microscope (Leica DMILM). Thus, assessment of the particle average diameter was performed with optical microscope software (LAS image analysis) on images acquired with x100 magnification (Figs. 19 and 20). The mean values of twenty measurements of the particle diameter for each type of powder are presented in the following table (table 6).

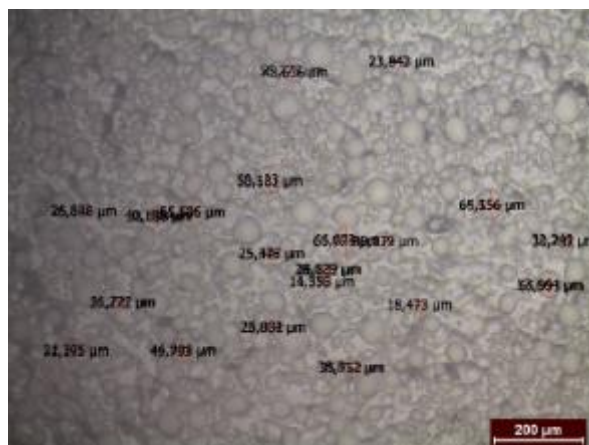


Figure 17: Twenty diameter measurements of the XPT-D-703 powder particles, via optical microscope.

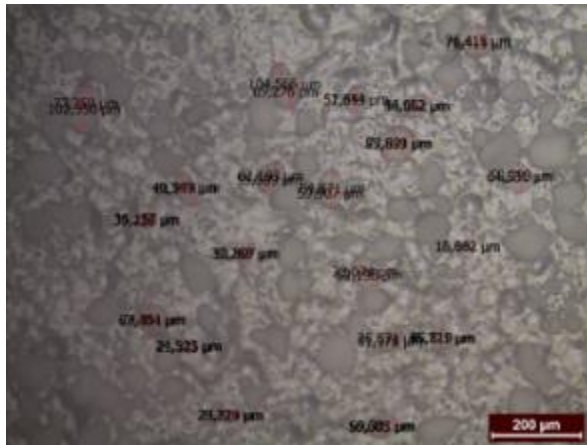


Figure 18: Twenty diameter measurements of the PYRO 4 powder particles, via optical microscope.

Table 6: Average diameter of powder particles (in µm).

Type of Powder	Mean diameter of powder particles (µm)
XPT-D-703	38,31 ± 16,99
PYRO 4	57,08 ± 22,63

3.1.1b) Scanning Electron Microscopy (SEM)

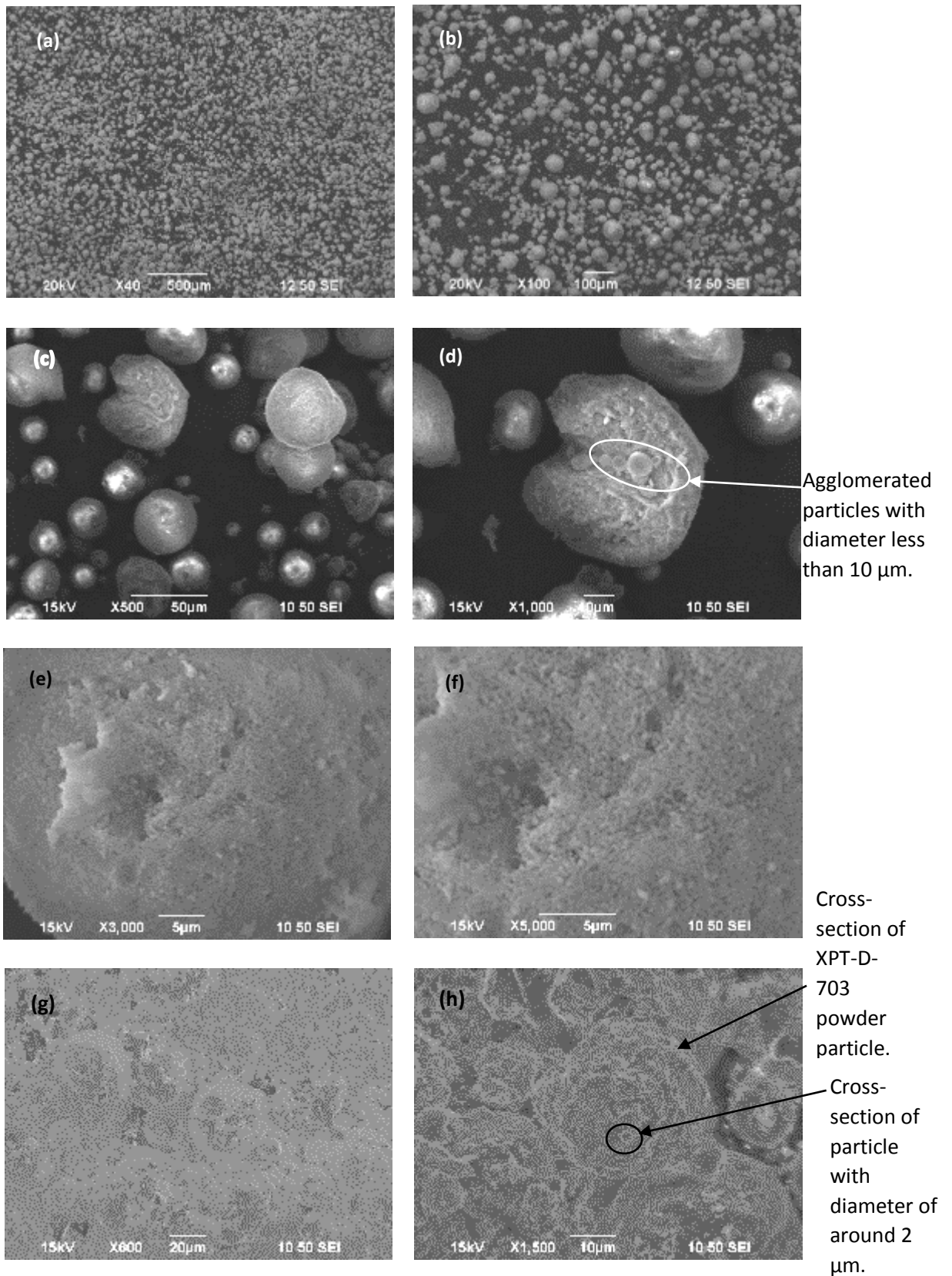


Figure 19: (a), (b), (c) SEM images of commercial XPT-D-703 hydroxyapatite powder at different magnification, (d) agglomerated particles with diameter less than 10 µm, (e), (f) powder particle in different magnification, (g) cross-section of XPT-D-703 powder particles, (h) cross-section of particle with diameter of around 2 µm.

As it is observed in figures 19a to 19d, XPT-D-703 hydroxyapatite powder is characterized by particles of mostly spherical morphology [78]. Each particle is agglomerated by many smaller spherical particles with diameter of around 10 μm or less (such microparticles are distinctive in Fig. 19d). In figures 19e and 19f, a powder particle in large magnification is observed, the surface of which seems to be comprised by an undefined cluster of nanoparticles (formations with size of less than 0,5 μm).

Finally, two samples were prepared with XPT-D-703 and PYRO 4 hydroxyapatite powder, respectively. Each type of powder was embedded in epoxy resin, following the process described in detail below (see paragraph 3.2.2), for boxing of the specimens. After the two powder specimens were detached from their molds, they were grinded at Struers LaboForce-1 and LaboPol-5 semiautomated grinding machine (Fig. 30) with fixed holders, with the use of gradually finer silicon carbide grinding papers of 1000, 1200, 2000 and 4000 grit. Each grinding paper was changed after one minute of grinding. No polishing was performed afterwards. As a result, observation of the cross-section of the powder particles was possible. In figures 19g and 19h, the cross-section of the particles of the commercial hydroxyapatite powder is presented. Cross-section of particle with diameter of around 2 μm is noticed inside a larger agglomerated particle.

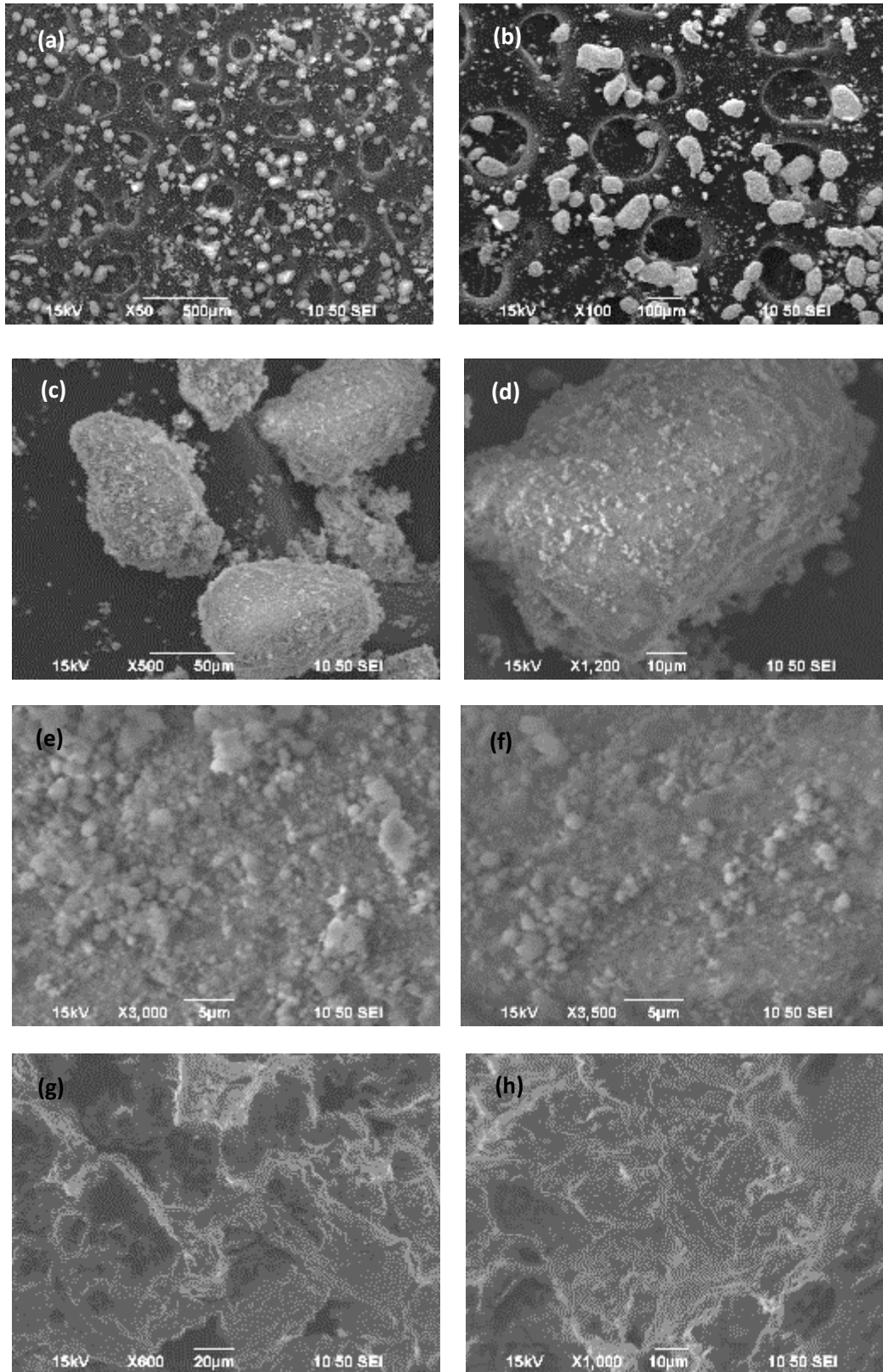


Figure 20: (a), (b), (c) SEM images of nanostructured hydroxyapatite powder at different magnification, (d) powder particle at larger magnification, (e), (f) surface of powder particle, (g), (h) cross-section of powder particles at different magnification.

Close examination of the PYRO 4 hydroxyapatite powder showed smaller particles of undefined shape agglomerated into final large particles [79] with more elongated rhomboid or tear-like shaped morphology (Figs. 20a to 20d). The surface of a powder particle in larger magnification is presented in Figs. 20e and 20f, upon which particles with sizes from 5 μm to less than 0,5 μm are dispersed. Finally, nanostructured morphology can be observed on the cross-section of the particles of the relative sample prepared with epoxy resin (Figs. 20g and 20h), as described above, though the main body of the particle is not distinct.

3.1.1c) Energy Dispersive Spectroscopy (EDS)

Moreover, Energy Dispersive Spectroscopy (EDS analysis) was performed on both types of hydroxyapatite powder, using SEM JEOL JSM-6390, in order to identify the elements present in the powders and their relative proportions. Ca, P and O elements were expected to be detected, as hydroxyapatite ($\text{Ca}_{10}(\text{PO}_4)_6(\text{OH})_2$) is the observed powder. EDS spectra and elemental tables acquired by spot analysis, are presented below, two for each powder (Figs. 21-24). It is noted that hydrogen is not presented in the following tables, as it is a light element and can not be detected.

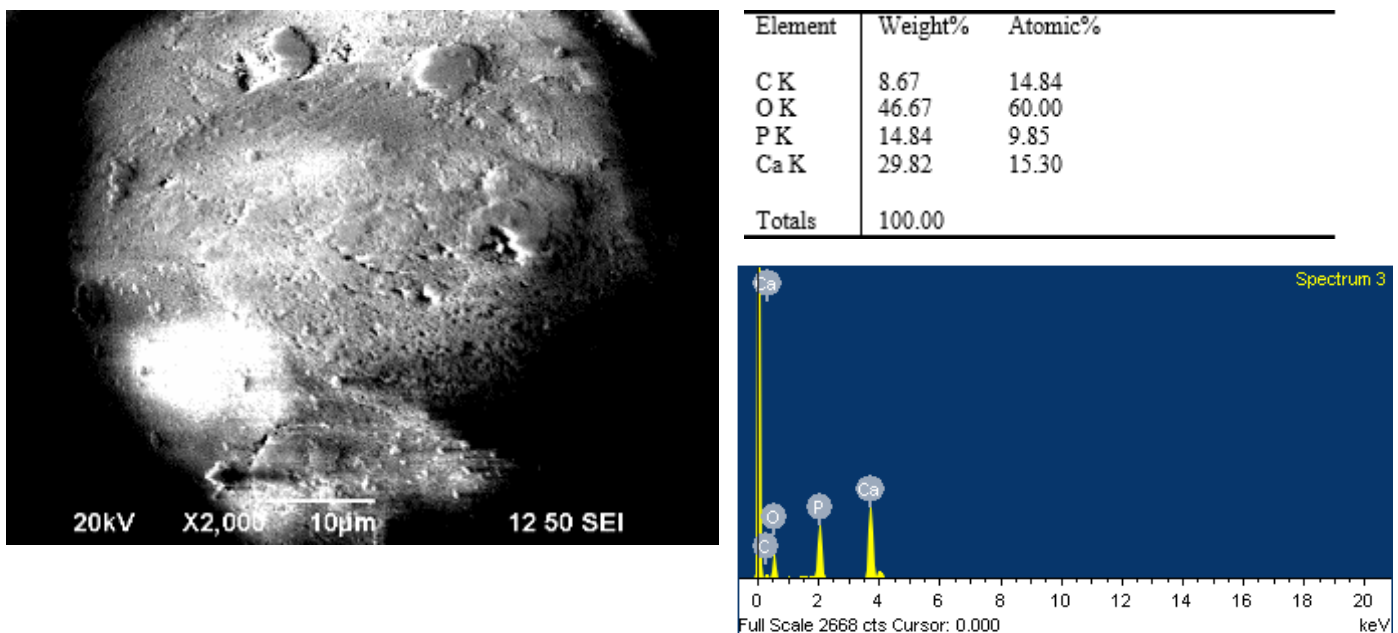
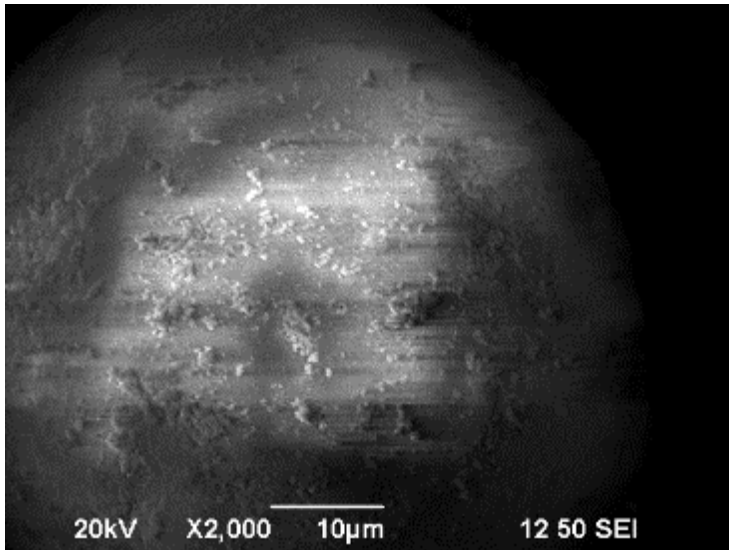


Figure 21: EDS spot analysis on particle of commercial XPT-D-703 hydroxyapatite powder.



Element	Weight%	Atomic%
C K	5.76	9.97
O K	49.63	64.42
P K	16.40	11.00
Ca K	28.21	14.61
Totals	100.00	

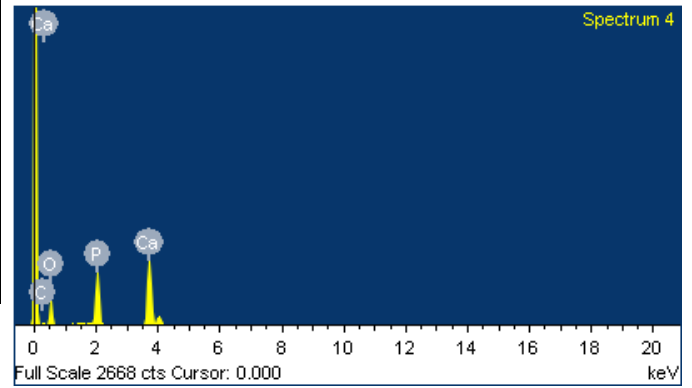
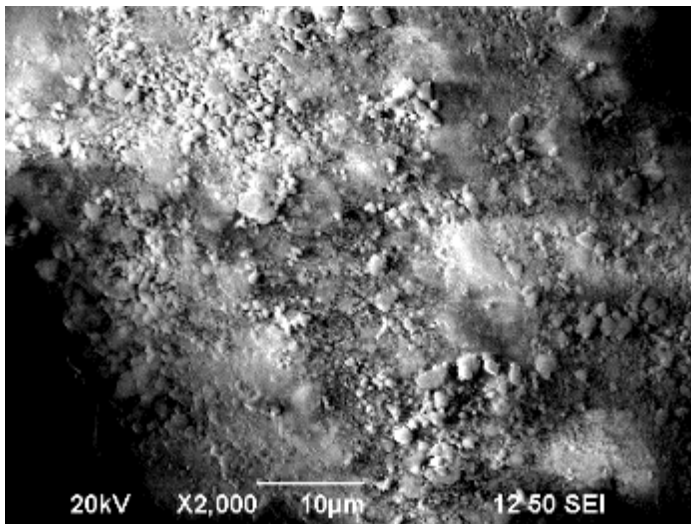


Figure 23: EDS spot analysis on particle of commercial XPT-D-703 hydroxyapatite powder.



Element	Weight%	Atomic%
C K	5.47	9.49
O K	49.98	65.08
P K	14.90	10.02
Ca K	29.65	15.41
Totals	100.00	

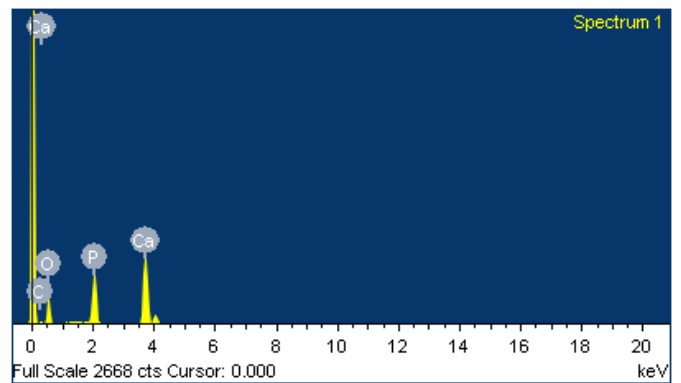


Figure 22: EDS spot analysis on particle of nanostructured PYRO 4 hydroxyapatite powder.

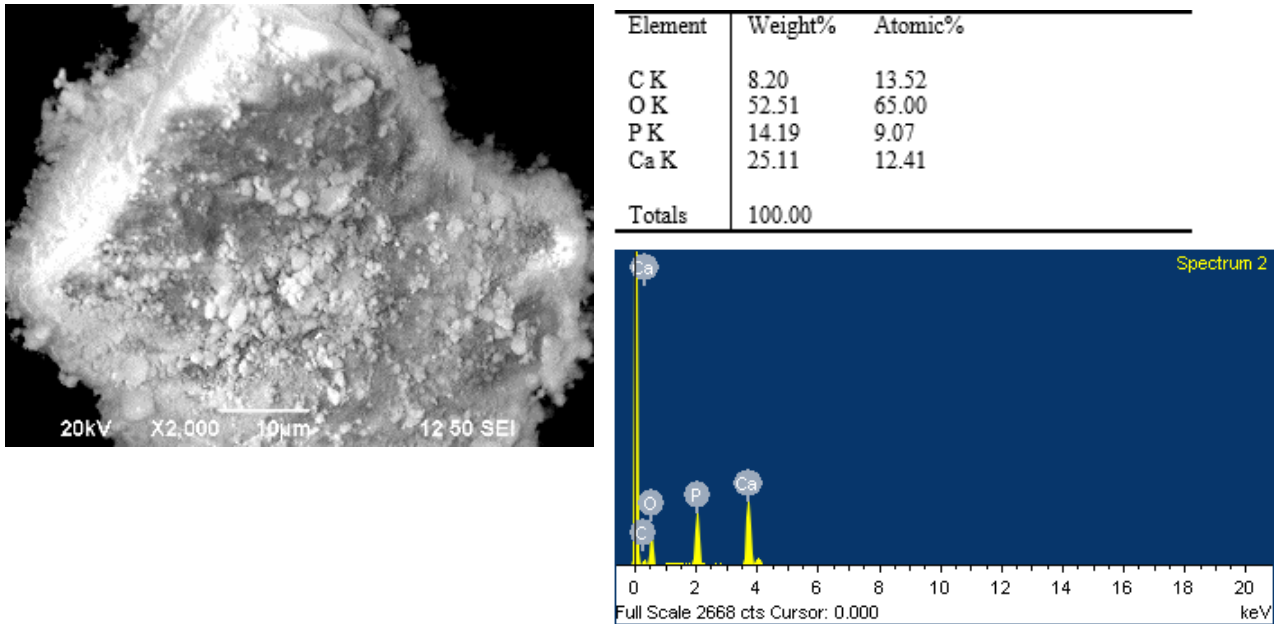


Figure 24: EDS spot analysis on particle of nanostructured PYRO 4 hydroxyapatite powder.

The detected elements in all spot analyses are Ca, P and O, as expected and also C which is appeared in very small weight percentages (5,47 % minimum and 8,67 % maximum percentage). The presence of C is justified, as a carbon tape is used in order for the powder to be fixed upon the sample bearer that is inserted into the SEM chamber. Generally, the measured values of weight percentage of each element present in the analyses are close for both types of powder. The dominant element for both hydroxyapatite powders is O, with average weight percentages 48,15 % and 51,25 % for the commercial and nanostructured hydroxyapatite powder, respectively. Next follows Ca with mean weight percentages 29,02 % and 27,38 % and finally, P with average weight percentages 15,62 % and 14,55 %.

3.1.2) Coatings and plasma spray parameters

Using the powders studies above, four specimens were prepared. The substrate of all four samples was stainless steel 304 and had been sandblasted before they were coated with hydroxyapatite powder via atmospheric plasma spray process (Fig. 25). What changed between the coatings prepared with the same type of hydroxyapatite powder, were the spraying parameters. More specifically, the plasma energy fluctuated between 30 to 50 kW and the stand-off distance (SOD) of the plasma gun, also known as spraying distance, varied from 7 to 9 cm. The powder used and also the proclivity of reduction or increase in the values of the spraying parameters is shown in the table below (table 7).



Figure 25: Principle of the plasma spray process (photograph acquired at PYROGENESIS SA).

Table 7: Type of powder and divergence of the plasma spray parameters for each sample.

No. of Sample	Type of Powder	Plasma Energy	Stand-off Distance
1	XPT-D-703	↑	↓
2	PYRO 4	↑	↓
3	XPT-D-703	↓	↑
4	PYRO 4	↓	↑

3.2) Characterization of the coatings

3.2.1) Coating roughness

Roughness measurements were taken on the surface of the coated specimens, before cut. The equipment used were surface roughness testers TR-100 and TR-200, both of which are manufactured and developed by Time Group Inc. (Fig. 26).

The examined parameters were Ra (arithmetical mean deviation of profile), Rz (ten point height of irregularities) and Rmax, namely Rt (total peak-to-valley height). Twelve roughness measurements for each roughness parameter were taken, for each specimen accordingly. The arithmetic mean value of all three roughness parameters was calculated based on the obtained measurements.



Figure 26: Surface roughness testers TR-100 (left) and TR-200 (right).

3.2.2) Preparation of the samples

The original samples needed to be reduced in size, in order for the microstructural characterization of the interface to be completed. The specimens which were cut with Struers Discotom-50 (Fig. 27) at approximately 2200 rpm (rotational speed of the disk) and propulsion speed 0,5 mm/s, are presented below (Figs. 28 and 29). Their dimensions, before and after cut, are also shown in table 8.



Figure 27: Struers Discotom-50.

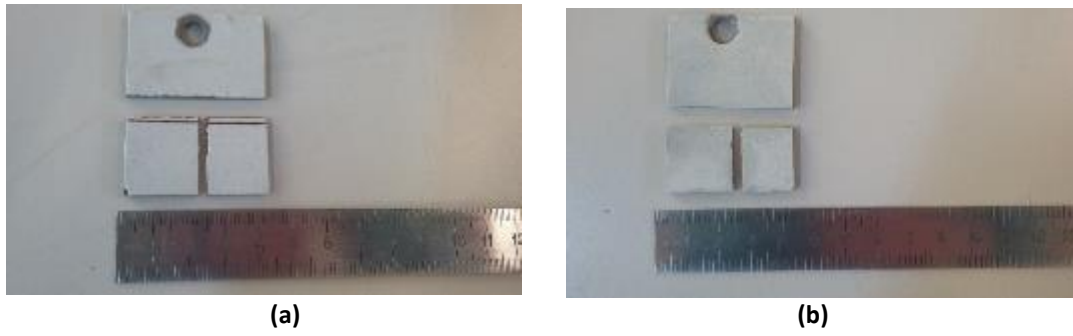


Figure 28: (a) Sample No. 1 with XPT-D-703 and hydroxyapatite powder and (b) sample No. 2 with PYRO 4 hydroxyapatite powder, both before and after cut.

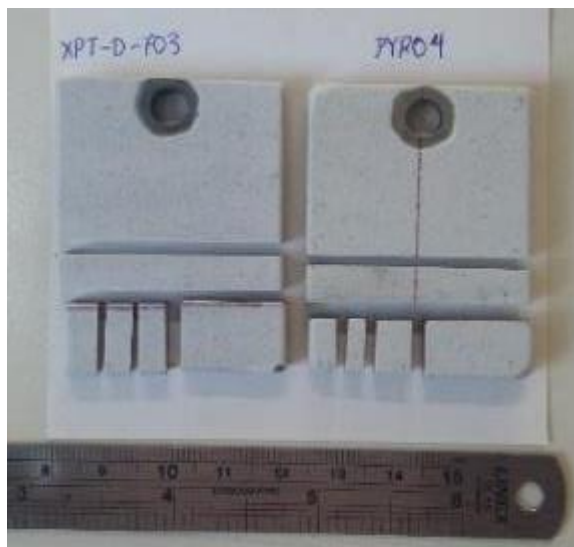


Figure 29: Sample No. 3 with XPT-D-703 hydroxyapatite powder (left) and sample No. 2 with PYRO 4 hydroxyapatite powder (right), both before and after cut.

Table 8: Dimensions of the samples before and after cut.

No. of Sample	Type of Powder	Before cut (mm)	After cut* (mm)
1	XPT-D-703	50 x 41 x 3	22,5 x 21 x 3
2	PYRO 4	50 x 38 x 3	20 x 20 x 3
3	XPT-D-703	50 x 40 x 5	20 x 12 x 5
4	PYRO 4	50 x 39 x 5	20 x 9 x 5

* After cut dimensions refer to the dimensions of the samples that were boxed in epoxy resin for further microstructural examination.

Subsequently, each sample is placed inside a cylindrical mold, which has been previously been covered with a layer of silicon for easier removal of the sample. The side of

the sample that is desired to be observed faces the bottom of the mold, while the sample is held at the correct position with the use of a multclip, if needed. Then, the samples are embedded in a mixture of epoxy resin and hardener. More specifically, the composition of the mixture for each sample has a volume ratio of fifteen parts Epofix resin to two parts Epofix hardener, according to Struers manufacturers. The mixture is stirred for two minutes and is then left to rest for the next two minutes. Then, the mixture is poured over the sample that is placed inside the mold. The mold is placed inside a chamber where vacuum is created through a pump, in order to avoid the formation of air bubbles on the surface of the sample. The specimen is left inside the chamber for one day, so as for the resin to solidify into a cylindrical shape.

After the whole specimen is detached from its mold, its surface is grinded and polished. Grinding is performed at Struers LaboForce-1 and LaboPol-5 semiautomated grinding machine (Fig. 30), with fixed holders and with the use of gradually finer silicon carbide grinding papers of 120, 180, 220, 320, 500, 800, 1000, 1200, 2000 and 4000 grit. Each grinding paper is changed after three to five minutes of grinding. Polishing is performed at the same device with a velvet disc instead of grinding papers. Two different pastes of Aluminum Oxide (Al_2O_3) are used, namely AP-A Suspension Alumina of 1 μm and subsequently 0,3 μm , each for eight to ten minutes of polishing. Finally, the specimens are rinsed with water and ethanol under pressure. The laboratory equipment used in each step of the process is cleaned carefully for future use.



Figure 30: Struers LaboForce-1 and LaboPol-5 semiautomated grinding machine with fixed holders.

3.2.3) Stereoscope

The specimens were observed via stereoscope Leica Mz6 (Fig. 31) and stereoscopic images of x20 and x40 magnification were acquired via Leica DFC290 Digital Camera. The mean value of thickness of all the coatings was also estimated, based on five measurements for per sample, acquired by image analysis of the built-in stereoscope software (LAS image analysis).

3.2.4) Optical microscope

The microstructure of the specimens was examined with the use of the optical microscope Leica DMILM (Fig. 31), through snapshots that were taken at x100 and x200 magnification via Leica DFC290 Digital Camera.



Figure 31: Leica DMILM optical microscope (left) and Leica Mz6 stereoscope (right).

3.2.5) Scanning Electron microscopy (SEM)

All of the samples were non-conductive, due to the existence of the as-sprayed ceramic coating of hydroxyapatite. Therefore, the specimens were primarily coated with gold via Agar Auto Sputter Coater (Fig. 32), in order for standard SEM imaging to be achieved. Gold sputtering was performed inside the sputtering chamber under pressure of around 0,05 mbar and current of 40 mA, for one minute.



Figure 32: Agar Auto Sputter Coater.

Subsequently, the specimens were additionally examined regarding to their morphological cross-section and surface characteristics, as well. In total, twelve specimens were examined, namely the embedded cross-sections and coating surfaces of samples No. 1 to No. 4 before their immersion into the SBF (see paragraph 3.2.9) and the coating surfaces

from these samples after their immersion into the SBF. Observation was possible via Scanning Electron Microscopy (SEM), using SEM JEOL JSM-6390, at different magnifications for each sample and elemental composition was achieved via Energy Dispersive Spectroscopy (EDS), using EDS Oxford Instruments INCAx-sight elemental detector (Fig. 33).



Figure 33: SEM JEOL JSM-6390 and EDS Oxford Instruments INCAx-sight elemental detector.

3.2.6) X-ray Diffraction (XRD)

X-ray analysis was performed on six samples namely, the two types of hydroxyapatite powder and their respective coatings on the stainless steel 304 substrate. For the diffraction analysis a Bruker D8 Advance diffractometer (Fig. 34) was used, while the resulting data were acquired and processed by built-in software DIFFRACplus EVA.

Regarding to the experimental conditions under which the analysis was executed, it is noted that they were kept the same for all measurements for reasons of comparison. In further detail, monochromatic radiation $\text{CuK}\alpha$ ($\lambda = 1,5406 \text{ \AA}$) was used, at 40 kV and 40 mA. The range of scanning was $10\text{-}80^\circ 2\theta$ with a scan speed of $0,05^\circ$ per second (3° per minute), conditions close to the ones chosen in references [21], [80], [81]. The peaks obtained were compared with the standard references for hydroxyapatite (00-009432), calcium phosphate- α (00-009-348), calcium phosphate- β (00-009-169), tetracalcium phosphate (00-025-1137) and calcium oxide (00-037-1497) [81].



Figure 34: Bruker D8 Advance diffractometer.

3.2.7) Microhardness

The coatings on each one of the four different specimens, were mechanically tested via Vickers method. The mean value of microhardness was calculated, based on 10 measurements that were made along the coating, in the transverse direction of the interface between the coating and the substrate, on each sample. The equipment that was utilized was Wolpert and Wilson Vickers tester (Fig. 35) and the imposed load was 300gf.



Figure 35: Wolpert and Wilson Vickers tester.

3.2.8) Porosimetry

In order to evaluate the percentage of porosity, two different techniques were employed, namely image analysis and mercury porosimetry.

3.2.8a) Image Analysis

Regarding image analysis, MIPAR image analysis program was acquired and image analysis was performed on cropped images of x100 magnification obtained through the optical microscope. The results presented by this program rely on a black and white area estimation. Therefore, after the necessary adjustments made on the original images the black areas presented the pore surface and the white areas presented the solid compact surface of the coating, respectively. The results were in the form of percentages and did not actually provide any information on whether the internal porosity was characterized by interconnected or closed pores. Instead, the obtained data were used to access if internal porosity had in fact been achieved.

Further information on the type of the internal porosity that was present in the coatings were acquired via mercury porosimetry.

3.2.8b) Mercury (Hg) Porosimetry

Mercury (Hg) porosimetry or else Mercury Intrusion Porosimetry (MIP) is a method used to measure porosity and average pore size. More specifically, it provides a diagram of the pore size distribution in relation to the pore volume and also information regarding the total specific surface area, the bulk and apparent density of a sample. For materials containing larger pores, mercury porosimetry is the preferred experimental technique and the penetrometer detects pores within a pore range from $\sim 200 \mu\text{m}$ to $\sim 35 \text{ \AA}$ [82]. Subsequently, the experimental data are analyzed on the basis of the Washburn equation:

$$P=2\sigma \cos\theta/r,$$

where P is the pressure applied on the mercury, σ is the surface tension of mercury, θ is the contact angle between the solid (meaning pore walls) and the mercury [76] and r is the corresponding pore size.

Mercury porosimetry presents specific drawbacks. One of them is the fact that it measures the largest entrance towards a pore, but not the actual inner size of a pore [83] (Fig. 36). More specifically, Hg porosimetry data analysis assumes rod-shaped voids connected to the surface by voids of the same or greater diameter. Voids connected to the surface via smaller-diameter voids (e.g. bottle-neck pores) are assigned the volume of a void with the diameter of these necks and therefore, determinations of void sizes are typically shifted to smaller diameters [84]. In addition, the specific method can not be used to analyze closed pores, since the mercury has no way of entering that pore and thus, provides information on the open porosity.

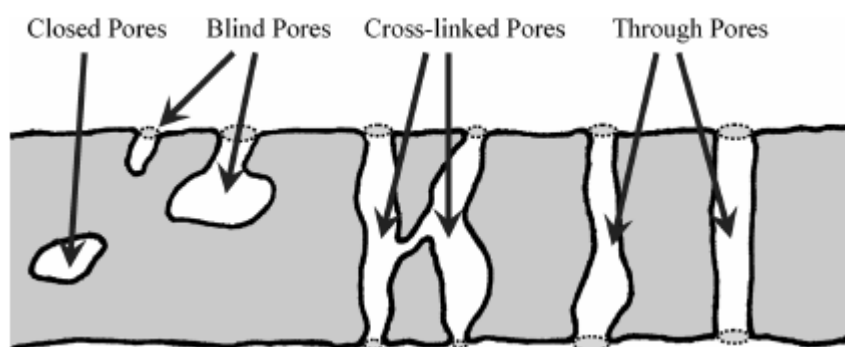


Figure 36: Schematic representation of pores [83].

Although, for practical reasons most instruments for mercury porosimetry use several transducers, mercury porosimetry apparatus in general, basically involves a Filling and Low Pressure System and a High Pressure System.

Initially the sample is evacuated to remove air and residual moisture or other liquids from the pore net. The sample cell is then filled with mercury as the entire system is still under reduced pressure. Subsequently, the overall pressure is slowly increased and allows mercury to penetrate the largest pores present in the sample or any void spaces between sample pieces. The first data point is usually taken at a pressure of 3000 to 4000 Pa or higher. Thereafter, the pressure is increased up to several atmospheres, which allows for a reasonable cross-over between the low and the high pressure part of the analysis. The

weight of the penetrometer, filled with mercury and the sample, is determined, which enables the user to calculate the bulk density of the sample. The volume of intruded mercury is also measured, continuously, through changes in the capacitance between the column of mercury in the dilatometer stem and a coaxial metal sheet surrounding the stem. Once transferred to the high pressure system, the sample cell is surrounded by hydraulic fluid and pressures of up to 414 MPa, are applied in an isostatic way.

The equipment used for this project, was a ThermoFinnigan Pascal 440 porosimeter (Fig. 37), with pore detection range from $\sim 100 \mu\text{m}$ to $\sim 37,5 \text{ \AA}$. The specimens were inserted in the sample cell after having been heated in the furnace at $60 \text{ }^\circ\text{C}$ for 24 hours and freeze dried for another 24 hours, in order to remove excess moisture from the cutting process.



Figure 37: ThermoFinnigan Pascal 440 porosimeter.

3.2.9) Bioactivity check

3.2.9a) Preparation of SBF

The SBF solution was prepared by chemical dissolution of NaCl, NaHCO₃, KCl, Na₂HPO₄, MgCl₂ · 6H₂O, HCl (1M), CaCl₂ · 2H₂O and Na₂SO₄ reagents in distilled water and buffer, while the pH values were recorded throughout the reaction. The SBF solution was buffered at pH 7,4, at 40 °C and its ionic concentrations were nearly identical to those of human blood plasma (Na⁺: 142,0, K⁺: 5,0, Mg²⁺: 1,5, Ca²⁺: 2,5, Cl⁻: 147,8, HCO₃⁻: 4,2, HPO₄²⁻: 1,0 and SO₄²⁻: 0,5 mM) [40]. More specifically, the pH was adjusted by addition of Tris-hydroxymethyl aminomethane ((CH₂OH)₃CNH₂), which induced an increase in pH value at around 8,79 and subsequently with 1,0 M hydrochloric acid (HCl), which reintegrated the pH to the desired value of 7,4. The quantities of the reactants required for preparation of the SBF solution are presented in the following table (table 9), according to their order of introduction into the solution.

Table 9: Quantities of the reactants required for preparation of the SBF solution.

Number	Reactant	Quantity
1	NaCl	9,8184 g
2	NaHCO ₃	3,4023 g
3	KCl	0,5591 g
4	Na ₂ HPO ₄	0,2129 g
5	MgCl ₂ · 6H ₂ O	0,4574 g
6	HCl (1M)	15 ml
7	CaCl ₂ · 2H ₂ O	0,5531 g
8	Na ₂ SO ₄	0,1065 g
9	Tris	9,0855 g
10	HCl (1M)	50 ml

3.2.9b) In vitro test

After synthesis of the SBF solution, each one the specimens were immersed into the SBF solution, inside fire resistant glass beaker of 100 ml capacity. The quantity of SBF poured in each beaker was 60 ml. The solution was kept at a stable temperature of 40°C, inside a furnace. The specimens were retrieved, after a period of 1, 3 and 7 days, in order to develop the desired hydroxyapatite layer on their surface. Every 48 hours, the SBF solution was replenished or renewed due to evaporation or absorption by the specimen, in order to keep its properties unchanged. Upon completion of the expected time in the SBF solution, the specimens were removed from their relative beaker and were placed inside the furnace at the same temperature (40 °C), for time period of 10 days, so as for the excess moisture to be removed. Subsequently, the samples that had been extracted from the SBF solution at the seventh day of their immersion were observed via SEM apparatus (see paragraphs 3.2.5 and 4.4.4).

3.2.10) Adhesion strength test

The adhesion strength test was carried out in accordance with the international standard ASTM 4541, “Standard Test Method for Pull-Off Strength of Coatings Using Portable Adhesion Testers” (Fig. 38), by Pyrogenesis SA. The test method covers a procedure for evaluating the pull-off strength of a coating system from a metal substrate. Pull-off strength is commonly referred to as adhesion or tensile strength. The test method determines force perpendicular to the coating surface before a pull-stub breaks [85].

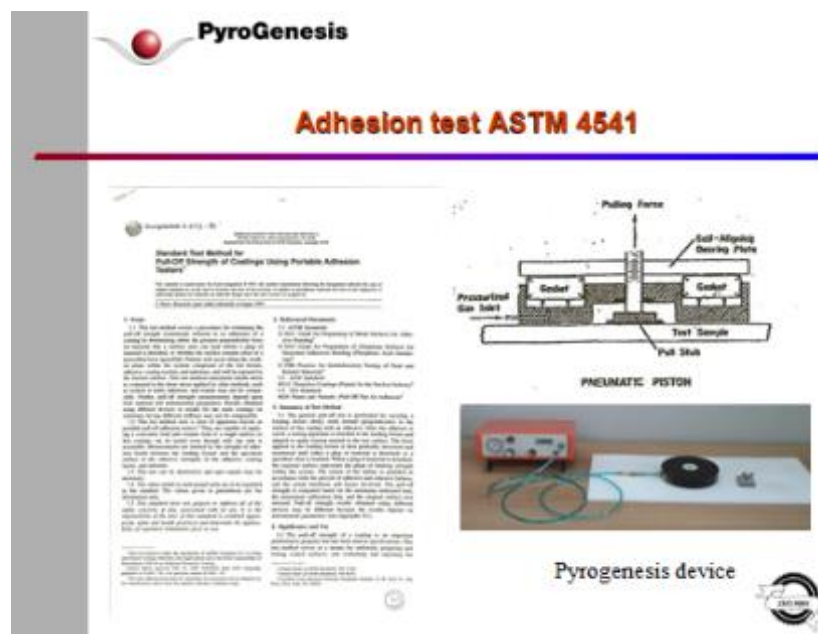


Figure 38: Adhesion test according to ASTM 4541.

Prior to beginning the test, the pull-stub must be properly cleaned to reduce any adhesive failure concerns. Regular equipment calibration also reduces error concerns. A light abrasion of the coating is permitted, followed by a solvent cleaning to promote adhesion of the adhesive material. If the coating is on a thin substrate, the back of each substrate test panel is coated with an adhesive and pressed down onto a four inch square ceramic tile to avoid distortion of the substrate. After the adhesive cures, the sample is subjected to an increasing stress until the weakest material in the coating system fails. These failures can be adhesive (between material), cohesive (within the same material), or any combination of the failure modes. The specimens were properly prepared, as shown in the following figures (Figs. 39 and 40), both before and after the adhesion test. In total, five measurements were taken (in MPa) for each type of hydroxyapatite coating.



Figure 39: Preparation of the specimens before the adhesion test.

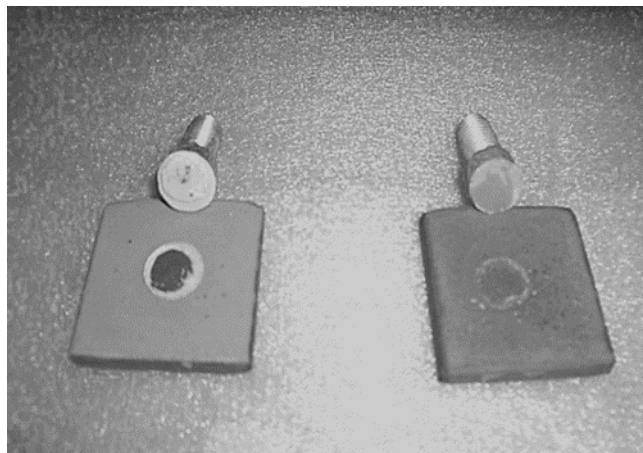


Figure 40: Adhesion test specimens after the adhesion test.

CHAPTER 4: RESULTS AND DISCUSSION

4.1) Coating roughness

Table 10: Roughness parameters Ra, Rz and Rmax.

No. of Sample	Type of Powder	TR-100		TR-200		
		Ra (μm)	Rz (μm)	Ra (μm)	Rz (μm)	Rt (μm)
1	XPT-D-703	$8,47 \pm 0,87$	$56,51 \pm 6,08$	$9,72 \pm 0,79$	$56,10 \pm 3,55$	$69,41 \pm 5,30$
2	PYRO 4	$7,30 \pm 0,62$	$49,76 \pm 5,73$	$8,67 \pm 0,83$	$52,38 \pm 4,34$	$66,53 \pm 8,13$
3	XPT-D-703	$5,90 \pm 0,65$	$39,01 \pm 7,36$	$8,73 \pm 0,90$	$48,81 \pm 4,86$	$64,54 \pm 9,65$
4	PYRO 4	$10,26 \pm 0,94$	$63,18 \pm 5,48$	$13,80 \pm 1,25$	$78,46 \pm 7,81$	$96,86 \pm 8,39$

From the acquired measurements shown above (table 10), it is concluded that all four specimens lie within the limits of the expected range of roughness values. Slightly exceeding roughness parameter values are presented, when measurements are obtained via TR-200 roughness tester. However, it is obvious that the specific piece of equipment provides somewhat higher data measurements in general and therefore, no profound deviation from the data obtained with TR-100, makes the data acceptable.

As it is derived from the acquired data, all of the roughness parameters examined change in the same direction. In further detail, roughness values decreased for the sample with XPT-D-703 hydroxyapatite powder, after alterations in the spraying parameters, while the exact opposite occurred for the samples sprayed with PYRO 4 hydroxyapatite powder. This tendency was measured with both roughness testers. Sample No. 4 with PYRO 4 powder, in particular, presents the highest values for all roughness parameters.

4.2) Thickness measurements using stereoscope

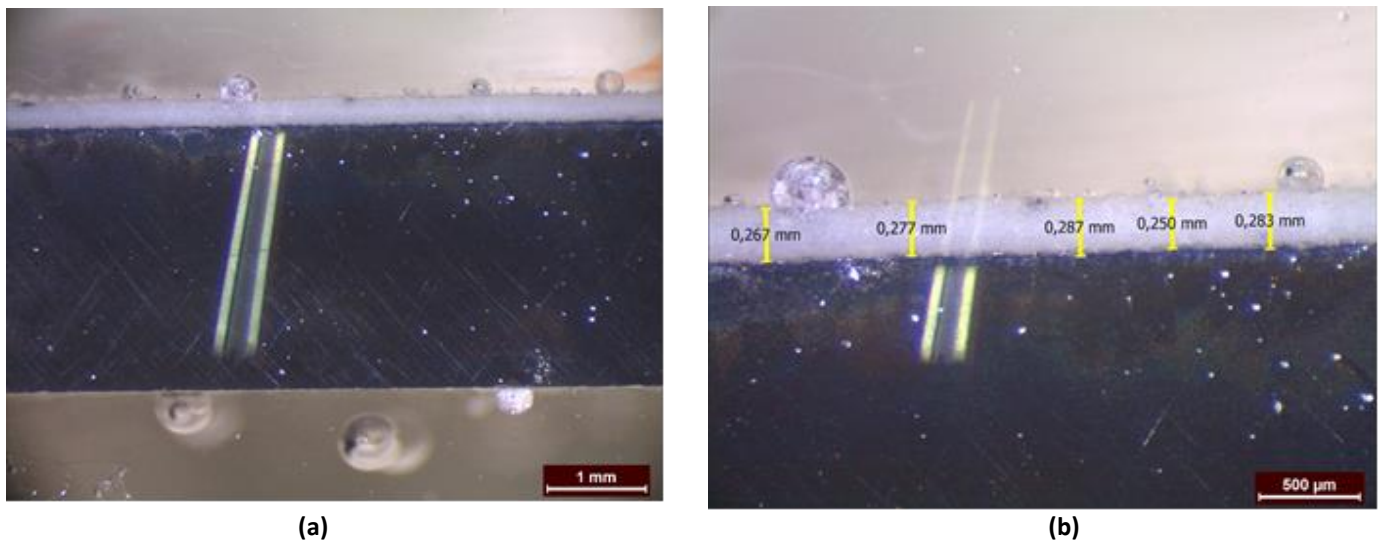


Figure 41: (a), (b) Sample No. 1 with XPT-D-703 hydroxyapatite powder at different magnifications, (b) five thickness measurements obtained by LAS image analysis are shown.

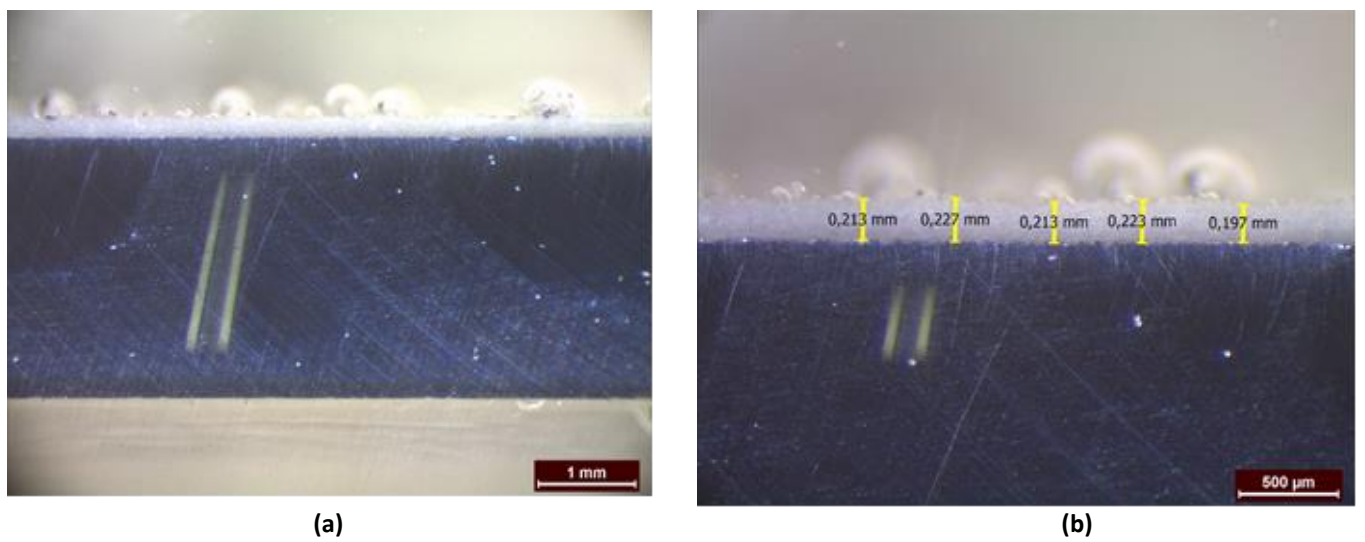


Figure 42: (a), (b) Sample No. 2 with PYRO 4 hydroxyapatite powder at different magnifications, (b) five thickness measurements obtained by LAS image analysis are shown.

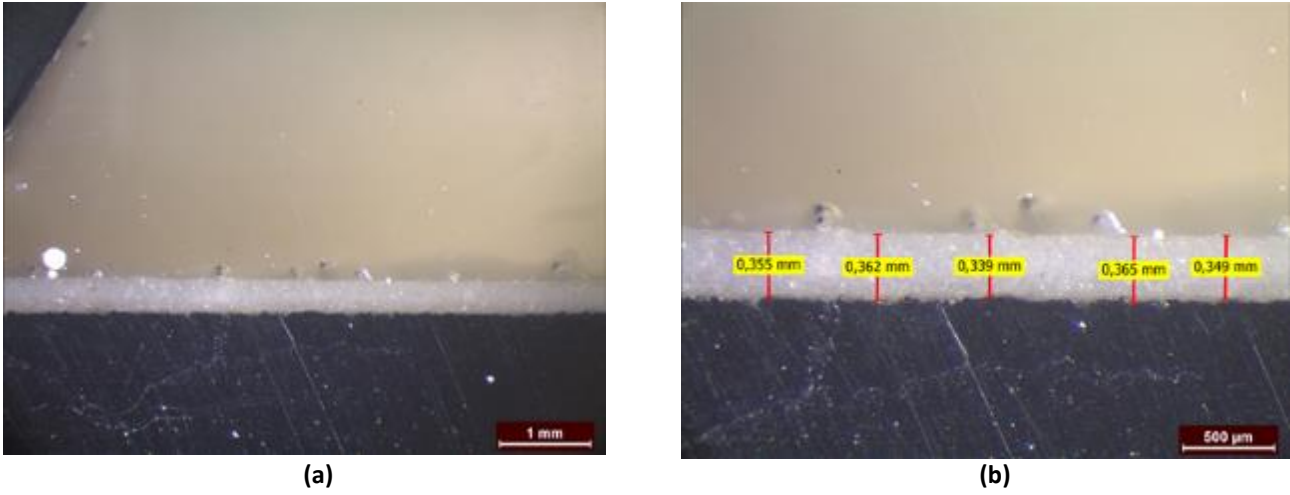


Figure 43: (a), (b) Sample No. 3 with XPT-D-703 hydroxyapatite powder at different magnifications, (b) five thickness measurements obtained by LAS image analysis are shown.

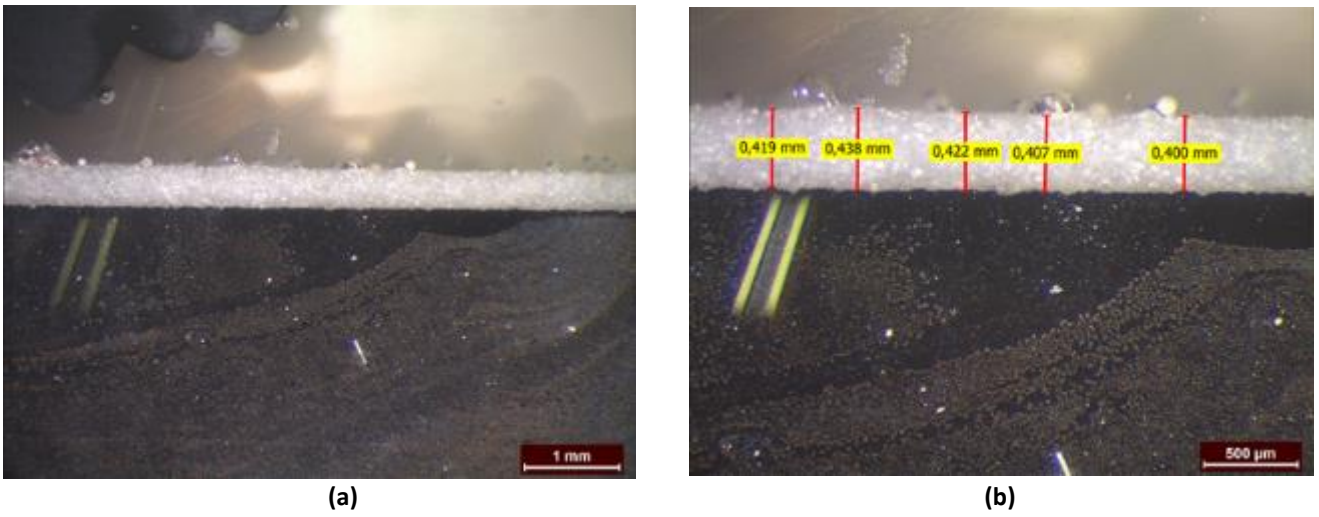


Figure 44: (a), (b) Sample No. 4 with PYRO 4 hydroxyapatite powder at different magnifications, (b) five thickness measurements obtained by LAS image analysis are shown.

Table 11: Average coating thickness of the samples.

No. of Sample	Type of Powder	Average coating thickness (mm)
1	XPT-D-703	0,273
2	PYRO 4	0,215
3	XPT-D-703	0,354
4	PYRO 4	0,417

4.3) Optical microscope

4.3.1) Specimen No. 1

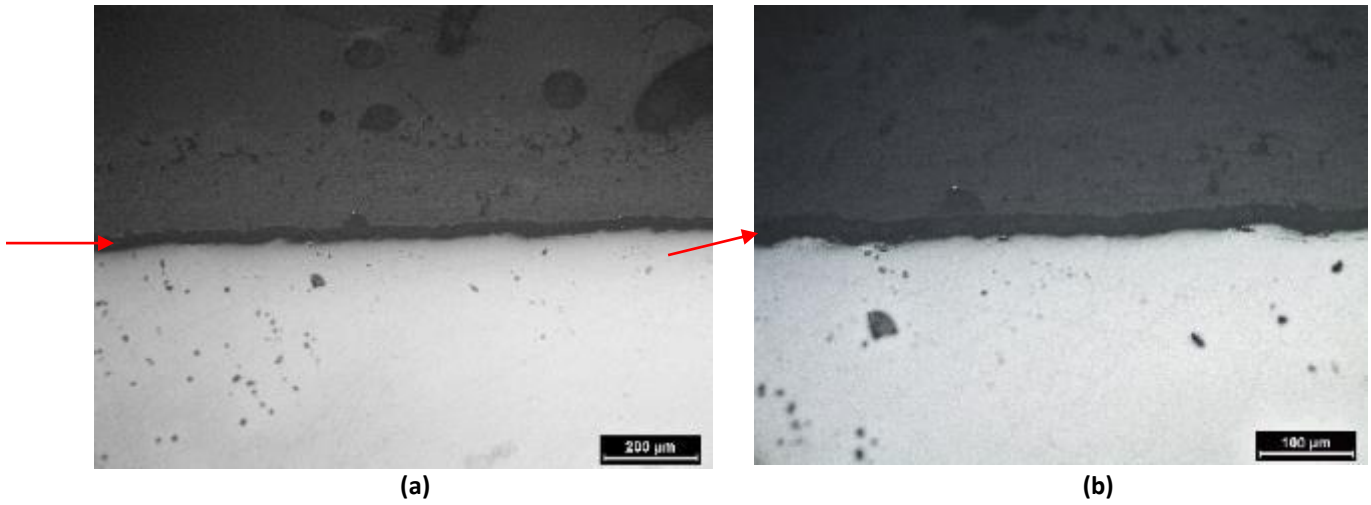


Figure 45: (a), (b) Sample No. 1 with XPT-D-703 hydroxyapatite powder at different magnification. Deep crack in the interface border, between the coating and the substrate, parallel to the substrate, is pointed by the arrow at both pictures.

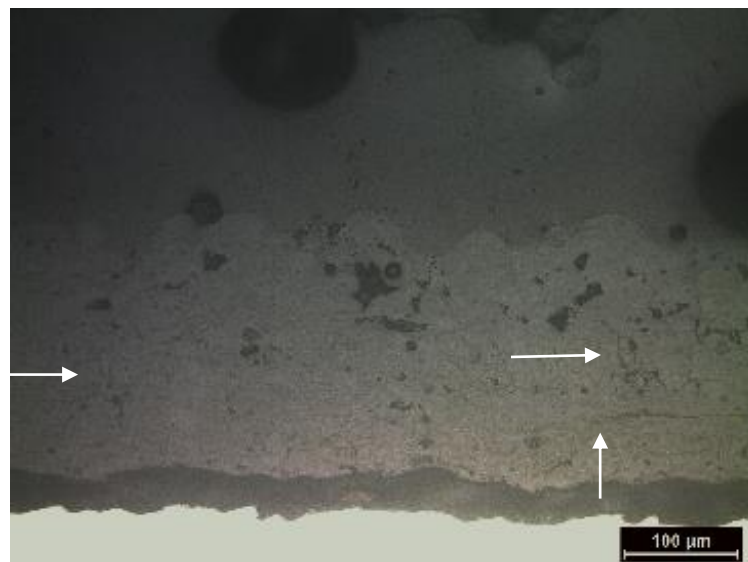


Figure 46: Sample No. 1 with XPT-D-703 hydroxyapatite powder. Microcracks parallel and perpendicular to the interface line.

4.3.2) Specimen No. 2

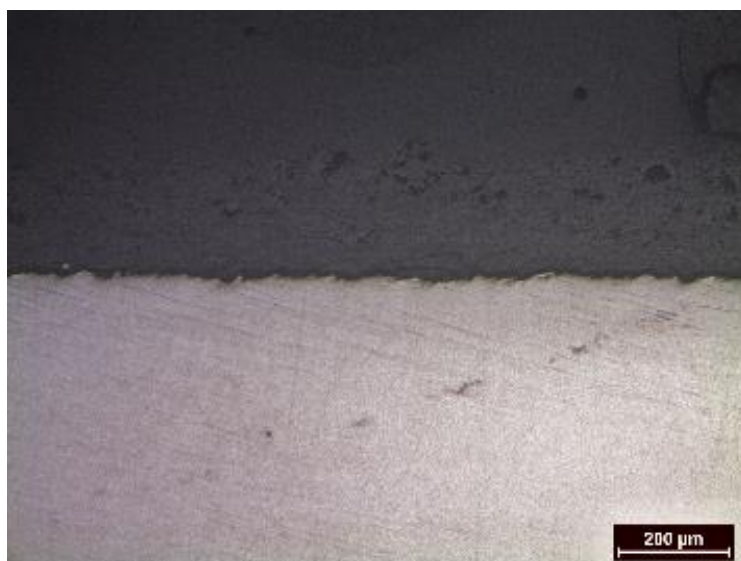


Figure 47: Sample No. 2 with PYRO 4 hydroxyapatite powder.

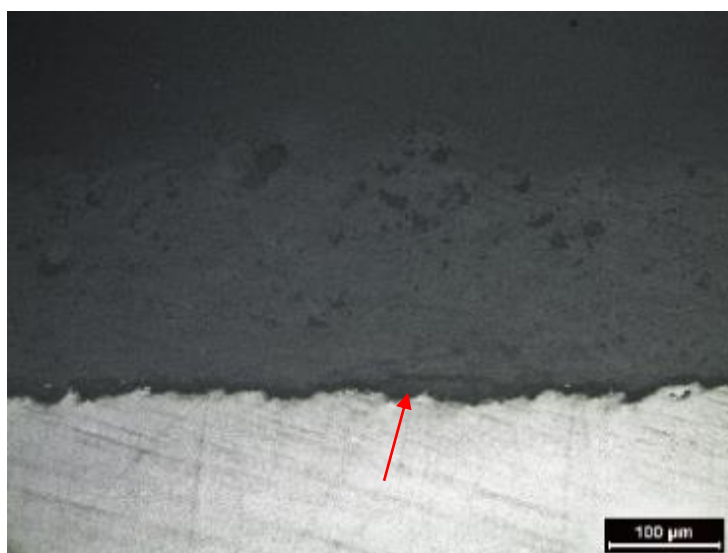


Figure 48: Sample No. 2 with PYRO 4 hydroxyapatite powder. Visible microcrack in the coating parallel to the interface, near the interface border.



Figure 49: Sample No. 2 with PYRO 4 hydroxyapatite powder. Visible microcrack in the coating parallel to the interface.

As it is derived from careful observation of the above pictures, the coating on the specimen with the commercial hydroxyapatite powder has formed a deep crack in the interface between the coating and the substrate and seems to be detached (arrows in figures 45a and 45b). In addition, some microcracks can be observed on both coatings (Figs. 46, 48 and 49), with most of them being parallel to the interface border. As mentioned in the literature, phenomena like these can take place [86] and they could be explained if the difference in coefficient of thermal expansions between the coating and the substrate is considered, which may lead to thermal cracks around the HAP coating and steel interface [87]. Moreover, it has been reported that the surface morphology and the cross-sectional microstructure of the HAP coatings sprayed at higher power and longer stand-off-distances (SOD) reveals enhanced particle melting and spreading, lower porosity and more microcracks [78]. Any perpendicular microcracks to the coating-substrate interface, may indicate the existence of high tensile stress in the coating, along the interface direction. These specific microcracks are produced during either the spraying or the polishing process of the sample [78].

4.3.3) Further stereoscopic and microscopical examination of specimen No.1

However, in order to confirm the origin of appearance of the wide crack in the interface between the coating and the substrate on the specimen No. 1 coated with the XPT-D-703 commercial hydroxyapatite powder, further examination of the specimen was performed. The sample was observed again via stereoscope and optical microscope, on the diametrical side of the cut which had not come in contact with the Discotom and was therefore intact.

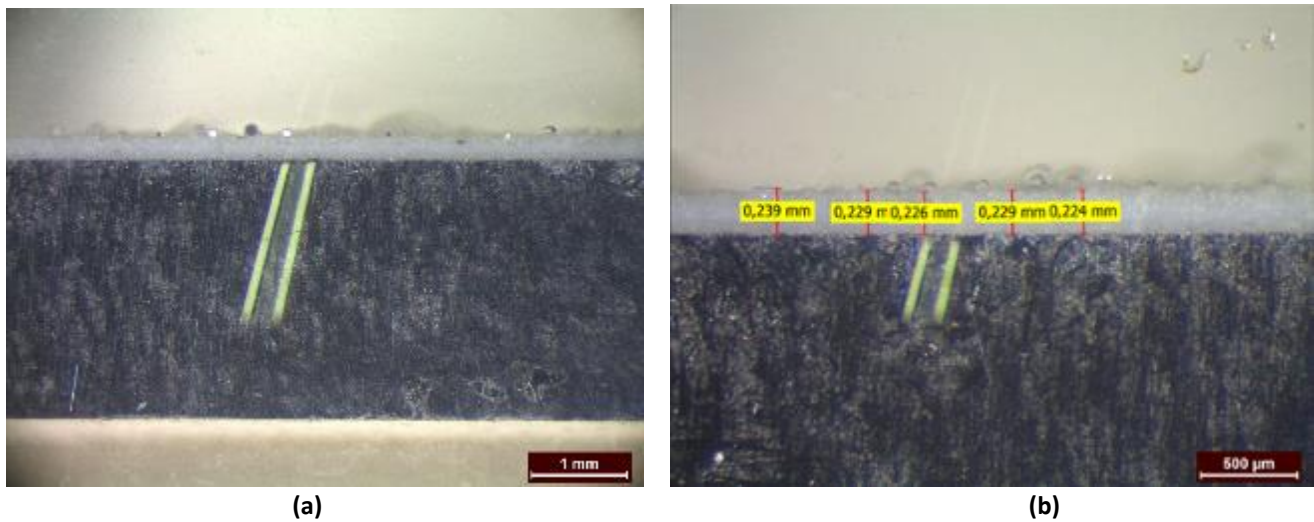


Figure 50: (a), (b) Stereoscopic images of sample No. 1 with XPT-D-703 hydroxyapatite powder at different magnification, (b) with thickness measurements.

Comparison between figures of the same magnification, of the cross-section of the specimen at the side of the cut and its diametrical side, specifically Figs. 41a and 50a, and also Figs. 41b and 50b, revealed no notable differences. The average coating thickness at the intact side of the specimen was measured 0,230 mm, slightly thinner than that of the side of the cut (0,273 mm), which is of not great importance.



Figure 51: Image acquired via optical microscope of the sample No. 1 with XPT-D-703 hydroxyapatite powder. Thin crack in the interface border, between the coating and the substrate, parallel to the substrate.

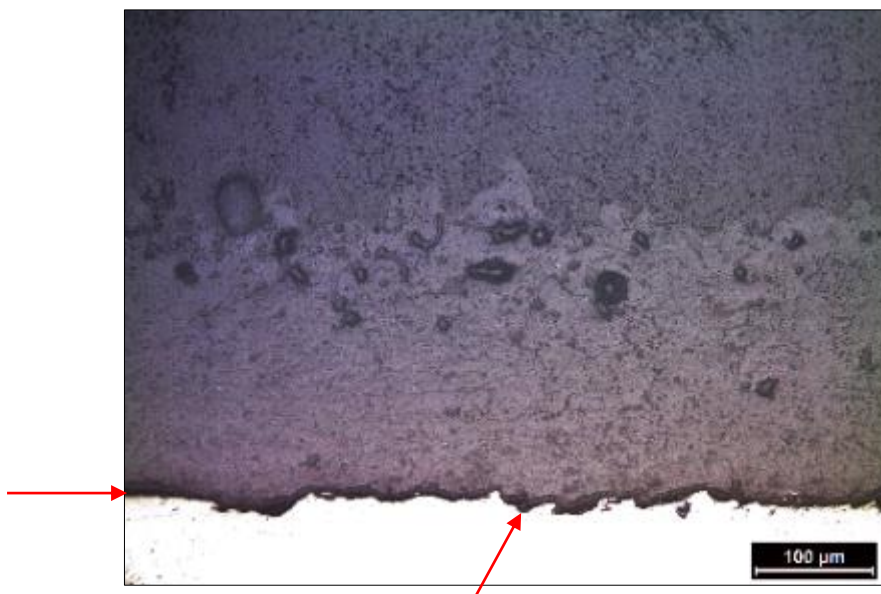


Figure 52: Image acquired via optical microscope of the sample No.1 with XPT-D-703 hydroxyapatite powder. Thin crack in the interface border, between the coating and the substrate, parallel to the substrate.

After observation of Figs. 45a, 45b, 51 and 52, it is evident that the crack in the coating-substrate interface of the sample at the side which had not come in contact with the Discotom, was notably thinner than that observed on the side of the cut. According to this, we can speculate that the cutting process was responsible for aggravation and deepening of the crack. Nevertheless, the fact that cutting of the sample led to such evident differences between the cross-sections of the two diametrical sides, is an indicator of poor adhesion.

4.3.4) Specimen No. 3

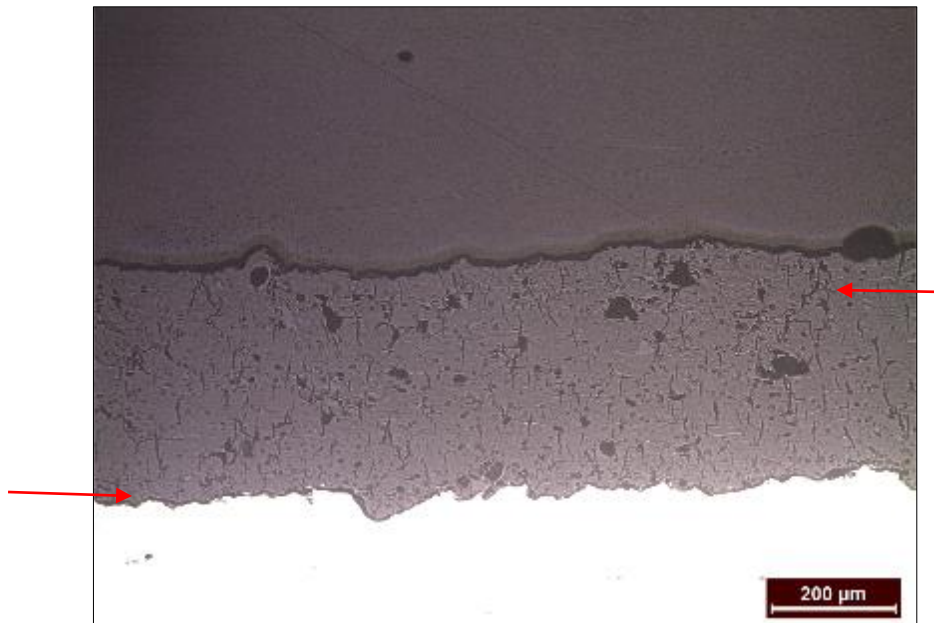


Figure 53: Sample No. 3 with XPT-D-703 hydroxyapatite powder. Microcracks perpendicular to the coating-substrate interface are visible (right-side arrow). No visible crack in the interface border, between the coating and the substrate (bottom-left arrow).

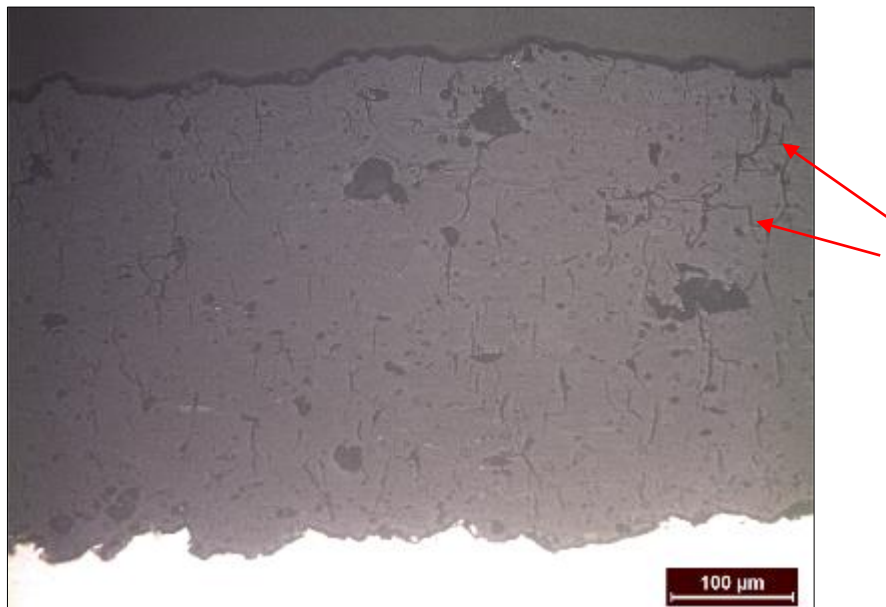


Figure 54: Sample No. 3 with XPT-D-703 hydroxyapatite powder. Microcracks perpendicular to the coating-substrate interface are visible (right-side arrows).

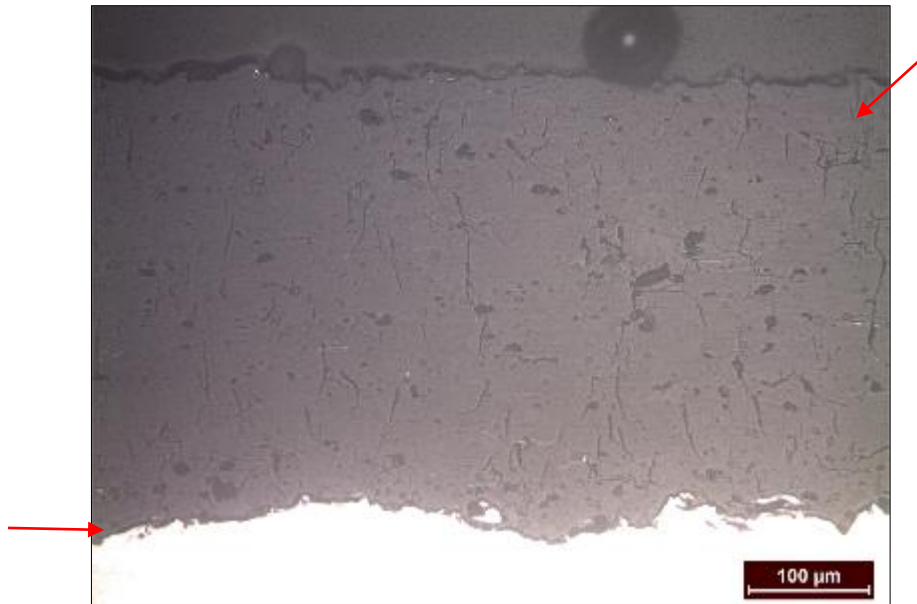


Figure 55: Sample No. 3 with XPT-D-703 hydroxyapatite powder. Microcracks perpendicular to the coating-substrate interface are visible (right-side arrow). No visible crack in the interface border, between the coating and the substrate (bottom-left arrow).

4.3.5) Specimen No. 4

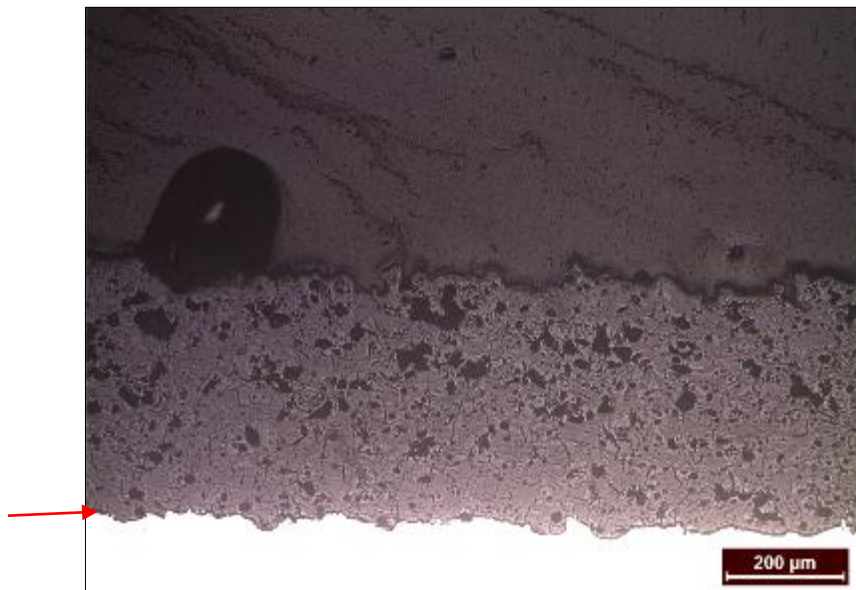


Figure 56: Sample No. 4 with PYRO 4 hydroxyapatite powder. No visible crack in the interface border, between the coating and the substrate (bottom-left arrow).



Figure 57: Sample No. 4 with PYRO 4 hydroxyapatite powder. Microcracks perpendicular to the coating-substrate interface are visible (right-side arrow). No visible crack in the interface border, between the coating and the substrate (bottom-left arrow). Clusters of small pores (white circles) in the coating.



Figure 58: Sample No. 4 with PYRO 4 hydroxyapatite powder. Microcracks perpendicular to the coating-substrate interface are visible (right-side arrow). Cluster of small pores (white circle) in the coating.

Examination of Figs. 53-58, reveals that both the specimens No. 3 and 4 are characterized by enhanced adhesion, probably due to more intense mechanical interlocking. This is evident, as any sign of the characteristic crack at the coating-substrate interface is absent (see also arrows at the bottom-left corner of Figs. 53, 55, 56 and 57).

Furthermore, there are two distinct features that differentiate these specimens from specimens No. 1 and 2, namely the already noticeable increase in porosity and the rise in the amount of microcracks present in the coating. Lower spray power, which was selected for HAP spraying on the specimens No. 3 and 4, leads to insufficient rise in temperature of the sprayed powder particles and therefore, inadequate melting. As a result, spreading of the particle material is incomplete and pores are formed amongst the volume of sprayed material. Thus excess porosity is obvious in Figs. 53-58 in relation to photographed porosity in Figs. 45-49. In addition, it is possible that some of the large pores represent the pullouts of unmelted particle cores during the grinding and polishing process [78].

Regarding the microcracks present in the coating (see also arrows at the right side of Figs. 53, 54, 55, 57 and 58), they are in their majority perpendicular to the coating-substrate interface and they are most likely caused due to release of high pressure within the sealed pores [58]. Alternatively, presence of microcracks could indicate high tensile stresses along the coating-substrate interface direction in the coating, during cooling process [78], either due to restricted contraction of the molten particles or difference in thermal expansion between the coating and the substrate [88].

One last visible feature is the existence of clusters of pores at random locations in the coating, next to pronounced bigger pores (see white circles in Figs. 57 and 58). These pores could be unrealized pores that were produced during spraying due to solidification contraction and splat filling effects [78].

4.4) Scanning Electron microscopy (SEM) and Energy Dispersive Spectroscopy (EDS)

4.4.1) Cross-section related results before immersion into the SBF solution

4.4.1a) Specimen No. 1

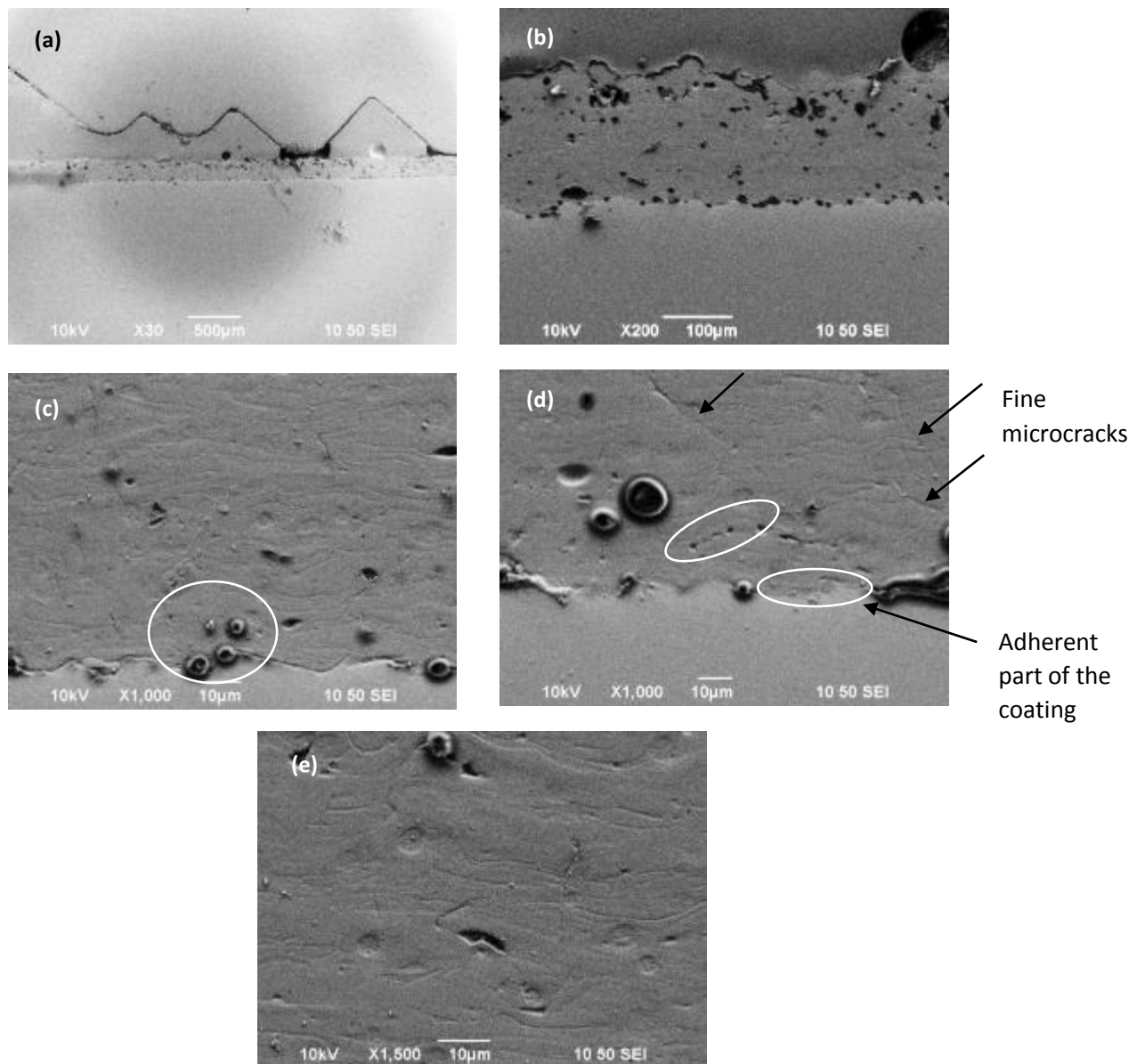


Figure 59: SEM images of cross-section of specimen No. 1, (a) overall cross-section at low magnification, (b) porosity content tends to gather at the upper part of the coating, (c) impurities accumulated at the coating-substrate interface, (d) part of the coating with fair adherence, pores and microcracks, (e) lamellar microstructure and fine microcracks perpendicular to the coating-substrate interface.

The coating of specimen No. 1 appears to be homogenous in terms of its thickness and presents the characteristic microstructure of plasma spray coatings (Fig. 59a). At low magnification (Fig. 59a) the coating also seems to preserve adequate adhesion with the substrate, as no major crack at the coating-substrate interface is evident.

At higher magnification (Figs. 59b and 59c) the coating (cross-section) characteristics become clearer. Greater dark spots are impurities left from the processes of grinding and polishing, which have been deposited onto probable underlying larger pores. It is also possible that some of these large pores represent the pullouts of unmelted particle cores during the abovementioned processes. The porosity level in this coating is half the porosity of its relative specimen No. 3, also prepared from XPT-D-703 commercial hydroxyapatite powder, as a result of higher plasma power and therefore, much better melting of the powder particles. Consequently, the pores are usually small due to splat filling effects and are depicted with small dark spots and the coating exhibits a relatively dense consistency. In addition, the total porosity content has a tendency to concentrate at the upper part of the coating (Fig. 59b).

At even higher magnification (Fig. 59e) the characteristic lamellar microstructure of the plasma spray coatings is evident. Moreover, areas of well-flattened and coherent splats can be seen in which pores and process deposits are dispersed. Satisfying adherence is also obvious, particularly in Figs. 59c and 59d, where pore-free parts of the coating-substrate interface is shown. Distinct pores are shown in Figs. 59c, 59d and 59e. Finally, microcracks are observed, mostly perpendicular to the coating-substrate interface (Fig. 59d). These microcracks are produced during either the spraying or the sample polishing processes and denote high tensile stress, along the coating-substrate interface direction, in the coating during the cooling [78].

4.4.1b) Specimen No. 2

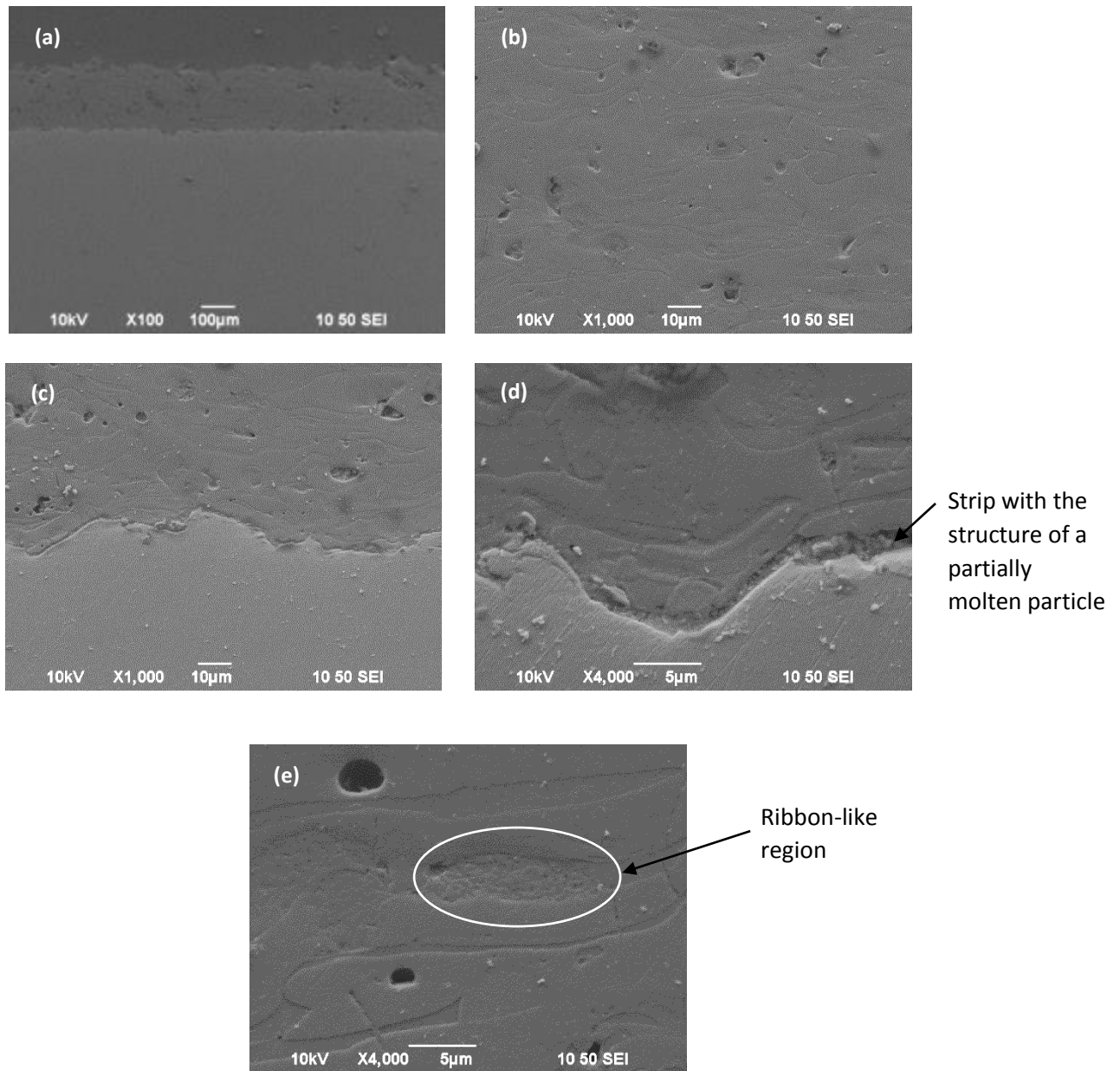


Figure 60: SEM images of cross-section of specimen No. 2, (a) overall cross-section at low magnification, (b) consistent coating with no presence of microcracks, lamellar microstructure, (c) and (d) zone of different phase at the coating-substrate interface, (e) ribbon-like regions, large pore due to pullout of unmelted particle core.

The coating of specimen No. 2 is characterized by homogeneity in its thickness and consistency both in its thickness and also in its length (Fig. 60a). At low magnification (Fig. 60a) the coating also seems to preserve adequate adhesion with the substrate, as there is no sign of detachment of the coating from the substrate. A very neat and impurity-free observational surface has been achieved, so as the porosity content enclosed in the coating is observable with easiness. Once again, larger pores are probably the aftermath of grinding and polishing process, as unmelted particle cores were detached from the coating. In addition, the main body of the coating is free of microcracks (Fig. 60b), which are very fine and are not considered as its dominant characteristic.

At higher magnification (Figs. 60c and 60d), the lamellar structure of the coating is revealed. Moreover, a strip of different microstructure is noticed at the coating-substrate interface. This narrow zone has the structure of a partially molten powder particle and is the effect from gradation of thermal properties between the coating and the substrate.

Finally, at even higher magnification (Fig. 60e) ribbon-like regions [78] are shown, which are intertwined with the neighbouring smooth surfaces and exhibit a quite different microstructure. Specifically, these ribbon-like regions are composed of many nano-grains that are, most possibly, newly recrystallized hydroxyapatite grains. The boundary between these two regions is also smooth.

4.4.1c) Specimen No. 3

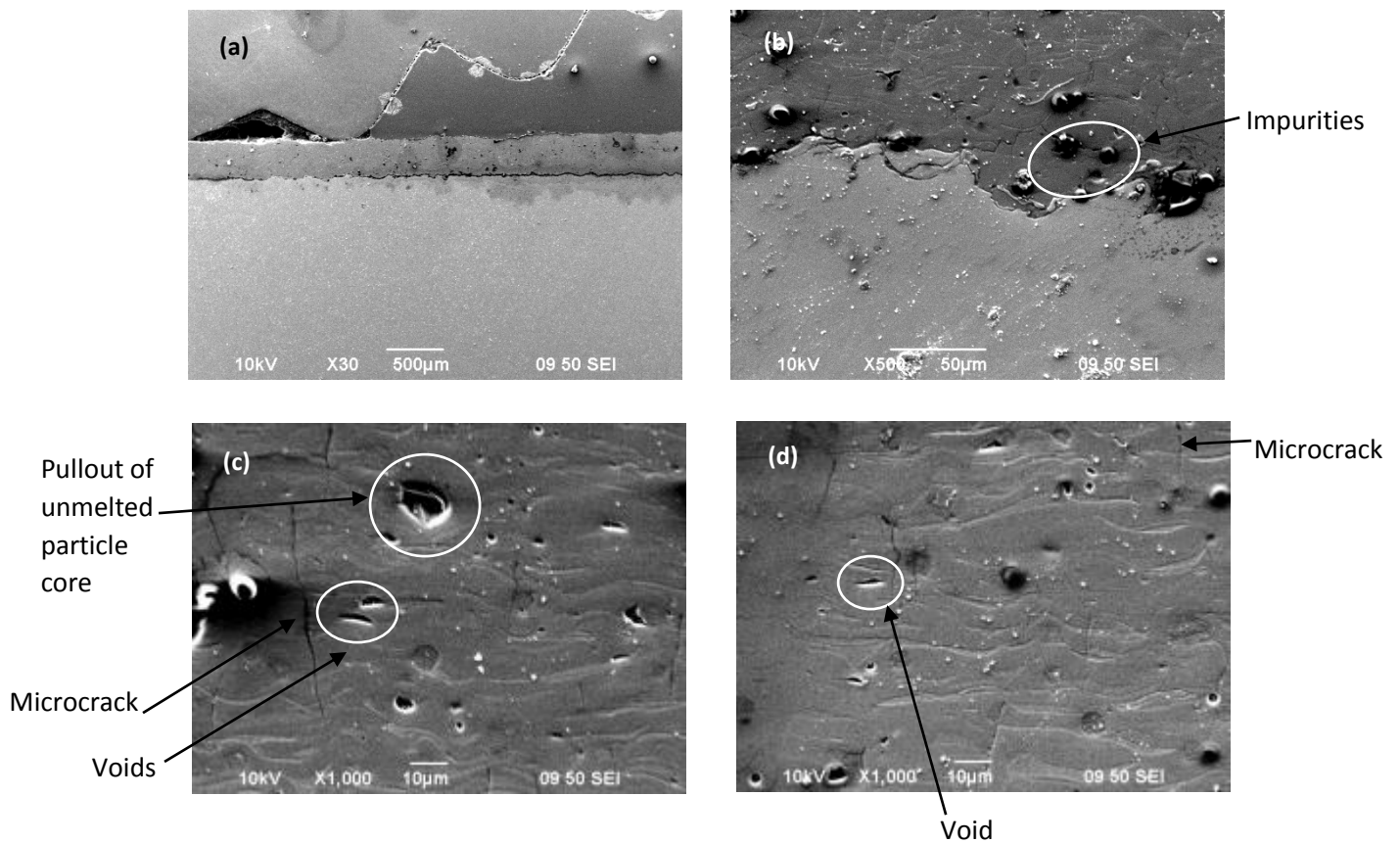


Figure 61: SEM images of cross-section of specimen No. 3, (a) overall cross-section at low magnification, (b) impurities dispersed near or onto the coating-substrate interface, (c) large pore due to pullout of unmelted particle core, (d) lamellar microstructure, voids and microcracks perpendicular to the coating-substrate interface.

The coating of specimen No. 3, similar to specimen No. 1, appears to be homogenous in terms of its thickness and presents the characteristic microstructure of plasma spray coatings (Fig. 61a). However, no preliminary assumption can be made at this low magnification, regarding the adhesion of the coating onto the substrate, due to the existence of areas with indiscernible composition at the coating-substrate interface.

At higher magnification near the border of the interface (Figs. 61b) it is apparent that the interface comprises of clear, pore-free areas, which seem to be adherent to the steel substrate and which are interjected by impurity deposits alongside the interface. Again, the greater dark spots are impurities left from the processes of grinding and polishing, which have been deposited onto presumable underlying larger pores. The porosity level in this coating is twice the porosity of its relative specimen No. 1 (see table 20 in paragraph 4.7.1d), due to utilization of lower plasma power and therefore, achievement of lower processing temperatures during spraying. As a result the as-sprayed powder particles were inadequately melted and were prevented from fully infiltrating the porous nanozones present in the coating [89]. However, the coating appears to be dense and the existent porosity is dispersed throughout the entire body of the coating. White particles observable at Figs. 61b to 61d, are most probably impurities upon which the electron beam of the SEM

is being scattered, thus appearing illuminated.

At even higher magnification (Figs. 61c and 61d) the characteristic lamellar microstructure of the plasma spray coatings is evident. Moreover, areas of well-flattened and coherent splats can be seen in which pores and process deposits are dispersed. Distinct pores are shown in Figs. 61c and 61d, some of which are of undefined shape due to incomplete spreading of the splat or are in the form of lines, also known as voids. Finally, microcracks are observed here, as well, mostly perpendicular to the coating-substrate interface. These microcracks are longer and coarser compared to those existent in the coating of specimen No. 1 and are also found in greater amount.

4.4.1d) Specimen No. 4

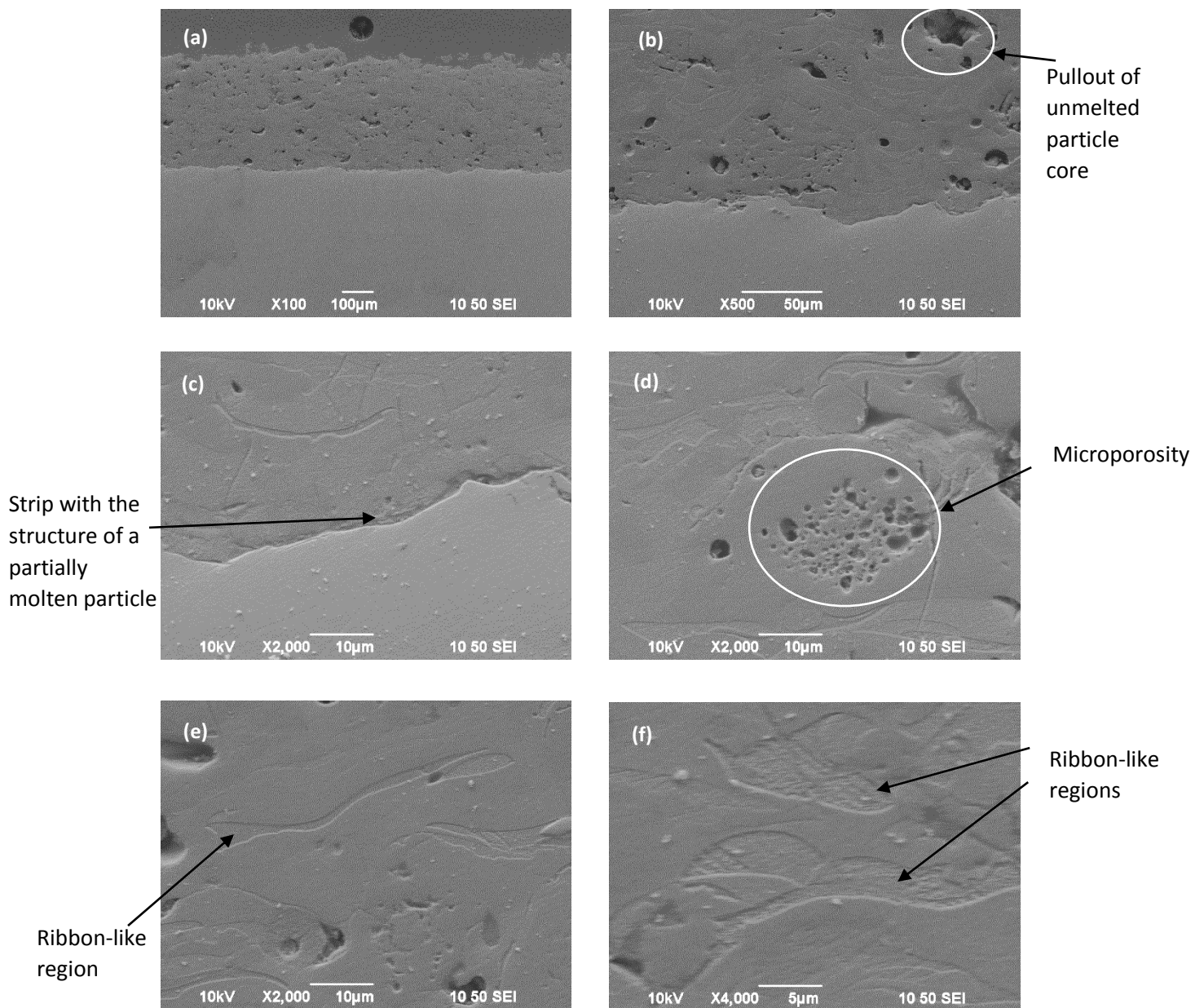


Figure 62: SEM images of cross-section of specimen No. 4, (a) overall cross-section at low magnification, (b) consistent coating with no presence of microcracks, large pore due to pullout of unmelted particle core, (c) zone of different phase at the coating-substrate interface, (d) microporosity, (e) and (f) ribbon-like regions.

The coating of specimen No. 4 is homogeneous throughout its thickness (Fig. 62a) and it bears characteristics of great resemblance with the coating of specimen No. 2. The coating presents strong adhesion to the substrate throughout its length (Figs. 62a and 62b), although the thermally-affected zone, also observable in specimen No. 2, is distinctive at the coating-substrate interface (Fig. 62c). Lack of impurities accumulated on the interface border, additionally makes this phenomena easier to be noticed. On the contrary, it insinuates the presence of such microstructural characteristics at the respective interface borders of the rest of the specimens and our inability to detect them, due to adverse

accumulation of impurities.

Porosity content enclosed in the coating (Figs. 62a and 62b) seems to be of greater amount than that enclosed in the coating of specimen No. 2 (Figs. 60a and 60b). Moreover, larger pores concluded by grinding and polishing process are noted (Fig. 62b), while, at the same time, clusters of micropores with pore diameter of less than 1 μm have been formed (Fig. 62d). Furthermore, a few very fine microcracks are shown (Fig. 62d), which do not constitute major microstructural characteristic.

Finally, at higher magnification (Figs. 62e and 62f), the already mentioned ribbon-like regions of different microstructure are noticed at the coating body amongst the surrounding smooth surfaces.

4.4.2) Cross-section related results after immersion into the SBF solution (observation via stereoscope and optical microscope)

4.4.2a) Specimen No. 1

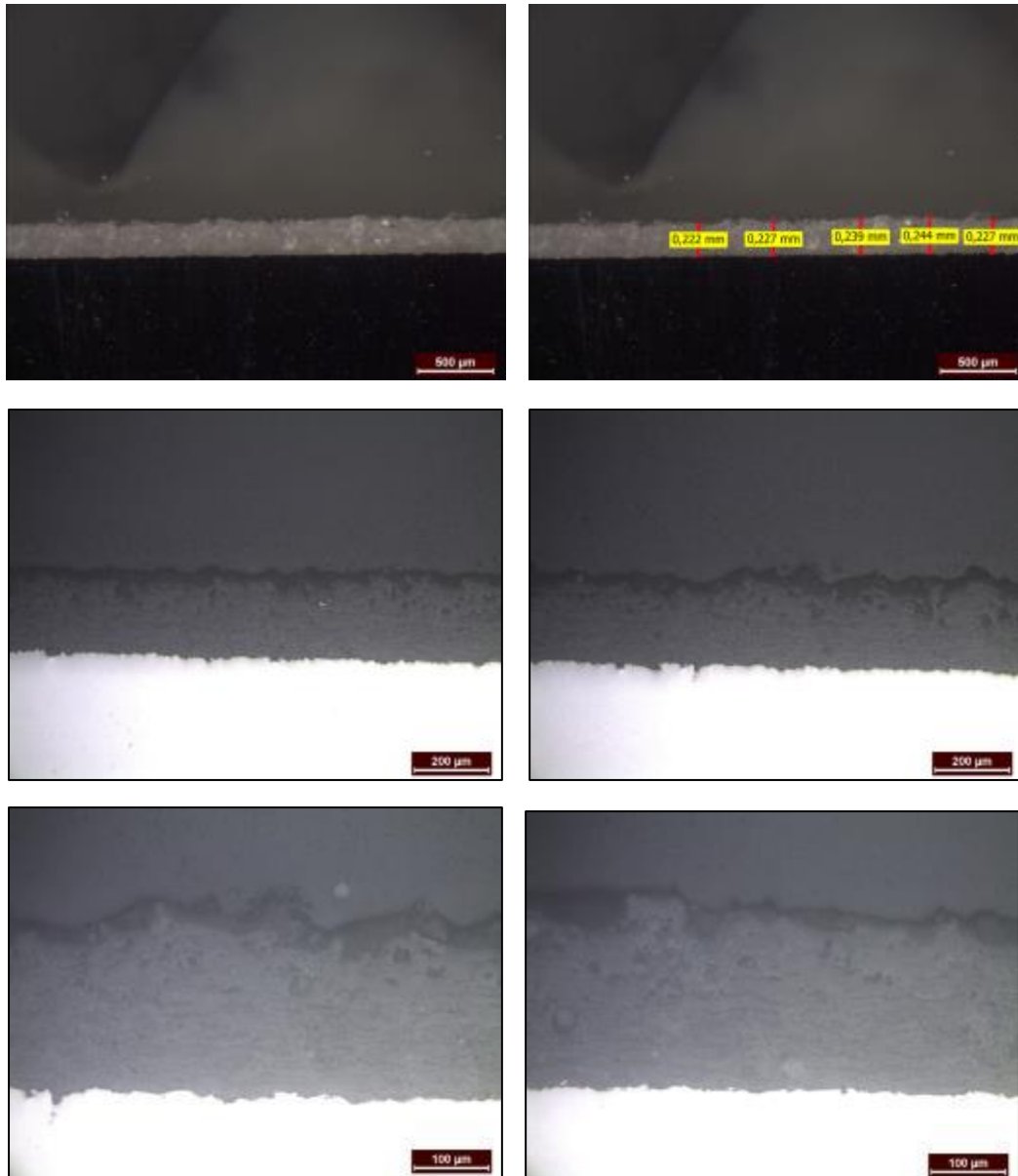


Figure 63: Cross-section of specimen No. 1, after immersion into the SBF solution. Images acquired via stereoscope with thickness measurements included (top row) and via optical microscope at different magnifications (middle and bottom row).

4.4.2b) Specimen No. 2

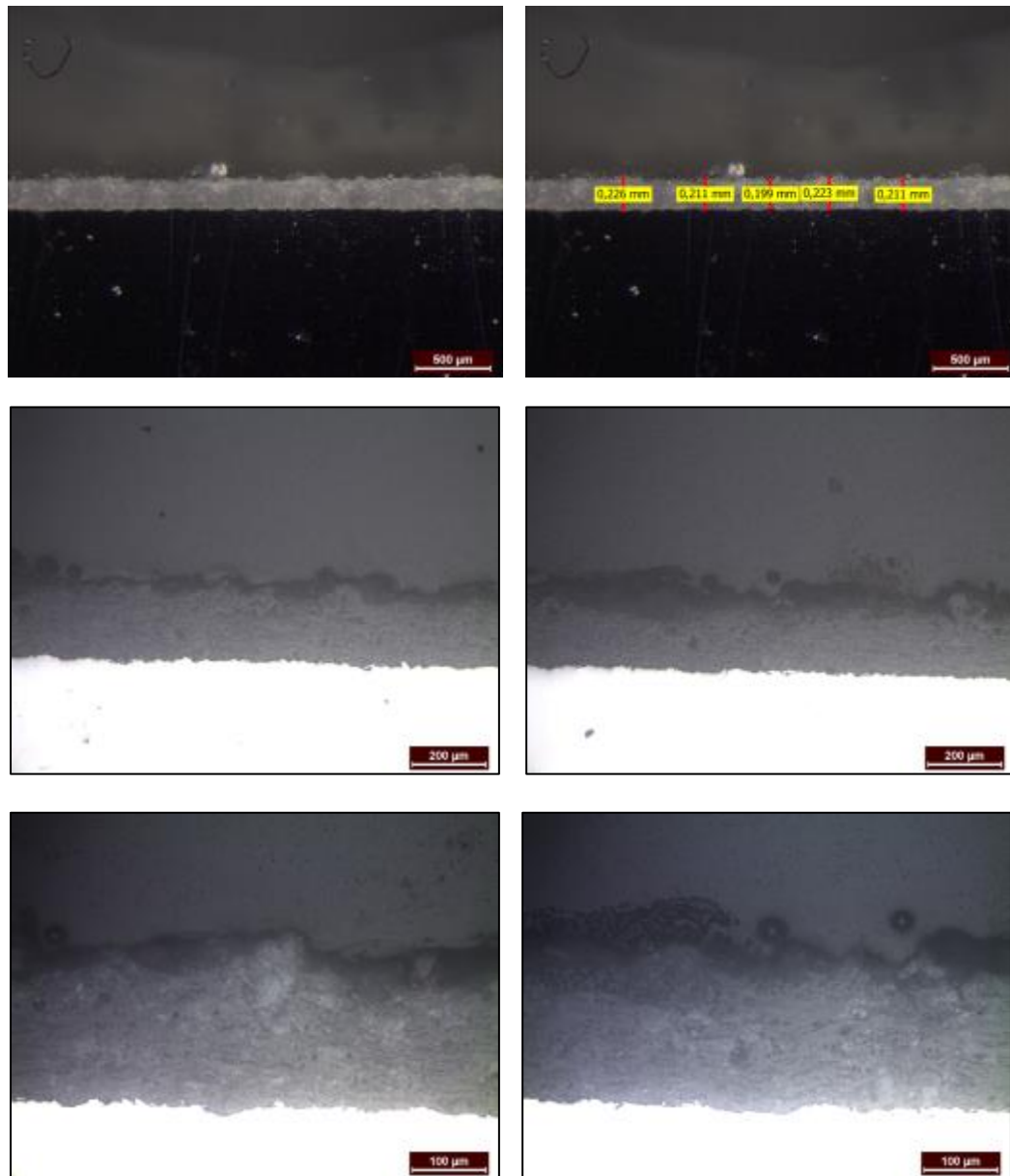


Figure 64: Cross-section of specimen No. 2, after immersion into the SBF solution. Images acquired via stereoscope with thickness measurements included (top row) and via optical microscope at different magnifications (middle and bottom row).

4.4.2c) Specimen No. 3

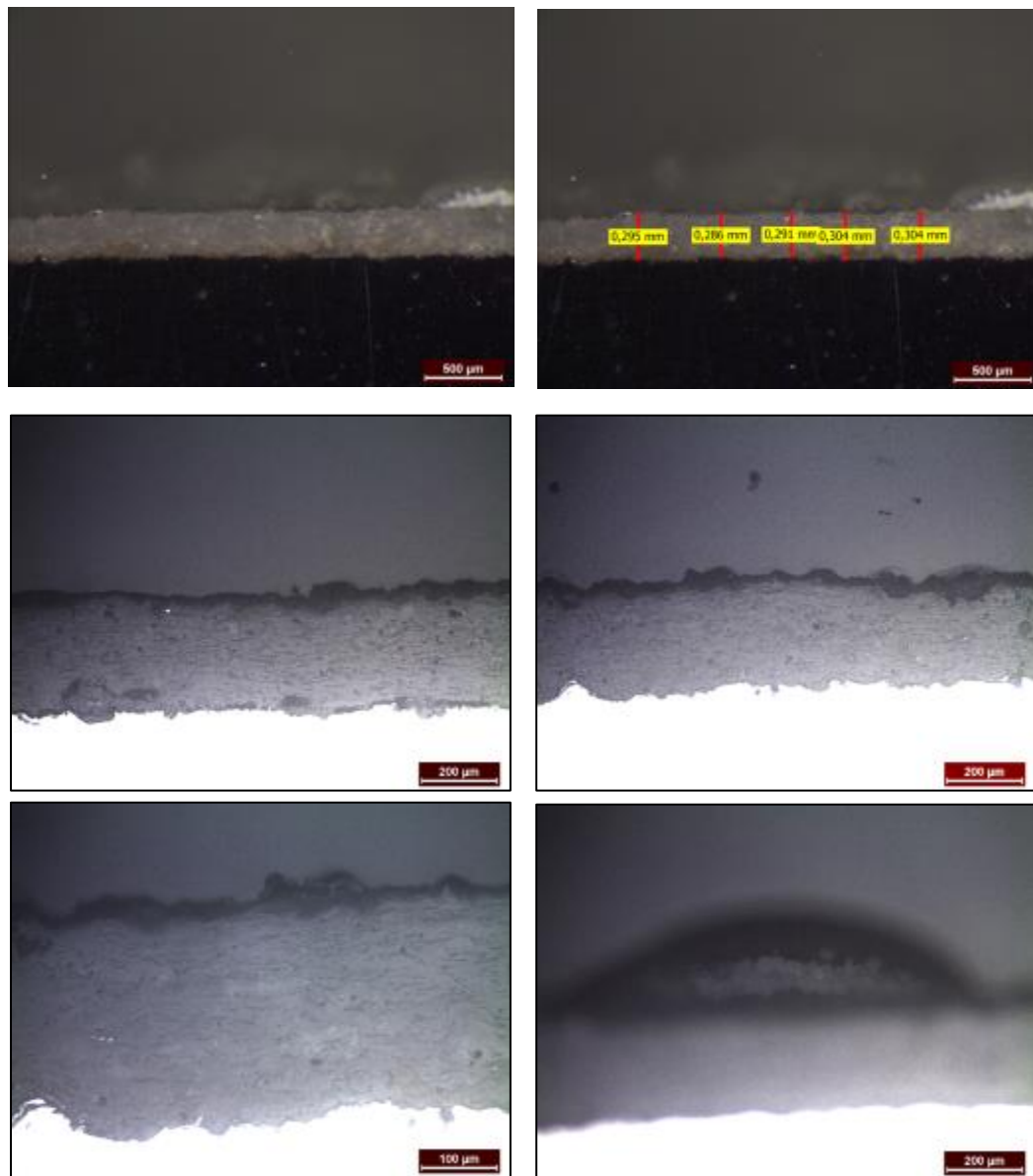


Figure 65: Cross-section of specimen No. 3, after immersion into the SBF solution. Images acquired via stereoscope with thickness measurements included (top row) and via optical microscope at different magnifications (middle and bottom row).

4.4.2d) Specimen No. 4

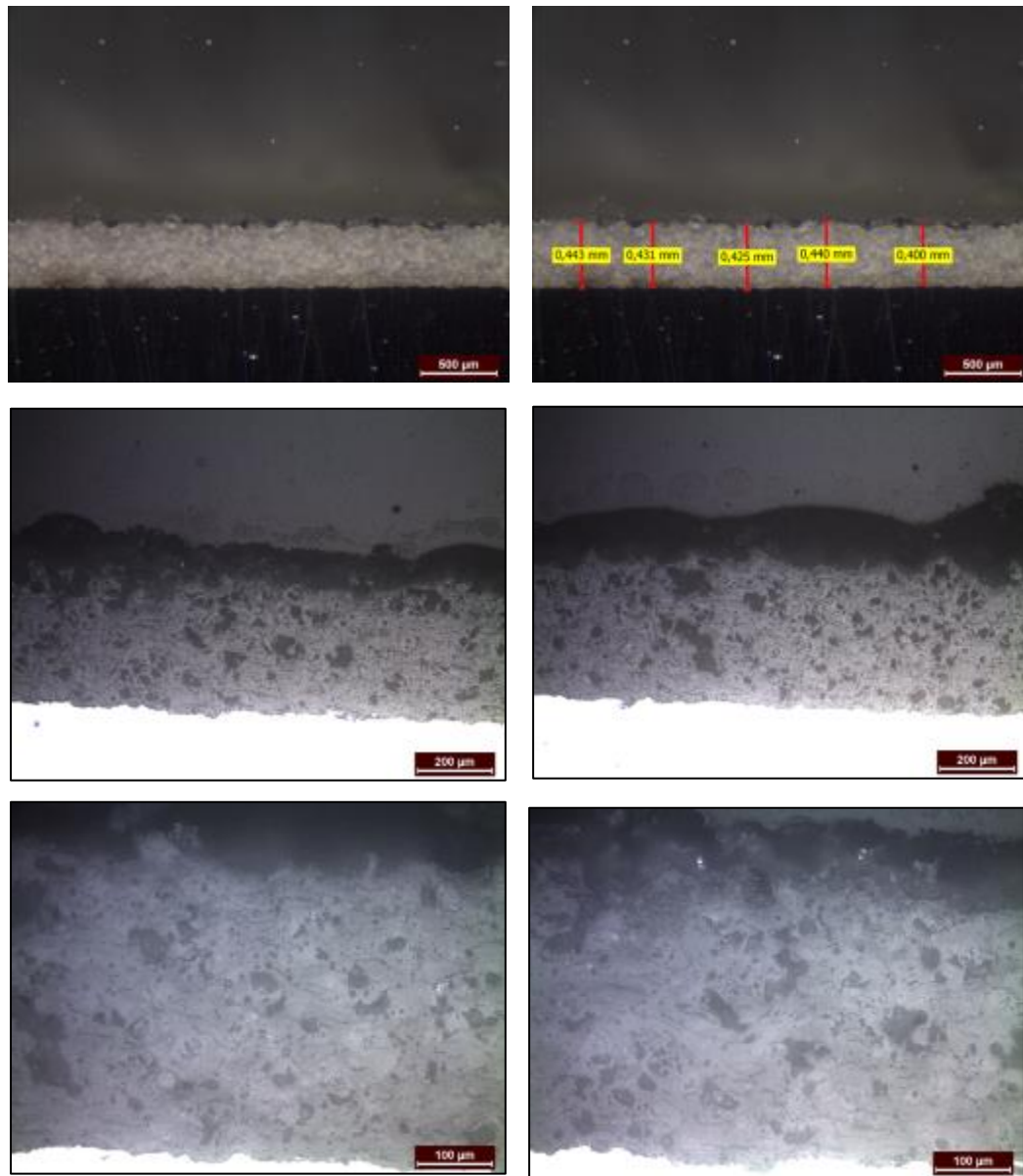


Figure 66: Cross-section of specimen No. 4, after immersion into the SBF solution. Images acquired via stereoscope with thickness measurements included (top row) and via optical microscope at different magnifications (middle and bottom row).

Table 12: Average coating thickness (in mm) of the samples, after immersion into the SBF solution.

No. of Specimen	Type of Powder	Mean coating thickness (mm)
1	XPT-D-703	0,232
2	PYRO 4	0,214
3	XPT-D-703	0,296
4	PYRO 4	0,428

Figures 63 to 66 refer to the cross-sections of specimens No. 1 to No. 4, after soaking for seven days, at 40 °C, into the SBF solution. Observation of the microstructure of the ceramic/SBF interfaces, through the optical microscope revealed the formation of a thin layer on top of the hydroxyapatite coatings on all four specimens.

The SBF when in contact with the ceramic surface reacts and dissolves the amorphous phase present in the coating, with subsequent release of calcium and phosphorous ions that form Si-OH groups on the coating surfaces. These silanol groups combine into an amorphous silica rich phase and are probable to induce heterogeneous nucleation of apatite [90]. In addition, any dissolution of calcium away from the coating requires subsequent recrystallisation of calcium onto the coating surface, in order for the chemical balance inside the solution to be maintained [91]. Therefore, when the ionic activities at the areas adjacent to the active surface of the coating, meaning the coating/SBF interface, reach the solubility of the carbonated apatites, this phase starts to precipitate onto the coating surface in less than seven days. Once apatite nuclei are formed, they grow spontaneously by consuming calcium and phosphate ions from the surrounding SBF solution [90]. Thus, the noticeable layer on top of the coatings is a layer of reaction products, most possibly hydroxy-carbonate apatite (HCA), as mentioned in the literature [92].

As it is presented in the above table (table 12), the overall coating thickness of specimens No. 1 and No. 2 was decreased, in relation to the thickness of these coatings before the immersion of the samples into the SBF solution (see table 11 in paragraph 4.2), although thickness measurements before and after immersion are close. Coating thickness of specimen No. 3 was quite decreased, but this was also the sample that reacted with the surrounding SBF solution (see paragraph 4.4.4c), thus no further deduction can be drawn upon thickness reduction.

On the contrary, overall coating thickness of specimen No. 4 was increased, which could be due to higher retained crystallinity of the coating after plasma spray process. According to the literature [90], lower dissolution rates are noted on account of the high level of crystalline HAP present on the coating, while HAP coatings tend to become more crystalline with immersion time, as a result of loss of the non-crystalline HAP phases. This comes in agreement with the respective data concerning crystallinity of specimen No. 4, acquired through X-ray diffraction. X-ray diffraction spectra (see Fig. 89 in paragraph 4.5.3) show that the intensity of the diffracted X-rays of PYRO 4 sprayed powder and specimen No. 4 are in close proximity and thus, crystallinity levels are close.

4.4.3) Coating surface related results before immersion into the SBF solution

4.4.3a) Specimen No. 1

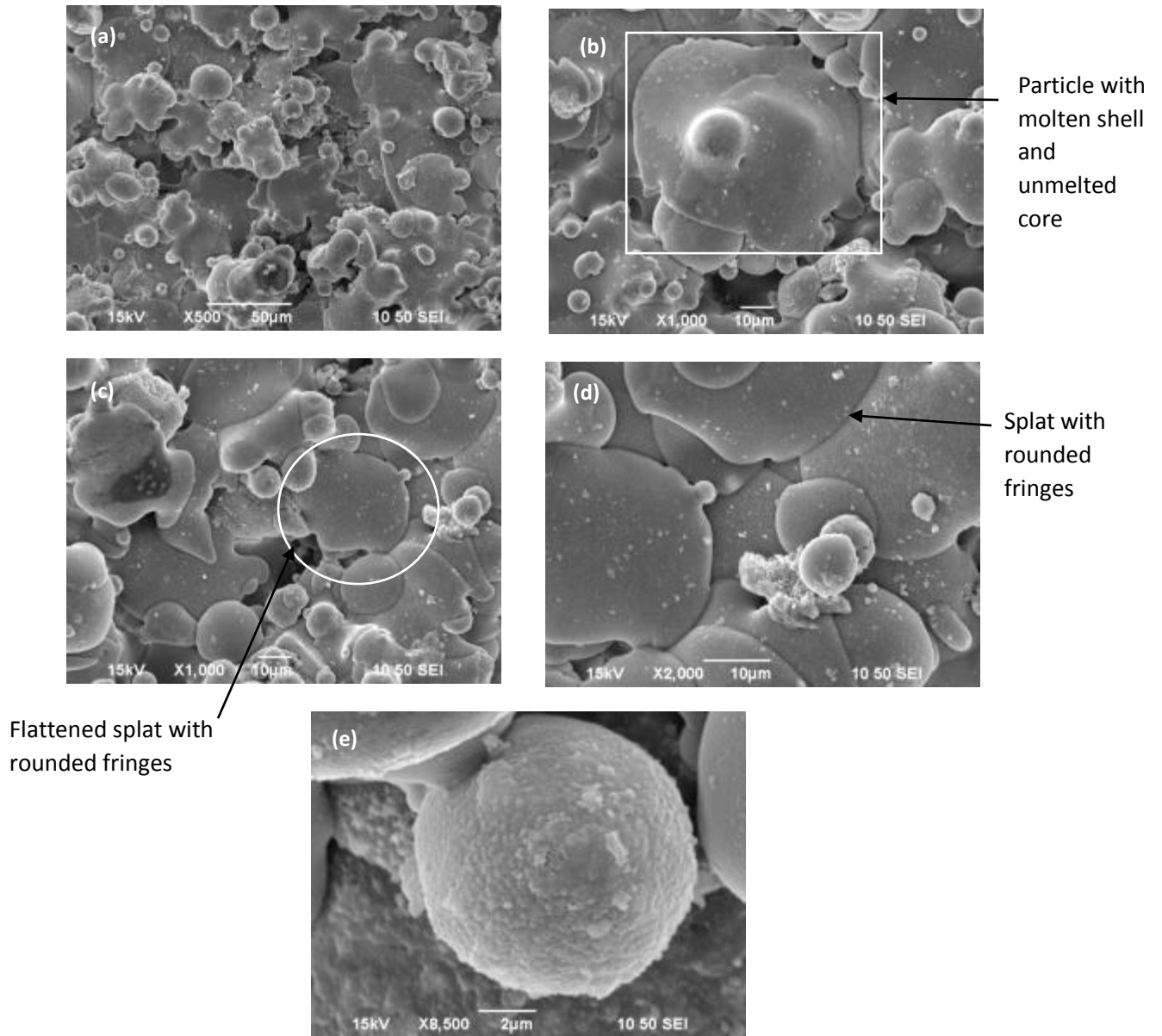


Figure 67: SEM images of the coating surface of specimen No. 1, prior to immersion into the SBF solution at different magnifications, (a) porous microstructure, dispersed unmolten and semi-molten particles, (b) semi-molten particle with molten shell and unmolten core, (c) and (d) well-flattened splats with rounded fringes, (e) microstructure of a partially molten particle.

Fully molten particles, also known as splats are observed. These splats are in general well-flattened, with distinguishable rounded fringes, on the outer surface layers of the coating (Figs. 67a to 67d). Splat boundaries are also obvious where splats are accumulated and overlap one another. Although higher plasma power was used for utilization of the specific coating, there are no splats showing any destroyed morphology [58]. Furthermore, a mean splat diameter seems to be 25 μm .

A porous net emerges throughout the overlapping splat layers (Fig. 67c), due to local insufficient melting of the particles and therefore, inadequate splat-to-splat cohesion. This porous microstructure is characteristic for plasma spray coatings and is noticeable at even lower magnifications of the coating (Fig. 67a).

On top of these well-flattened splats, semi-molten feedstock particles are noticed (Fig. 67b). More specifically, the shell of these particles has been melted, but the core has been kept intact, thus presenting a bimodal microstructure.

In addition, unmolten particles, partially melted particles of spherical morphology and also smaller fractions of partially melted particles, which were utilized upon collision with exact previous as-sprayed layer of feedstock, are dispersed over the surface of the splats. In general, these partially melted particles seem to be of the same order of magnitude (Fig. 67a). However, at greater magnifications (Figs. 67b to 67d) partially melted particles of different magnitude order appear, while at even greater magnification (Fig. 67e) the microstructure of a partially melted particle can be observed.

4.4.3b) Specimen No. 2

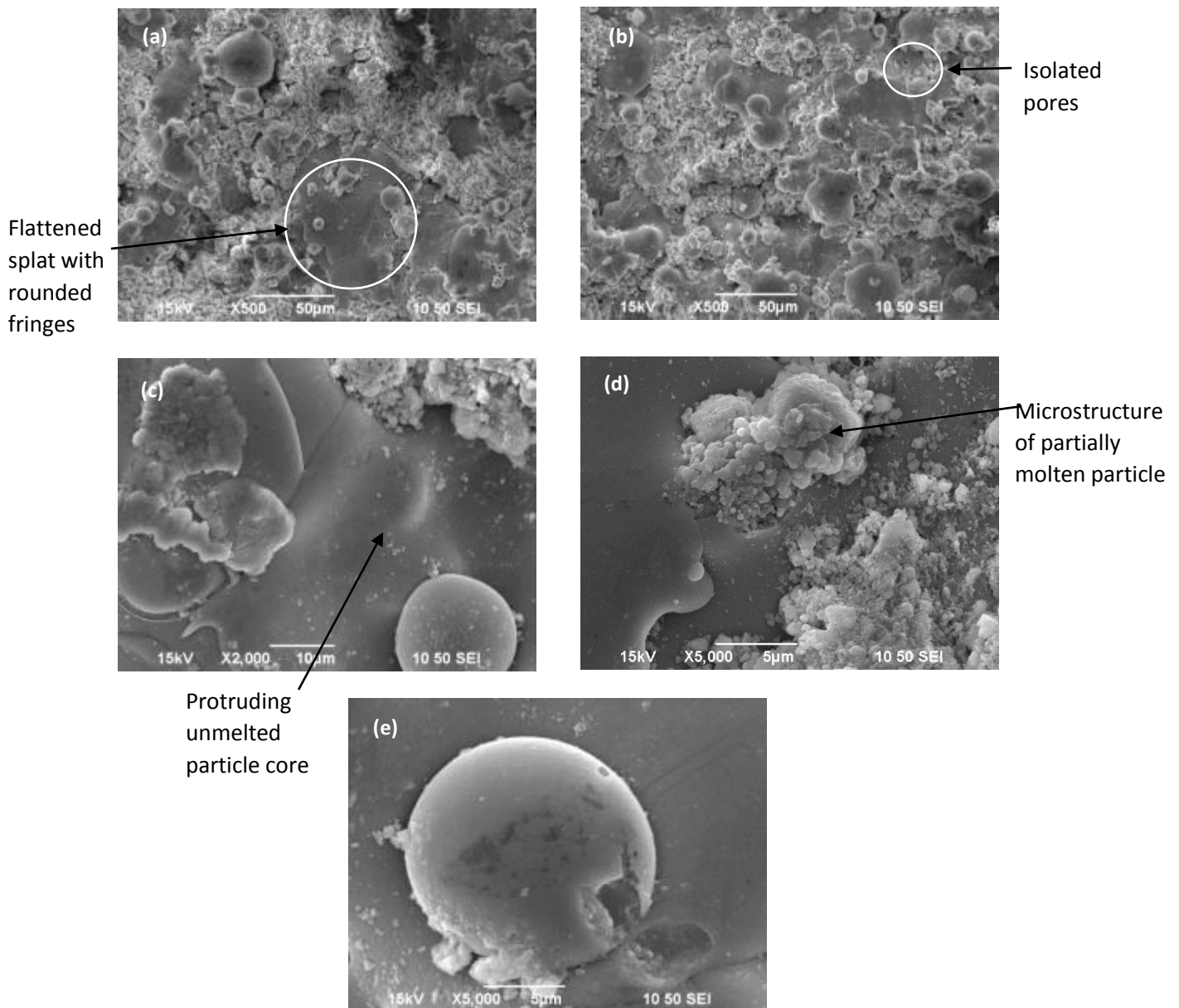


Figure 68: SEM images of the coating surface of specimen No. 2, prior to immersion into SBF solution at different magnifications, (a) porous microstructure, dispersed unmolten and semi-molten particles, (b) semi-molten particle with molten shell and unmelted core, (c) and (d) well-flattened splats with rounded fringes, (d) and (e) microstructure of a partially molten particle.

At first glance a finer and more homogenous microstructure is observed (Figs. 68a and 68b). Splats can be clearly observed (Fig. 68a) and are generally well-fattened with rounded fringes. Protruding remnants of semi-molten particle cores are also noted (Fig. 68c), while their molten shells have gone through adequate spreading and act as a binder, as well as splats.

The majority of the coating surface is dispersed with partially molten particles or fractions of partially molten particles that were shattered upon impact with the underlying as-sprayed material. In figure 68d, a partially molten particle can be observed in great detail. More specifically, some of the individual nanosized particles of the feedstock became rounded but they did not coalesce during spraying. Therefore, the porous structure of the agglomerated powder feedstock has been preserved in the coating microstructure [89]. Isolated open pores can also be seen upon splats (Fig. 68b). However, the majority of porous microstructure in the coating is speculated to originate from insufficient melting of primarily porous powder particles, as stated above, rather than poor cohesion amongst the splats.

In figure 68e, an unmelted particle is clearly observed. The nanosized particles of the feedstock that were agglomerated in order to form this particle with diameter of around 15 μm , are shown both inside the cracked region of the particle and also attached at its shell. Their size does not exceed 2 μm in diameter.

4.4.3c) Specimen No. 3

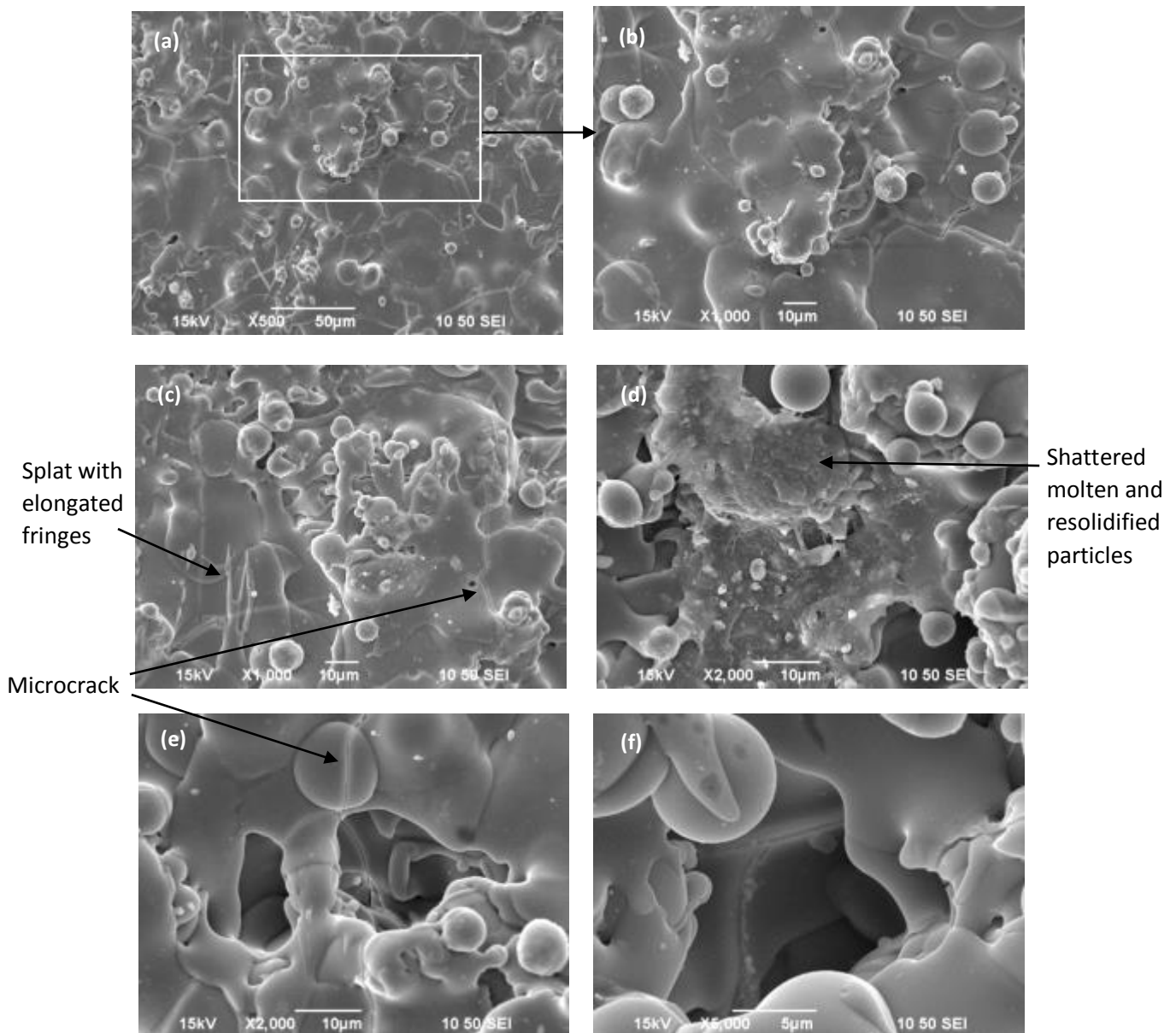


Figure 69: SEM images of the coating surface of specimen No. 3, prior to immersion into SBF solution at different magnifications, (a) well-flattened splats that form glassy surfaces, (b) zoom-in of an (a) region, (c) splats with elongated fringes, presence of microcracks, (d) shattered molten and resolidified particles, (e) and (f) interior of an open pore.

At lower magnifications (Figs. 69a and 69b) a more consistent coating surface is observed. This idea comes in agreement with the findings from the mercury porosimetry regarding specimen No. 3, for which the total porosity percentage was found to be 0,2 (see table 21 in paragraph 4.7.2d), smaller than the relative percentages for the rest specimens. Pores exist although the characteristic porous microstructure is not profound.

The existent splats (Figs. 69a to 69c) are well-flattened and form characteristic glassy surfaces [93], underneath which unmelted particle cores are protruding (Fig. 69b). The

majority of the splats is characterized by elongated fringes (Fig. 69c) and also discernible splat boundaries between overlapping splats. Moreover, some very fine cracks are present within particular splats (Figs. 69c and 69e), which could be due to production of amorphous phases while spraying. Plasma spraying of the powder feedstock at lower plasma power and longer spraying distance justify the presence of excess of unmelted powder particles of spherical morphology and also the deformed shape of splats with elongated fringes. In addition, partially molten particles and also shattered molten and resolidified particles due to impact upon the underlying sprayed material are noticed (Fig. 69d).

Finally, the interior of an open pore is depicted in Figs. 69e and 69f, at higher magnification.

4.4.3d) Specimen No. 4

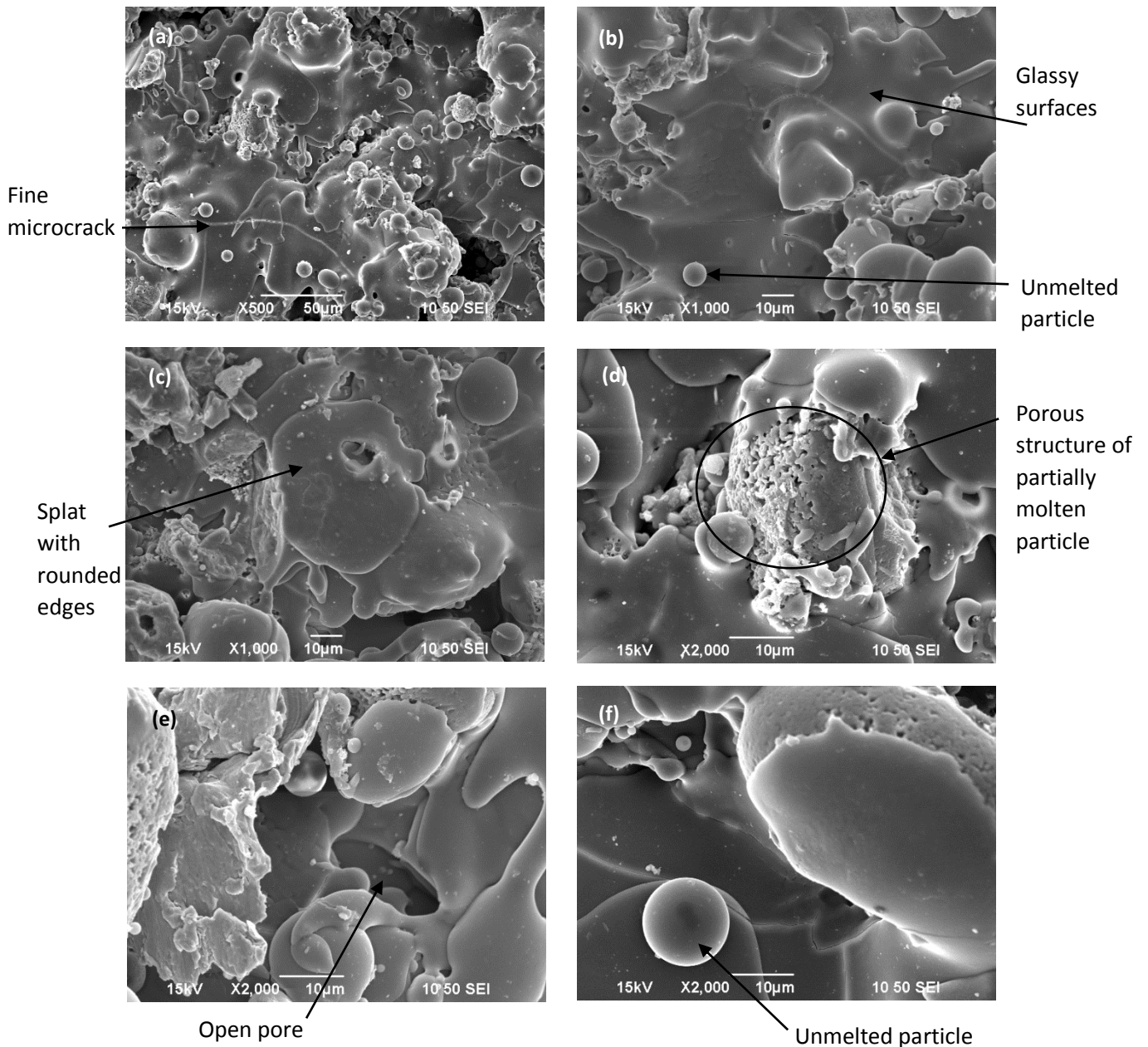


Figure 70: SEM images of the coating surface of specimen No. 4, prior to immersion into SBF solution at different magnifications, (a) porous coating, fine microcrack within flattened splats, (b) glassy surfaces and unmelted or semi-molten particles, (c) splat with rounded fringes, (d) porous structure of partially molten powder particle, (e) open pore, (f) unmelted particle, semi-molten particle covered by flattened splat.

At first sight a rough and porous surface coating is observed (Fig. 70a). The observed splats (Figs. 70a to 70c) are well-flattened and form characteristic glassy surfaces [93]. The edges of the splats are rounded and do not form elongated fringes, unlike specimen No. 3, despite the same spraying parameters. The splat boundaries are mostly indiscernible, although some very fine cracks that are present within particular splats are detected (Fig.

70a). Aside from well-flattened splats, there are also those that present bimodal structure and are a result of incomplete melting of the impinging powder particles during the plasma spray process. Underneath these splats, an unmelted or semi-molten particle core projects from the rest splat surface (Figs. 70b and 70c).

Unmelted powder particles are also present (Figs. 70a, 70b and 70f). Moreover, likewise specimen No. 2, there are partially molten powder particles, which preserve the porous structure of the agglomerated powder feedstock in the coating microstructure. One such particle is shown in Fig. 70d, where the individual nanosized particles of the feedstock have been agglomerated into a larger particle, whilst creating a porous net within the particle. A similar particle is presented in Fig. 70f, the lower side of which is covered by a splat. The microstructure in general, seems to be a combination of well-flattened splats and partially melted particles at equal quantities.

Apart from the existing pore structure of partially melted particles, open pores are observed upon the splat surfaces (Figs. 70a and 70b) and also locally where the splats lack cohesion due to insufficient melting and/or spreading of the particles (Fig. 70e). Finally, the interior of an open pore is depicted in Fig. 66e at higher magnification.

4.4.3e) Energy Dispersive Spectroscopy (EDS)

EDS analyses were performed on the coatings of all the specimens. Some of the acquired spectra are presented below (Figs. 71 to 74), one for each specimen, respectively.

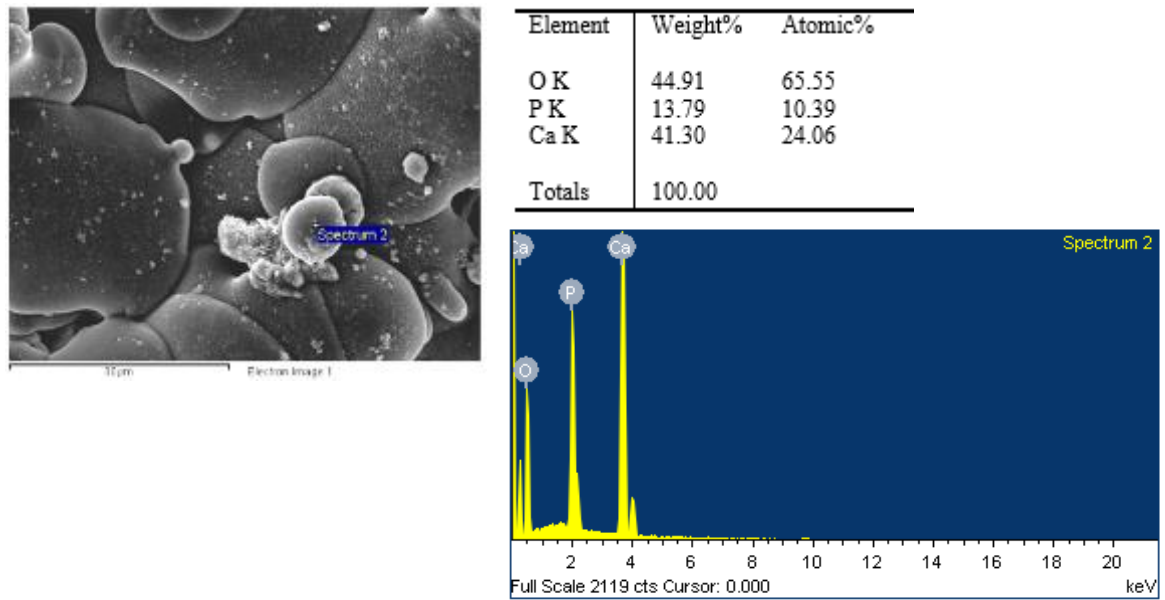


Figure 71: EDS spot analysis on coating of specimen No. 1, before immersion into the SBF solution.

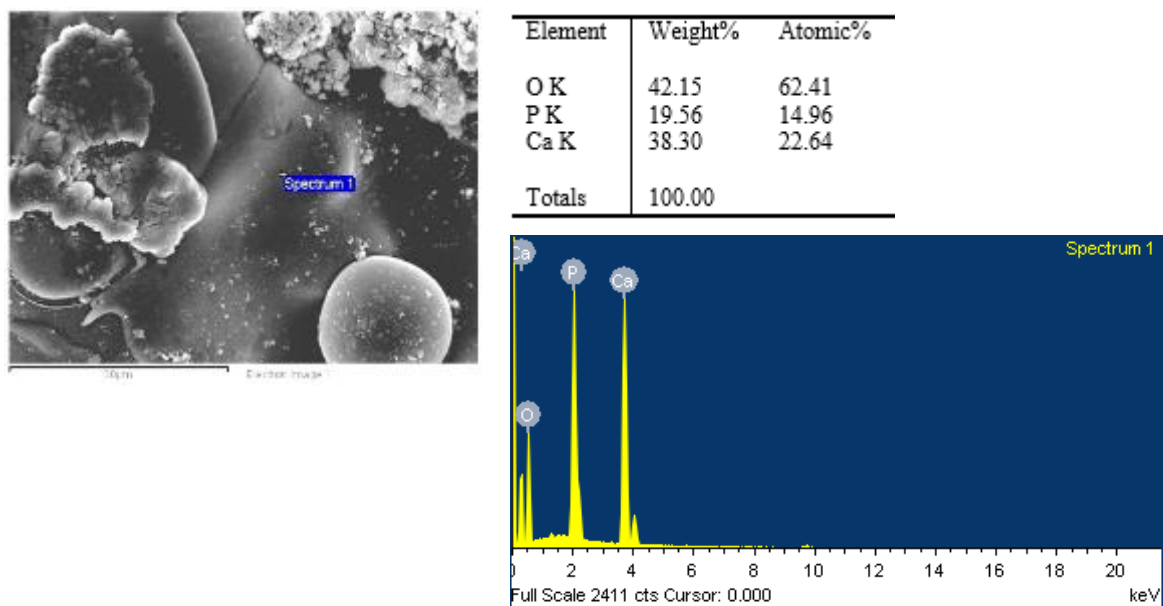
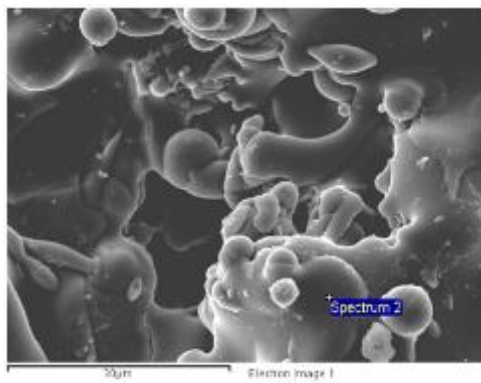


Figure 72: EDS spot analysis on coating of specimen No. 2, before immersion into the SBF solution.



Element	Weight%	Atomic%
O K	36.57	56.71
P K	22.08	17.69
Ca K	41.35	25.60
Totals	100.00	

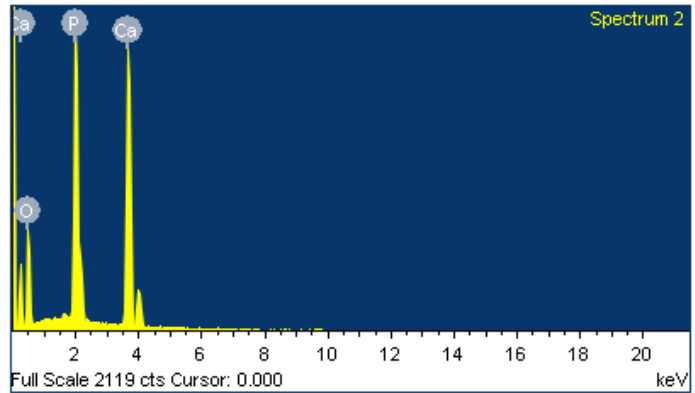
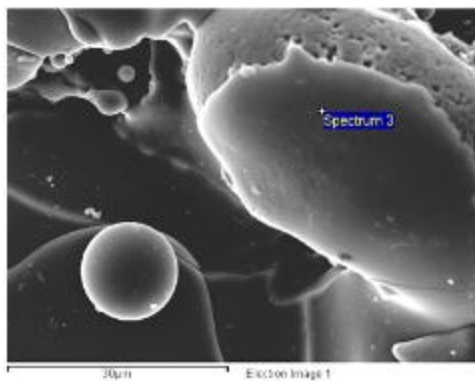


Figure 73: EDS spot analysis on coating of specimen No. 3, before immersion into the SBF solution.



Element	Weight%	Atomic%
O K	30.23	49.76
P K	22.77	19.36
Ca K	47.00	30.88
Totals	100.00	

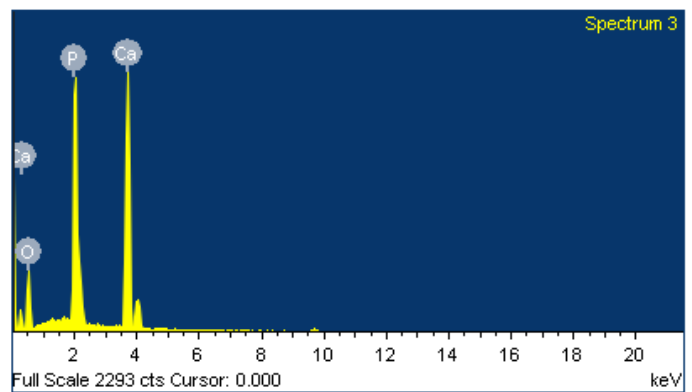


Figure 74: EDS spot analysis on coating of specimen No. 4, before immersion into the SBF solution.

From the EDS spot analyses it was shown that the dominant elements present on four coatings, before their immersion into the SBF solution, are calcium, phosphorous and oxygen, the weight percentage of which is presented in the following table (table 13).

Table 13: Dominant elements detected (mean weight percentages) on the coating of each specimen, before their immersion into the SBF solution.

No. of Specimen	Type of Powder	Ca (%)	P (%)	O (%)
1	XPT-D-703	49,72	13,58	36,70
2	PYRO 4	34,11	15,03	50,87
3	XPT-D-703	37,56	20,08	42,37
4	PYRO 4	56,02	15,04	28,94

The coatings of specimens No. 1 and No. 4 present lower concentrations of oxygen, than those of calcium or phosphorus. On the contrary, specimens No. 2 and 3 are characterized by a more increased oxygen content, which suits better the obtained EDS results, regarding the two types of powder (see paragraph 3.1.1c). No classification based on the type of powder of each specimen can be made. Overall comparison of the values presented in table 13 with those acquired by EDS analyses on the two types of hydroxyapatite powder, shows that phosphorous content fluctuates in the same range of values, while weight percentages of calcium and oxygen slightly vary.

4.4.4) Coating surface related results after immersion into the SBF solution

4.4.4a) Specimen No. 1

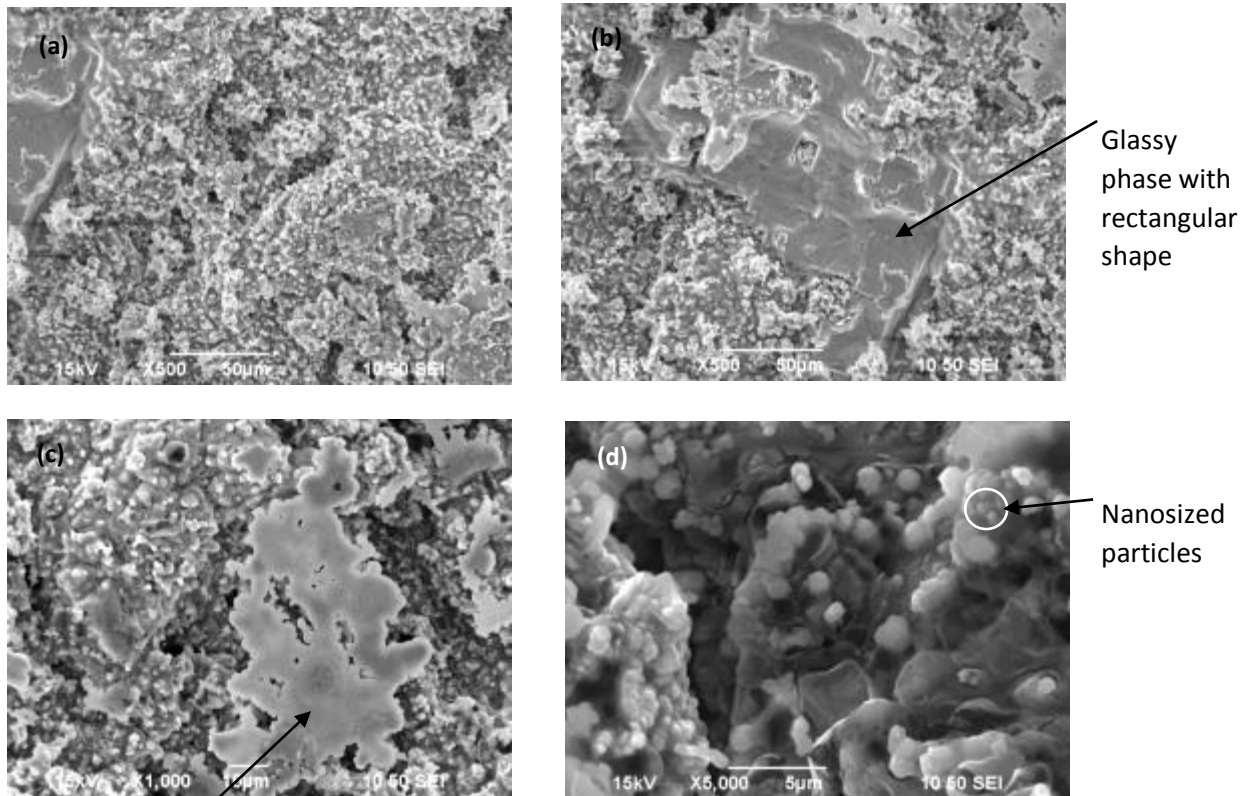


Figure 75: SEM images of the coating surface of specimen No. 1, after immersion into the SBF solution at different magnifications, (a) porous and inhomogeneous coating, (b) glassy surface with rectangular shape, (c) glassy surface with undefined shape, (d) spheroid nanosized HAP particles.

The coating surface presents a porous and inhomogeneous structure (Figs. 75a and 75b). Hydroxyapatite spheroid nanosized particles with diameter of about 2 µm or even less have been formed (Fig. 75d). These particles are dispersed on the coating surface, either solely or they are combined in dense clusters.

Among these clusters large glassy phases are discernible, which have either a more rectangular shape (Fig. 75b) or undefined shape (Fig. 75c). These phases constitute degraded salt crystals or residues from contact of the surface with the SBF solution.

4.4.4b) Specimen No. 2

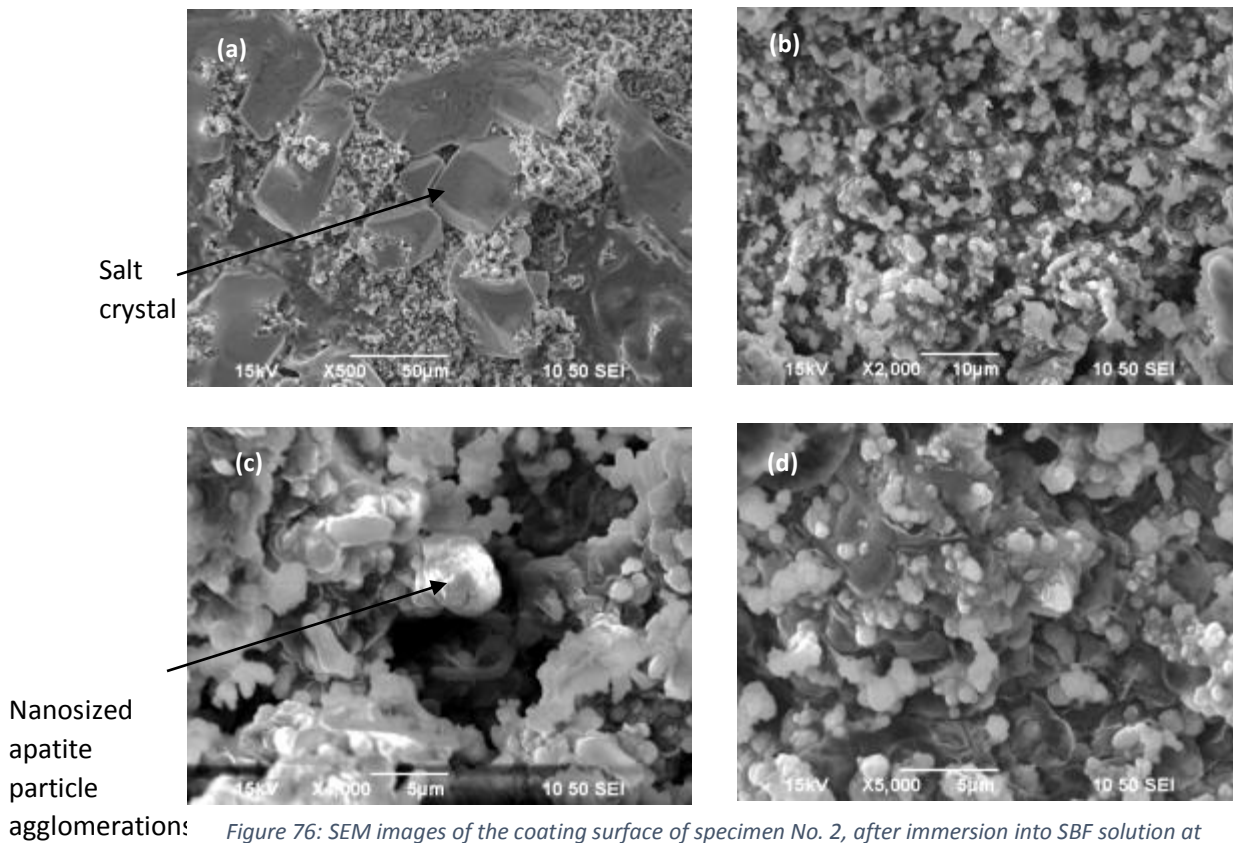


Figure 76: SEM images of the coating surface of specimen No. 2, after immersion into SBF solution at different magnifications, (a) salt crystals, (b) apatite formation, (c) and (d) nanosized apatite particle agglomerations.

Surface microstructure of specimen No. 2 bears great similarity with that of specimen No. 1. The salt crystals observed at the specific sample seem to have a more defined rectangular shape and keep a clearer surface (Fig. 76a). In addition, the newly formed apatite clusters sporadically present a more elongated shape (Fig. 76b). Finally, in figures 76c and 76d, it is shown how some of the nanosized apatite particles have been agglomerated into a larger spheroid particle.

4.4.4c) Specimen No. 3

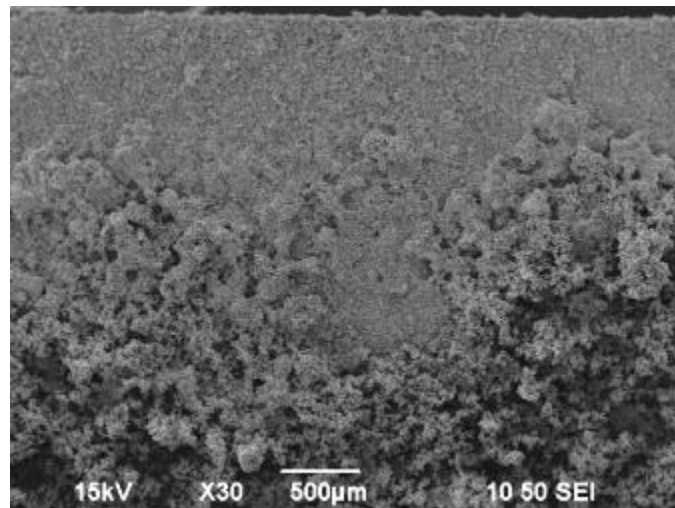


Figure 77: SEM image of the coating surface of specimen No. 3, after immersion into SBF solution at low magnification. Both the area that reacted within the solution (upper) and the undisturbed area (lower) are shown.

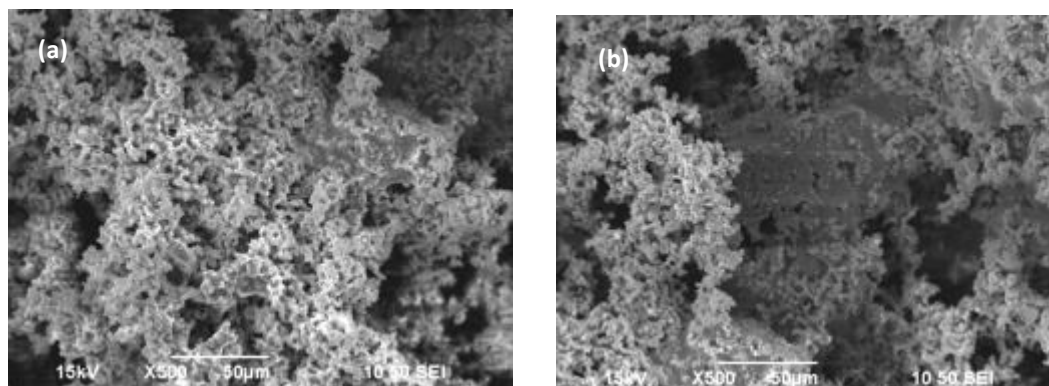


Figure 78: SEM images of the coating surface of specimen No. 3, after immersion into SBF solution. The images refer to the area of the specimen that did not react with the solution. (a) inhomogeneous coating with the form of scaffold, (b) interior of an open pore.

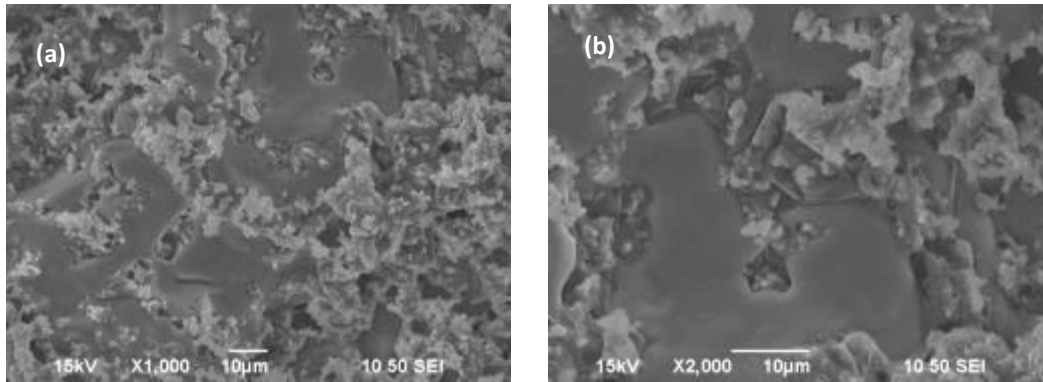


Figure 79: SEM images of the coating surface of specimen No. 3, after immersion into the SBF solution at different magnifications. The images refer to the area of the specimen that reacted with the solution. (a) and (b) salt residues amongst apatite formations.

Specimen No. 3 presented a particular behavior while immersed into the SBF. More specifically, at around the fifth day of its immersion into the solution it started spuming. This could be due to an impurity absorbed by the hydroxyapatite coating, during the cutting process of the specimen. One such impurity that is known to react when found in physiological environment is magnesium (Mg). According to previous study [94], magnesium corrodes rapidly in a simulated body fluid and hydrogen gas bubbles and also hydroxyl anions (OH⁻) are produced as corrosion products. Hydroxyl anions in particular, are prone to induce alkalization of the solution and an increase in its pH value to over 9 in about 10 hours, until a final relatively stable value of 10,5 is reached. As a result, such scenario could disrupt the physiological reaction balances between the SBF and the bioactive specimen and lead to further reaction the between the SBF components and the elements comprising the specimen. The location at which degradation of the hydroxyapatite coating occurred is shown at the upper part of figure 77, alongside the undisturbed area at lower magnification and at figures 79a and 79b, at higher magnifications.

A significantly porous and inhomogeneous coating surface is appeared at figure 78a, which has taken the form of a scaffold. The hydroxyapatite surface is dispersed with newly formed hydroxyapatite nuclei of spherical morphology, each of which has diameter less than 5 µm. These nanosized hydroxyapatite particles have been agglomerated into rod-like structures. In figure 78b, the interior of an open pore of this structure is presented.

The area that interacted with the solution during its immersion into the SBF, is characterized by the same porous and inhomogeneous surface that was described above, although in less magnitude. Amongst the newly formed apatite formations/clusters some glassy deformed phases are observed, which are probably salt residues from the SBF components (Figs. 79a and 79b).

4.4.4d) Specimen No. 4

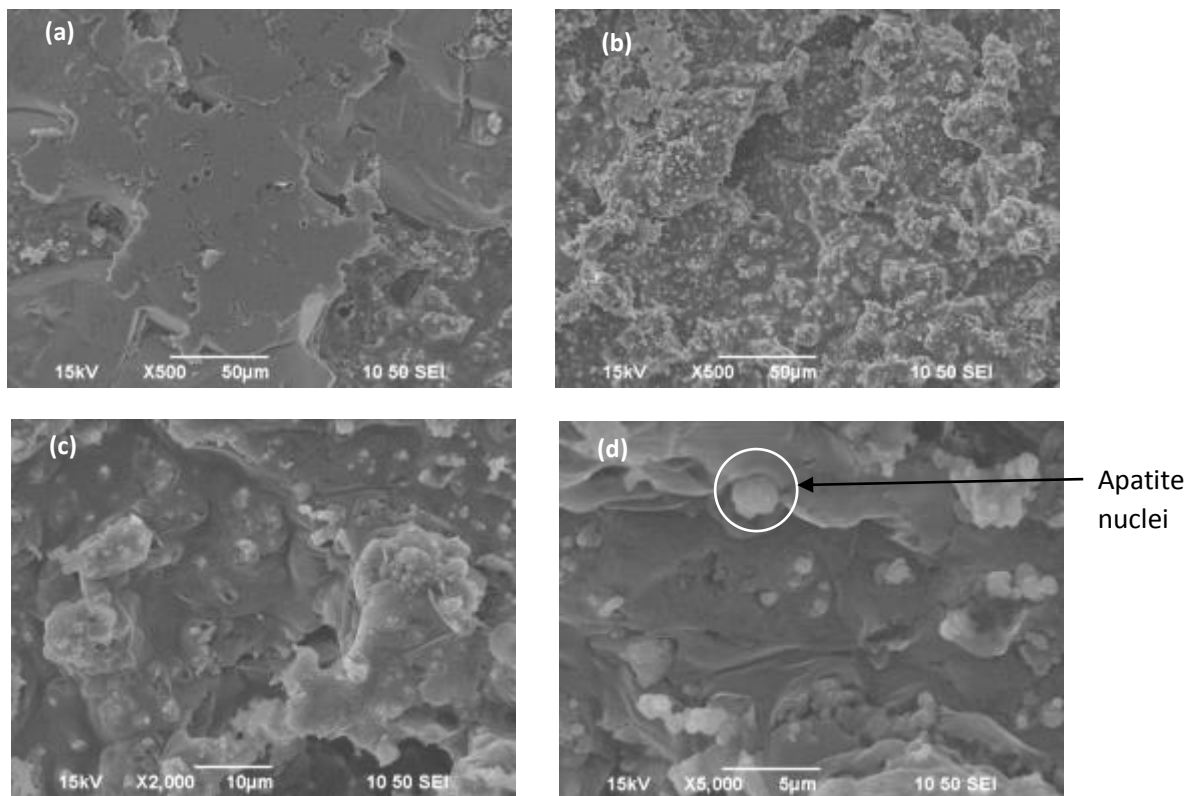


Figure 80: SEM images of the coating surface of specimen No. 4, after immersion into SBF solution at different magnifications.

Specimen No. 4 seems to be the one with the least formation of new apatite phase. Although, there are apatite nanosized nuclei with diameter of less than $2\mu\text{m}$ (Figs. 80c and 80d), they are sparingly dispersed over the coating surface. Salt residues from the SBF solution, shown as glassy phases of undefined shape (Fig. 80a), occupy the most surface. However, apatite particles begin to develop even on that kind of surfaces (Figs. 80c and 80d).

4.4.4e) Energy Dispersive Spectroscopy (EDS)

EDS analyses were performed on the coatings of all the specimens that were retrieved from the SBF solution. Some of the acquired spectra are presented below (Figs. 81 to 83), one for each specimen, respectively. It is noted that, EDS analysis was not performed on specimen No. 3, due to reaction with the surrounding solution.

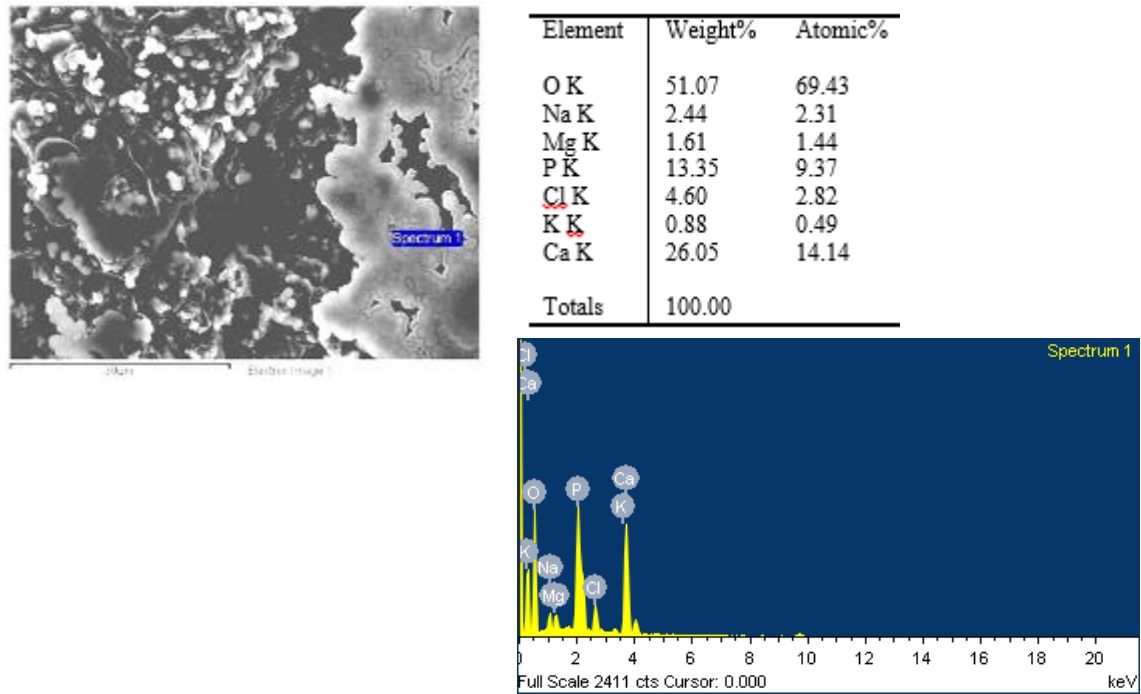


Figure 81: EDS spot analysis on coating specimen No. 1, after immersion into the SBF solution.

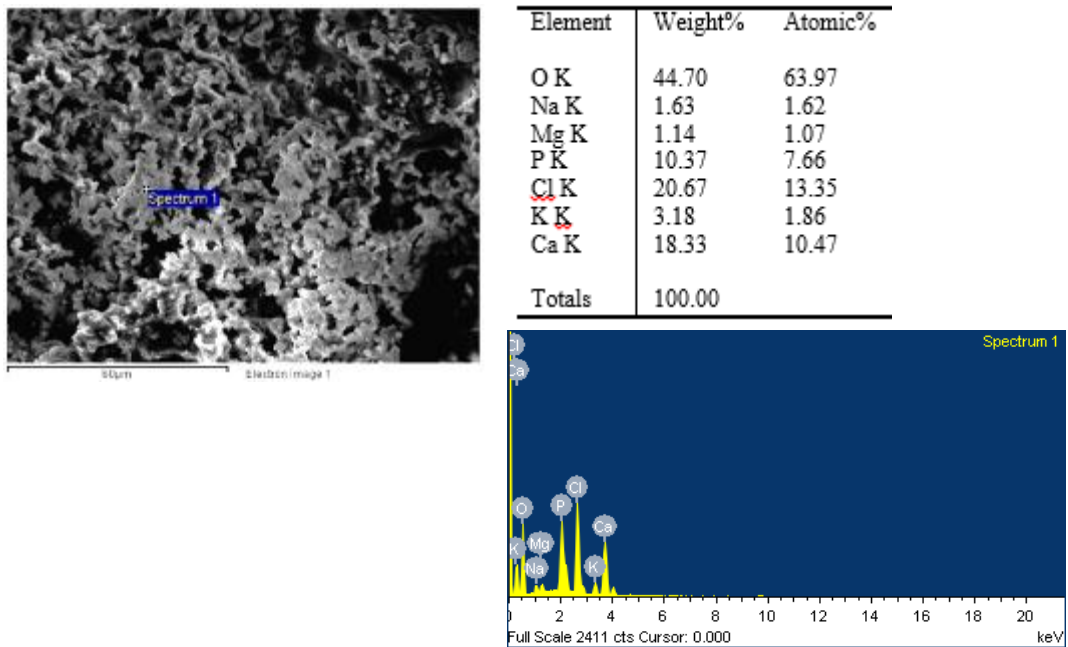


Figure 82: EDS spot analysis on coating of specimen No. 2, after immersion into the SBF solution.

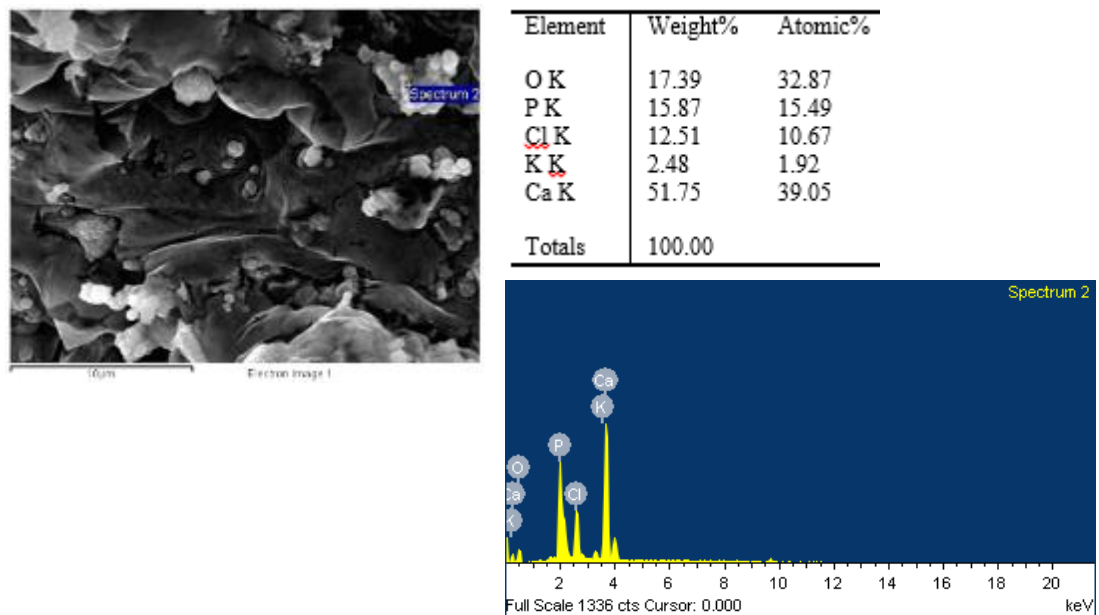


Figure 83: EDS spot analysis on coating of specimen No. 4, after immersion into the SF solution.

From the EDS spot analyses it was shown that the dominant elements present on four coatings, after their immersion into the SBF solution, are calcium, phosphorous and oxygen, the weight percentage of which is presented in the following table (table 14).

Table 14: Dominant elements detected (mean weight percentages) on the coating of each specimen, before their immersion into the SBF solution.

No. of Specimen	Type of Powder	Ca (%)	P (%)	O (%)	Na (%)	Mg (%)	Cl (%)	K (%)
1	XPT-D-703	23,20	13,07	55,56	2,19	1,62	3,39	0,87
2	PYRO 4	22,07	11,71	45,68	3,52	1,43	13,89	1,72
3	XPT-D-703	-	-	-	-	-	-	-
4	PYRO 4	32,49	7,44	30,91	1,56	0,56	23,80	3,24

No conclusions can be withdrawn, based on the type of powder of each specimen, since data regarding the specimen No. 3 were not acquired. Comparison of the values presented above with those obtained from the two types of hydroxyapatite powder (see paragraph 3.1.1c), shows that calcium, phosphorous and oxygen content change in the same direction. More specifically, among these three elements, oxygen is the most abundant, followed by calcium and then phosphorus. In addition, the contents of the specific elements detected on specimens No. 1 and No. 2, fluctuate in the same range of the corresponding values of both the kinds of HAP powder. At the same time, there is a minor deviation in the relative elemental weight percentages of the coating of specimen No. 4 and therefore, a different apatite formation on specimen No. 4 is speculated.

Furthermore, it is noted that Na, Mg, Cl and K elements are present on the examined specimens after immersion, which were not detected on the HAP powders, but are due to contact with the SBF solution. Finally, it is mentioned that when EDS spot analysis was performed on salt crystals (e.g. Fig. 76a in paragraph 4.4.4b), the acquired data revealed presence of Na and Cl alone and thus, were not included in the table (table 14) as reliable results.

4.4.5) Comparison and differences

In order to completely comprehend the changes occurred onto the coating surface of the specimens after immersion into the simulated body fluid solution, two images (Figs. 84a and 84b) are briefly examined. For the sake of comparison, the two figures originate from the same specimen and are of the same magnification.

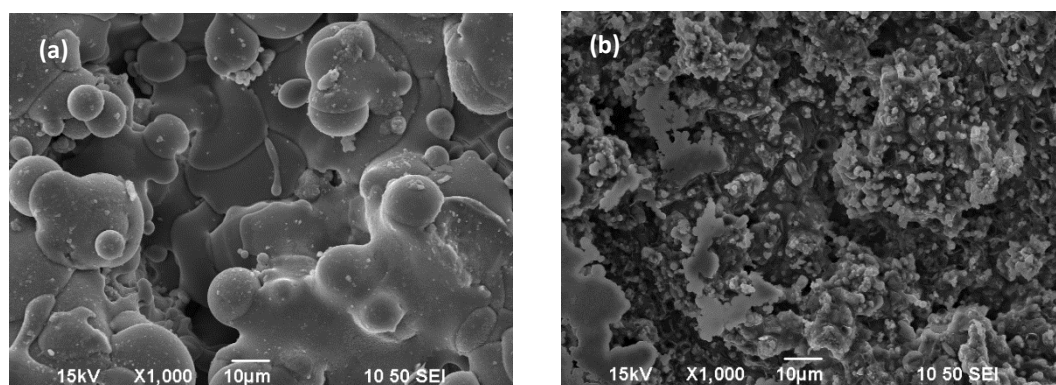


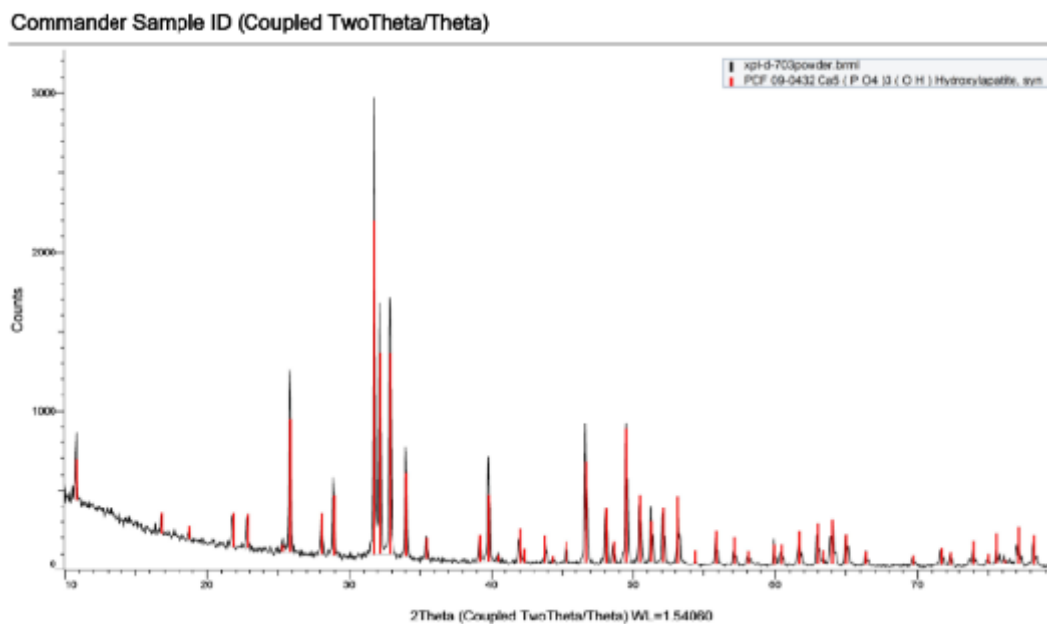
Figure 84: Coating surface of specimen No. 1 (a) before and (b) after immersion into the SBF solution.

As it seen in figure 84a, the coating surface consists of well-flattened rounded splats that are layered one on top of the other. Splat boundaries and pore formations where there is inadequate spreading of the splats are observed. Semi-molten particles with molten shell and unmelted core and also partially melted deformed spheroidal particles are shown. Moreover, unmelted spherical particles from the powder feedstock and particle fractions that are occurred upon impact of the as-sprayed particles with the exact underlying as-sprayed layer of material are noticed. Diameter of such located particles is around 3 μm .

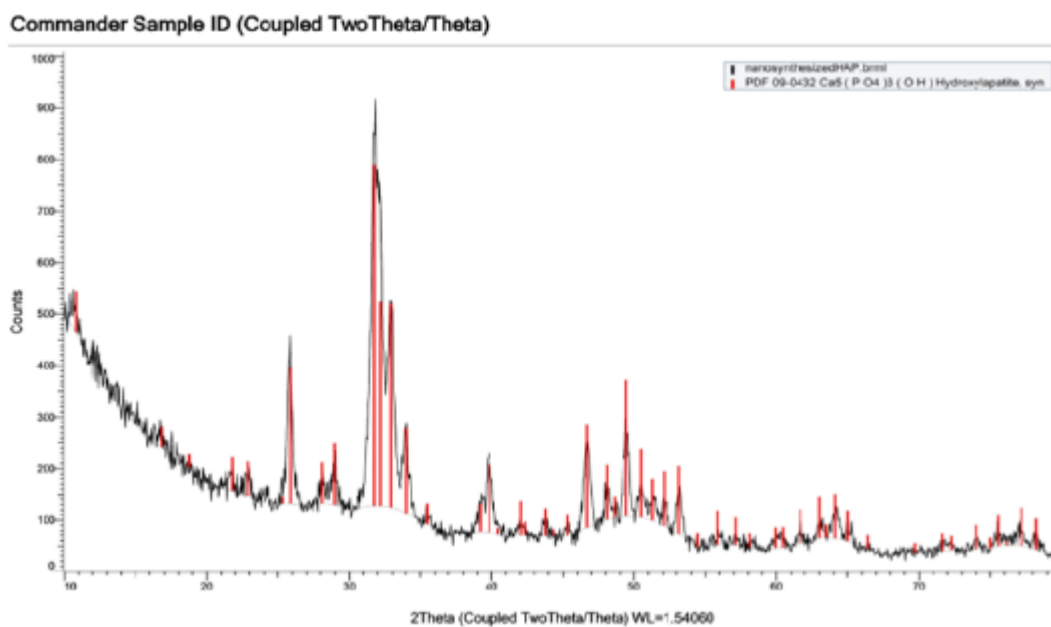
In figure 84b, a rugged and inhomogeneous surface is presented. Phase nucleations are dispersed throughout the coating surface and form growing clusters with tips that seem to project and lengthen. Amongst the new phase undefined glassy surfaces are traced, which contain quantities of elements present in the SBF solution and also act as nucleation sites, as revealed by EDS analysis. Splat formations are indiscernible.

4.5) X-ray Diffraction (XRD)

4.5.1) Powders



(a)



(b)

Figure 85: XRD spectra of (a) commercial XPT-D-703 hydroxyapatite powder and PYRO 4 hydroxyapatite power. In both spectra the diffraction patterns of synthetic hydroxyapatite (red line) is also provided.

After the XRD spectra shown above were acquired (black lines) for each type of hydroxyapatite powder, they were processed by the built-in software of the diffractometer. The existent database of the software confirmed that both the two powders were synthetic hydroxyapatite (red lines). Subsequently, comparison between Figs. 85a and 85b, revealed that XPT-D-703 powder is more crystalline (3000 counts) than PYRO 4 powder, as the intensity of the latter is decreased (940 counts).

The mean crystal size of the commercial HAP powder was calculated by the XRD software, based on the spectra shown in Fig. 81a and was found to be 642,8 Å. However, mean crystal size of PYRO 4 powder was not acquired due to inability of calculation of the Full Width at Half Maximum (FWHM) parameter of the highest peak (Fig. 85b).

Finally, the main (hkl) indices for synthetic HAP that exist in the software database and were a matching reference for both types of powders were (112), (211), (300), (222), (202), (102), (002), (111), (100), (004) listed in descending order of intensity.

4.5.2) Specimens No. 1 and 2

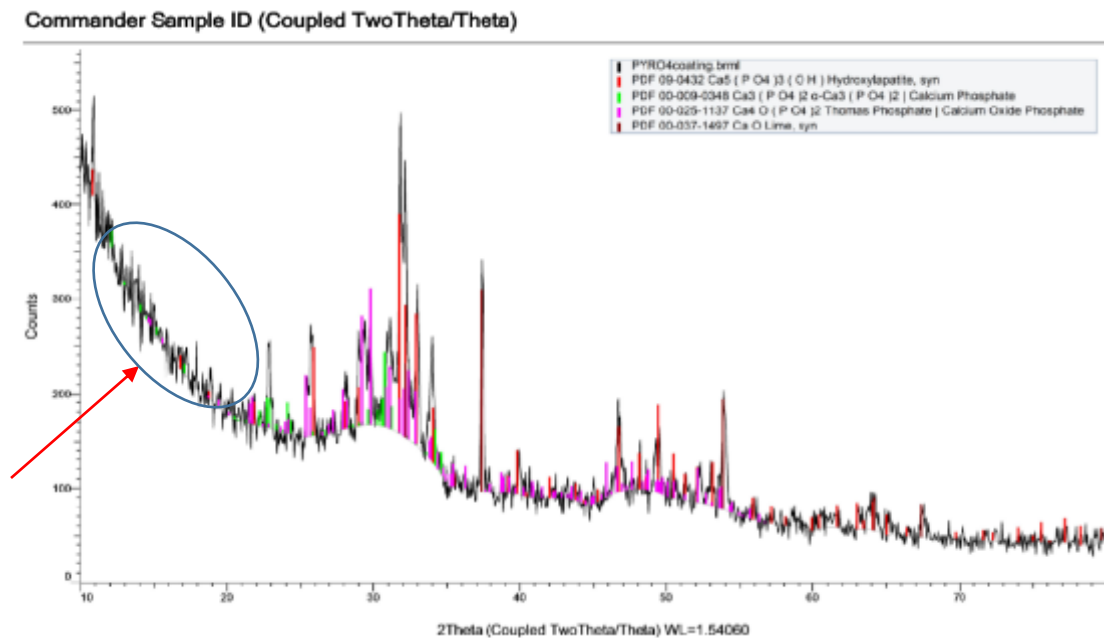
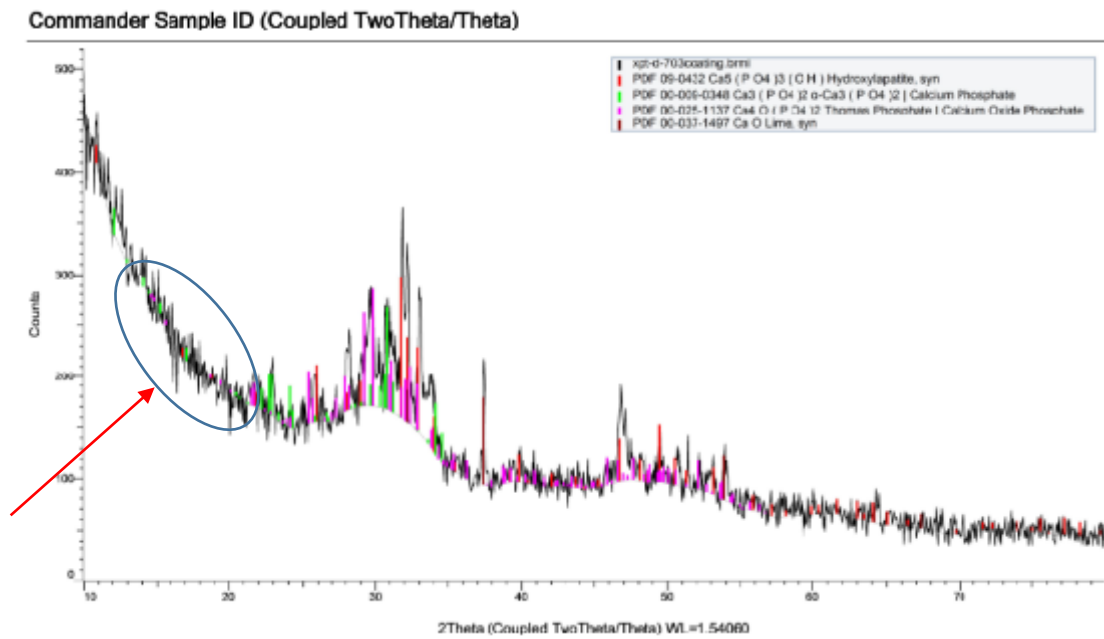
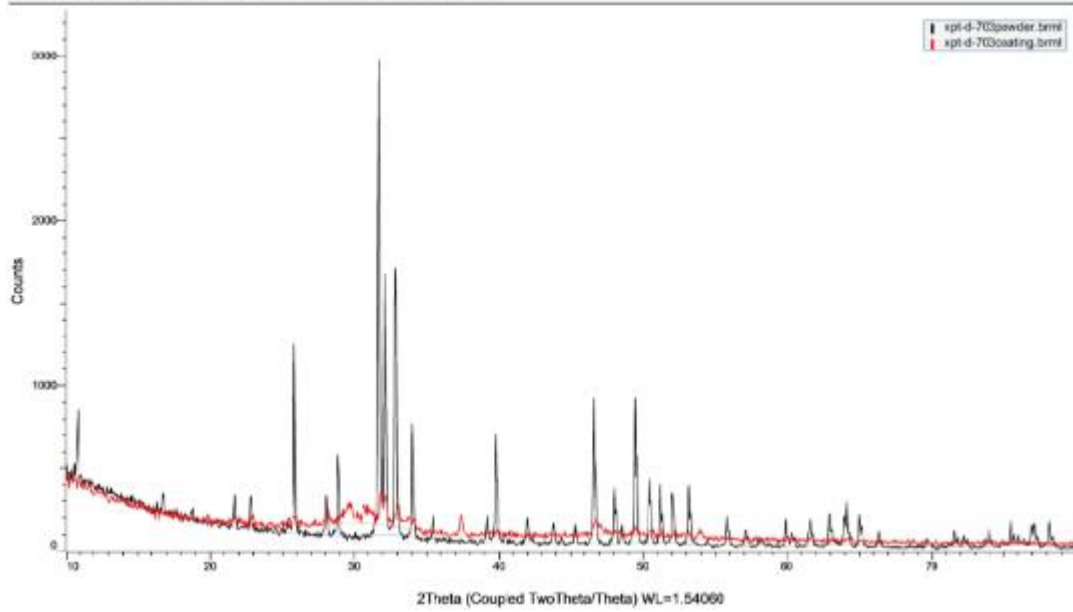


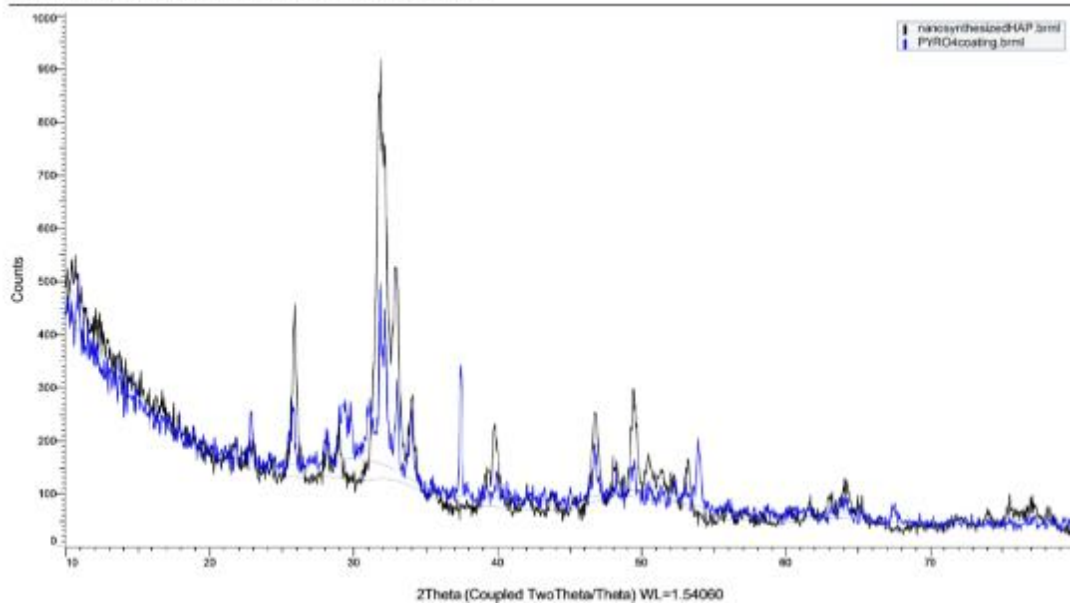
Figure 86: XRD spectra of (a) commercial XPT-D-703 hydroxyapatite coating and (b) PYRO 4 hydroxyapatite coating (black lines). All of the phases identified are also depicted (synthetic HAP= red, calcium phosphate- α = green, tetracalcium phosphate= purple, calcium oxide= brown).

Commander Sample ID (Coupled TwoTheta/Theta)



(a)

Commander Sample ID (Coupled TwoTheta/Theta)



(b)

Figure 87: Aggregated graph of hydroxyapatite powder and its respective hydroxyapatite coating for (a) commercial XPT-D-703 powder and (b) PYRO 4 powder.

Regarding the XRD analysis of the two coatings, both their spectra are characterized by sharp and uneven peaks (they are partially shown by the arrows). The hydroxyapatite powder, during plasma spraying is sprayed in a certain direction (angle) and therefore, occupies a specific orientation upon the substrate. In this way, the scattered intensity of the X-ray beam is more contained, while this is not an issue with powder particles.

In addition, both the two types of powders have lost their crystallinity during thermal spraying and amorphous phases have been developed on the coating. This is evident by the low intensity of the diffracted X-rays on the above spectra, where the highest peak hardly surpasses 500 counts (Figs. 86a and 86b), in contrast with the highest peaks formed on the powder graphs (Figs. 85a and 85b, relatively). This can also be seen more clearly, in the aggregated graphs in Figs. 87a and 87b, where the black spectra are referred to the HAP powders and the red and blue spectra to their respective coatings. Loss of crystallinity can be explained, as hydroxyl groups are removed from the crystalline HAP during plasma spraying, hence the amount of amorphous calcium phosphate is enhanced [95].

Finally, in both X-ray spectra (Figs. 86a and 86b), other calcium phosphate compounds were identified, apart from synthetic HAP (red). Among them, the most dominant phase was calcium oxide (CaO, brown), while α -tricalcium phosphate (α -Ca₃(PO₄)₂ or α -TCP, green) and tetracalcium phosphate (Ca₄(PO₄)₂O or TTCP, purple) followed in smaller quantities. Such phase changes of HAP to other calcium phosphate compounds, are also occurred during plasma spraying [18], [95].

4.5.3) Specimens No. 3 and 4

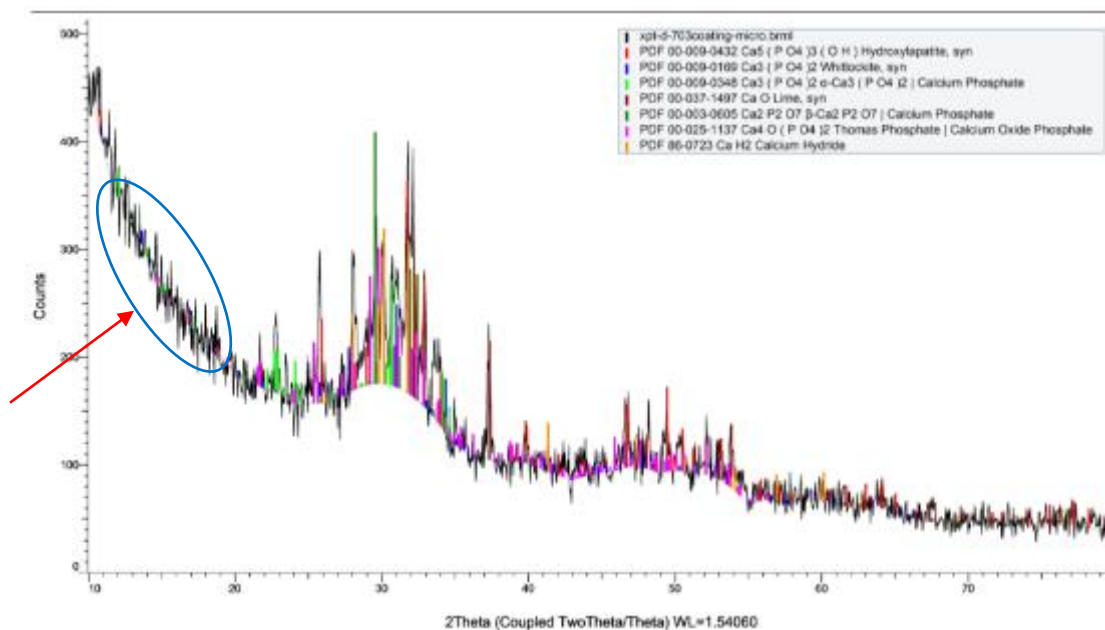


Figure 88: XRD spectra of commercial XPT-D-703 hydroxyapatite coating (black lines). All of the phases identified are also depicted (synthetic HAP= red, whitlockite= blue, calcium phosphate- α =light green, calcium oxide= brown, calcium phosphate- β = green, tetracalcium phosphate= purple, calcium hydride= orange).

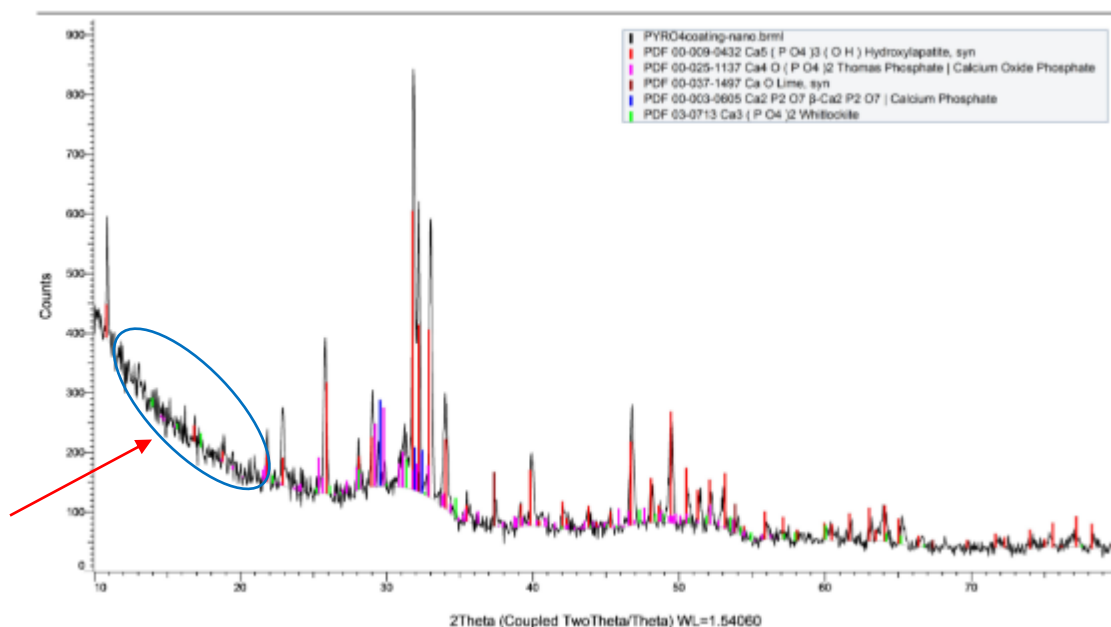


Figure 89: XRD spectra of PYRO 4 hydroxyapatite coating (black lines). All of the phases identified are also depicted (synthetic HAP= red, tetracalcium phosphate= purple, calcium oxide= brown, calcium phosphate- β = blue, whitlockite= green).

Regarding the XRD analysis of the two coatings, both their spectra are once again characterized by sharp and uneven peaks (pointed by the arrows), due to spraying direction of the hydroxyapatite powder.

Moreover, both the two types of powders have partially lost their crystallinity during thermal spraying and amorphous phases have been developed on the coating. Nevertheless, the sample sprayed with PYRO 4 hydroxyapatite powder remains fairly crystalline, as the highest peak of intensity of the diffracted X-rays on the relative spectra almost reaches 900 counts, which is really close to the approximately 940 counts of the powder (Figs. 89 and 85b). On the contrary, the intensity of the diffracted X-rays regarding the sample sprayed with XPT-D-703 hydroxyapatite powder hardly surpasses 500 counts and is much further than the 3000 counts referred to the relative powder before spraying (Figs. 88 and 85a).

Finally, in both X-ray spectra (Figs. 88 and 89), other calcium phosphate compounds were identified, apart from synthetic HAP (red). Among them, phases that were identified in both spectra were calcium oxide (CaO), β -tricalcium phosphate (β -Ca₃(PO₄)₂ or β -TCP), tetracalcium phosphate (Ca₄(PO₄)₂O or TTCP) and calcium phosphate (Ca₂P₂O₇ β -Ca₂P₂O₇). Additionally, α -tricalcium phosphate (α -Ca₃(PO₄)₂ or α -TCP) and calcium hydride (CaH₂) were detected in the XPT-D-703 coating. Such phase changes of HAP to other calcium phosphate compounds, are also occurred during plasma spraying [18], [95].

4.6) Microhardness

Table 15: Microhardness measurements.

No. of Sample	Type of Powder	Microhardness (GPa)
1	XPT-D-703	$2,27 \pm 0,82$
2	PYRO 4	$2,73 \pm 0,66$
3	XPT-D-703	$2,64 \pm 0,56$
4	PYRO 4	$2,27 \pm 0,42$

From the above table, it is concluded that all four specimens practically have the same microhardness. The measured value falls within the expected range mentioned in the literature [42], [96].

4.7) Porosity

4.7.1) Porosimetry via image analysis

Porosity analysis was performed on images acquired by the optical microscope (Leica DMILM) with either (x100) or (x200) magnification. Three images were taken on random spots along the hydroxyapatite layer, for each specimen accordingly. For the porosity analysis MIPAR image analysis software was used. The resulting data are presented in the following tables (tables 16-20).

4.7.1a) Specimen No. 1

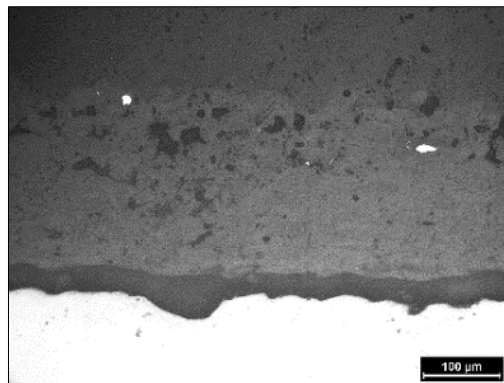


Figure 90: Original photo of sample No. 1 with XPT-D-703 hydroxyapatite powder acquired by the optical microscope.

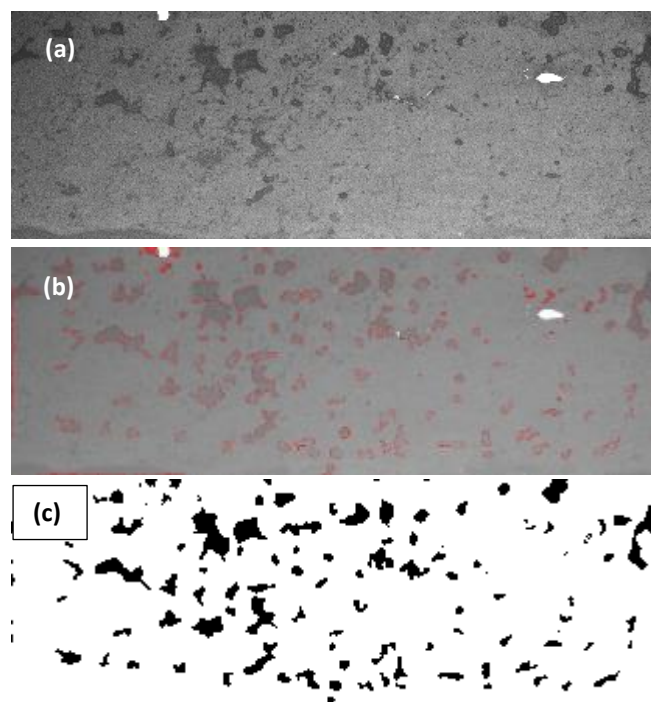


Figure 91: Cropped image of the original photo for ease of processing, (b) with pore outline, (c) on black and white display.

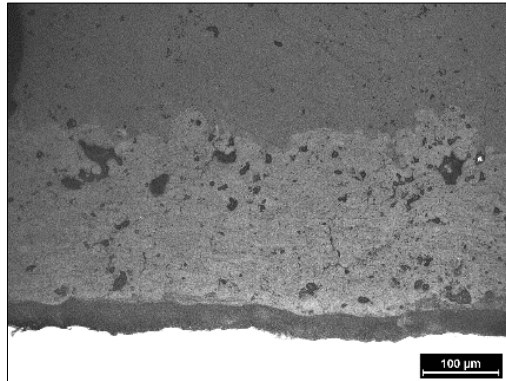


Figure 92: Original photo of sample No. 1 with XPT-D-703 hydroxyapatite powder acquired by the optical microscope.

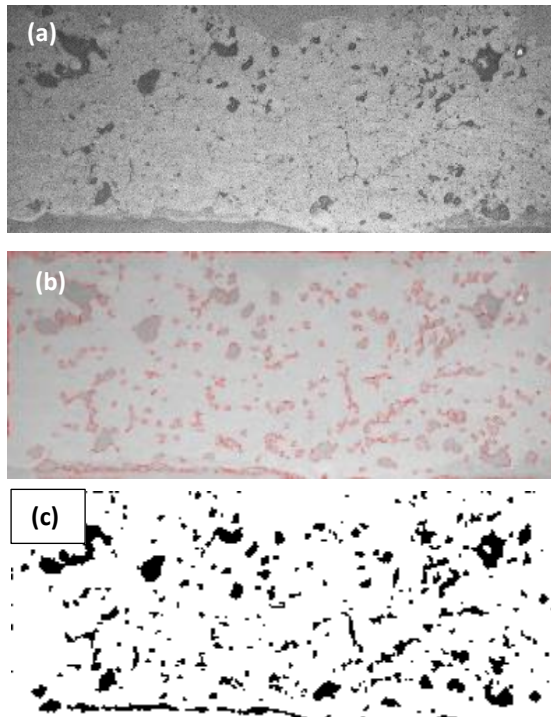


Figure 93: (a) Cropped image of the original photo for ease of processing, (b) with pore outline, (c) on black and white display.

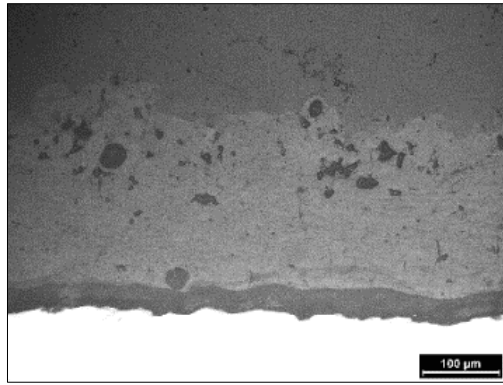


Figure 94: Original photo of sample No. 1 with XPT-D-703 hydroxyapatite powder acquired by the optical microscope.

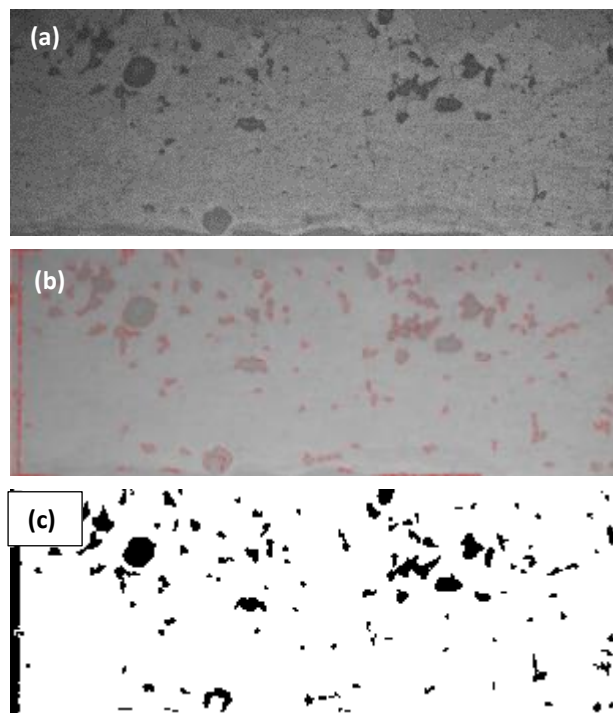


Figure 95: (a) Cropped image of the original photo for ease of processing, (b) with pore outline, (c) on black and white display.

Table 16: Porosity measurements on XPT-D-703 hydroxyapatite coating of sample No. 1.

Snapshots	1	2	3
Features	186	447	175
Area fraction of porosity (%)	9,67	12,57	7,81
Equivalent diameter (μm)	7,74 ± 6,46	6,25 ± 4,32	7,70 ± 5,86
Upper value/ Lower value of equivalent diameter	0,37/ 26,52	0,37/ 34,01	0,37/ 49,62

4.7.1b) Specimen No. 2

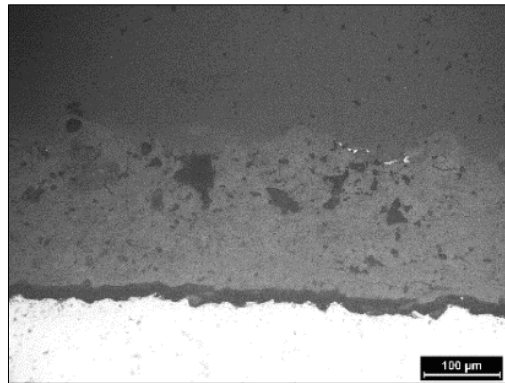


Figure 96: Original photo of sample No. 2 with PYRO 4 hydroxyapatite powder acquired by the optical microscope.

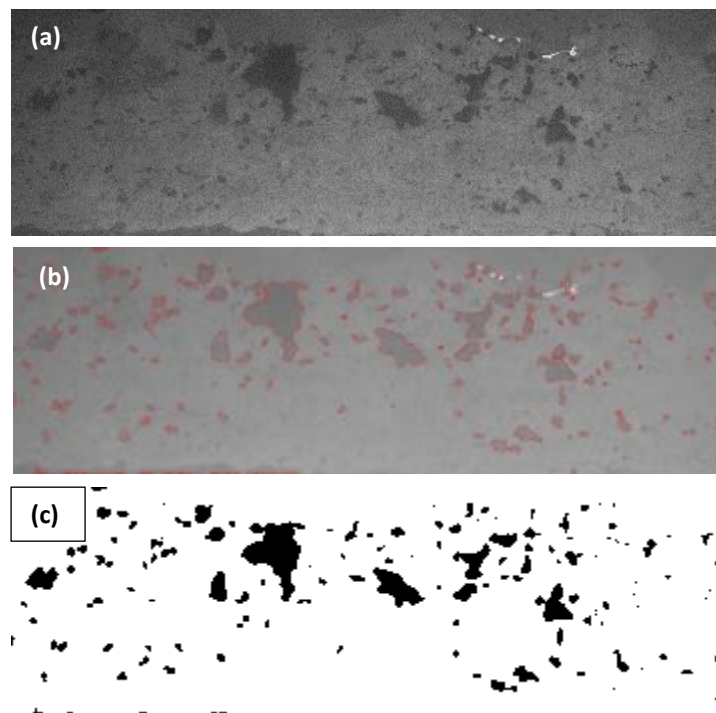


Figure 97: (a) Cropped image of the original photo for ease of processing, (b) with pore outline, (c) on black and white display.

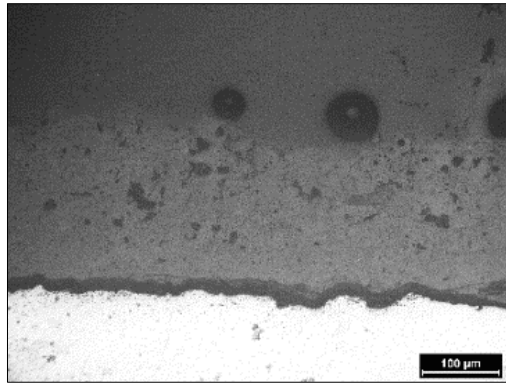


Figure 98: Original photo of sample No. 2 with PYRO 4 hydroxyapatite powder acquired by the optical microscope.

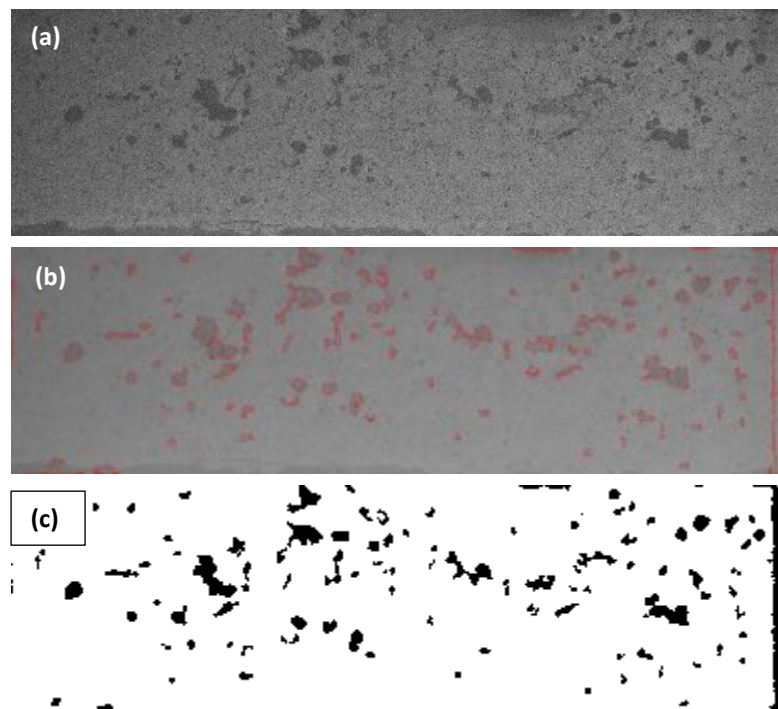


Figure 99: (a) Cropped image of the original photo for ease of processing, (b) with pore outline, (c) on black and white display.

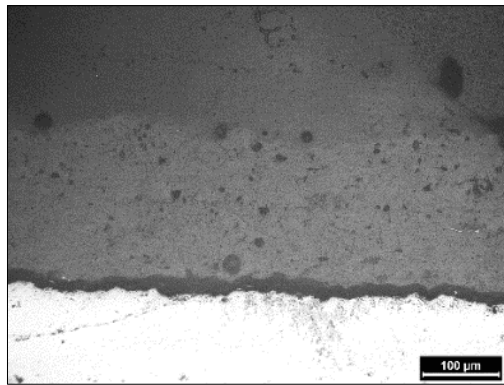


Figure 100: Original photo of sample No. 2 with PYRO 4 hydroxyapatite powder acquired by the optical microscope.

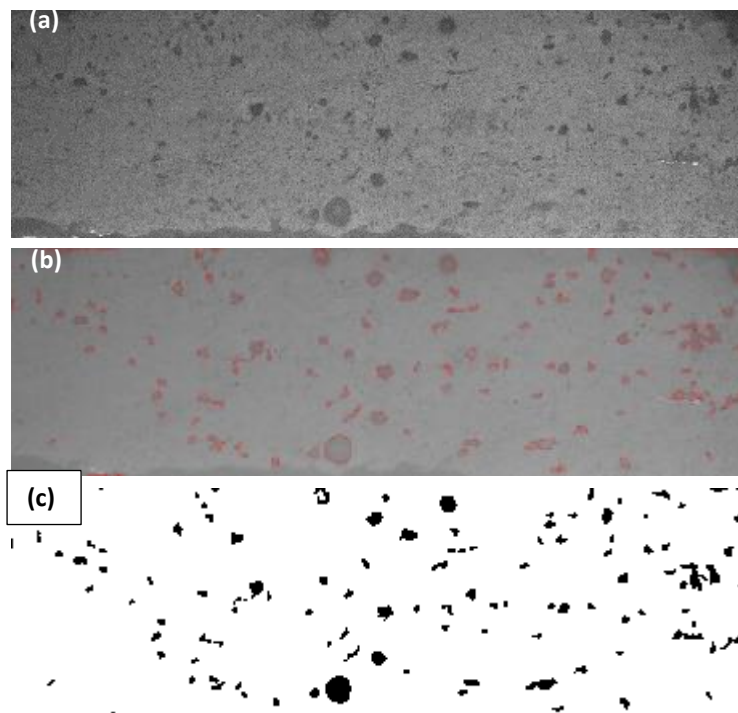


Figure 101: (a) Cropped image of the original photo for ease of processing, (b) with pore outline, (c) on black and white display.

Table 17: Porosity measurements on PYRO 4 hydroxyapatite coating of sample No. 2.

Snapshots	1	2	3
Features	259	148	164
Area fraction of porosity (%)	7,65	7,16	4,46
Equivalent diameter (μm)	4,95 ± 5,42	7,67 ± 4,97	5,86 ± 3,77
Upper value/ Lower value of equivalent diameter	0,37/ 47,99	0,38/ 47,67	0,37/ 24,55

4.7.1c) Specimen No. 3

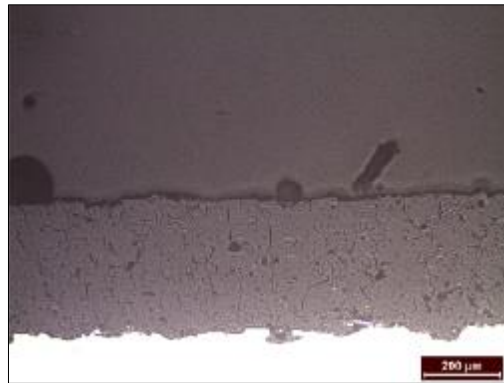


Figure 102: Original photo of sample No. 3 with XPT-D-703 hydroxyapatite powder acquired by the optical microscope.

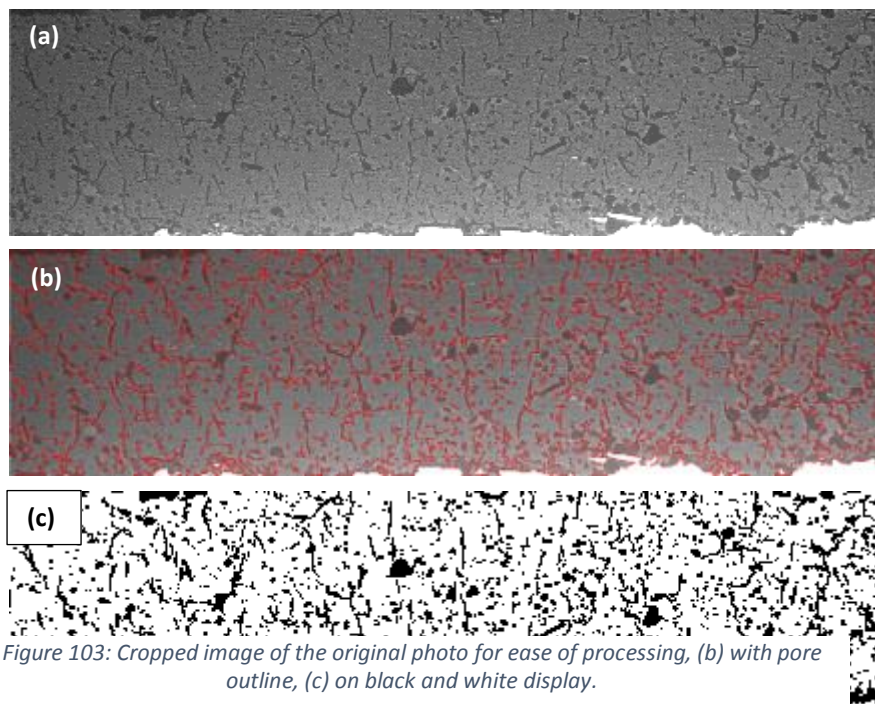


Figure 103: Cropped image of the original photo for ease of processing, (b) with pore outline, (c) on black and white display.

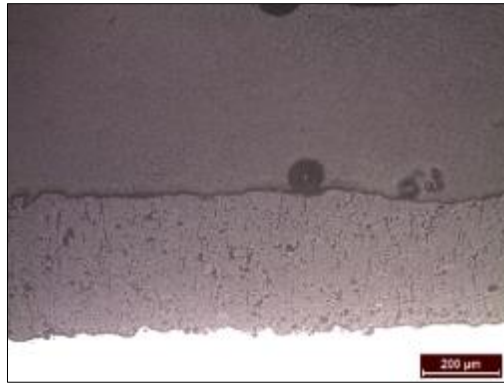


Figure 104: Original photo of sample No. 3 with XPT-D-703 hydroxyapatite powder acquire by the optical microscope.

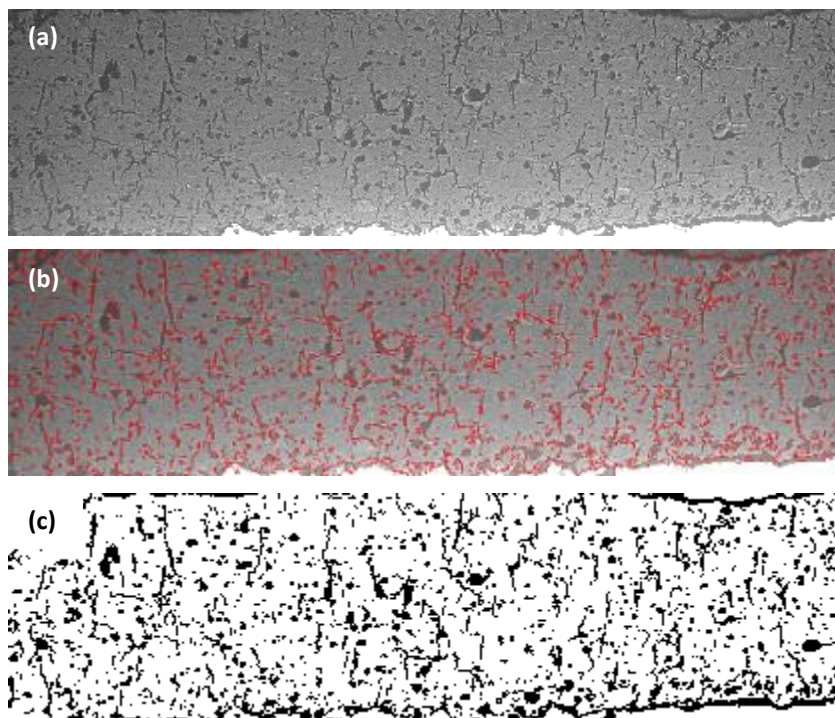


Figure 105: (a) Cropped image of the original photo for ease of processing, (b) with pore outline, (c) on black and white display.

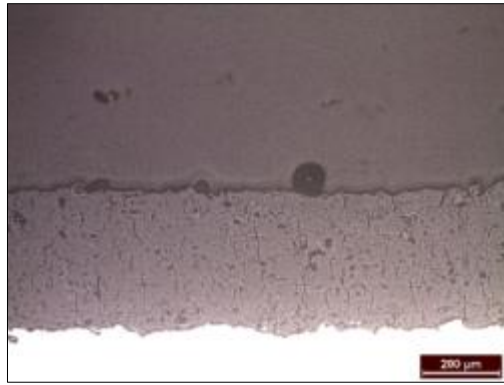


Figure 106: Original photo of sample No. 3 with XPT-D-703 hydroxyapatite powder acquired by the optical microscope.

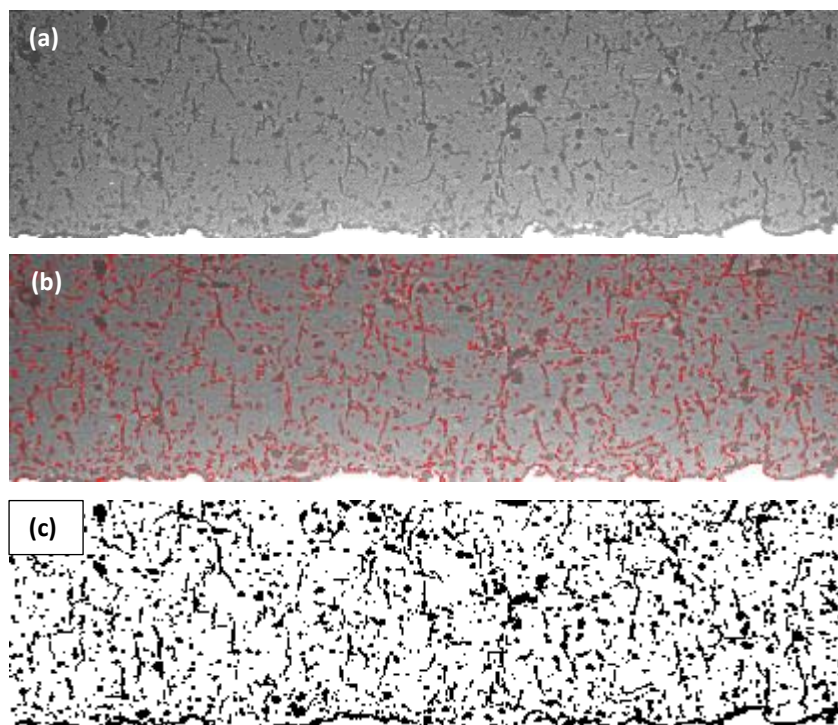


Figure 107: (a) Cropped image of the original photo for ease of processing, (b) with pore outline, (c) on black and white display.

Table 18: Porosity measurements on XPT-D-703 hydroxyapatite coating of sample No. 3.

Snapshots	1	2	3
Features	1105	1103	1141
Area fraction of porosity (%)	21,11	19,27	20,47
Equivalent diameter (μm)	8,57 ± 6,35	8,54 ± 6,06	8,95 ± 5,67
Upper value/ Lower value of equivalent diameter	4,12/ 78,21	4,15/ 92,12	4,13/ 66,57

4.7.1d) Specimen No. 4

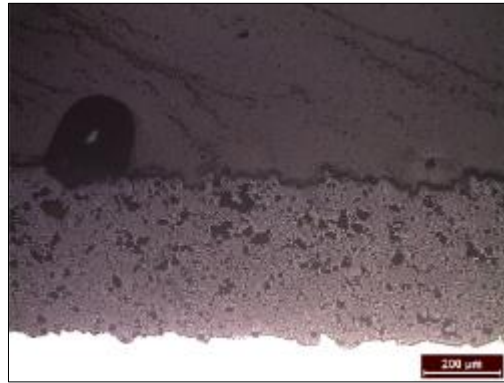


Figure 108: Original photo of sample No. 4 with PYRO 4 hydroxyapatite powder acquired by the optical microscope.

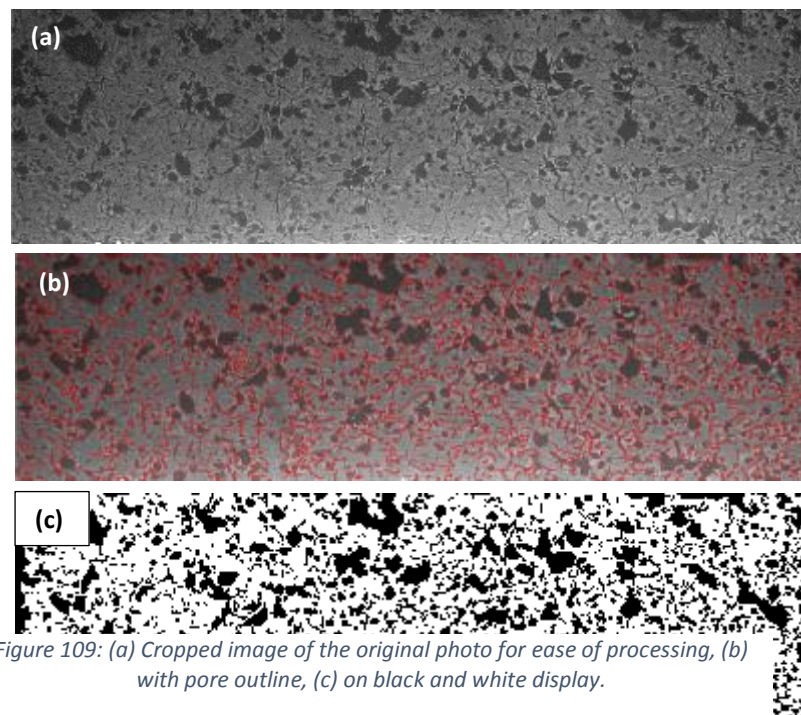


Figure 109: (a) Cropped image of the original photo for ease of processing, (b) with pore outline, (c) on black and white display.

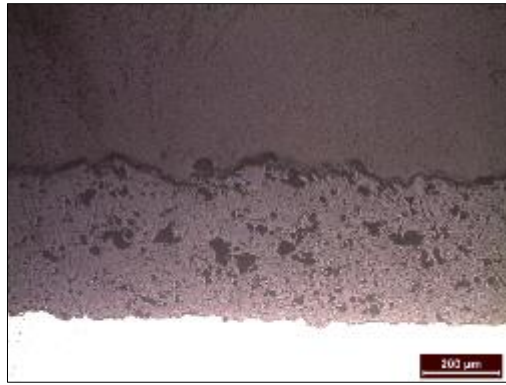


Figure 110: Original photo of sample No. 4 with PYRO 4 hydroxyapatite powder acquired by the optical microscope.

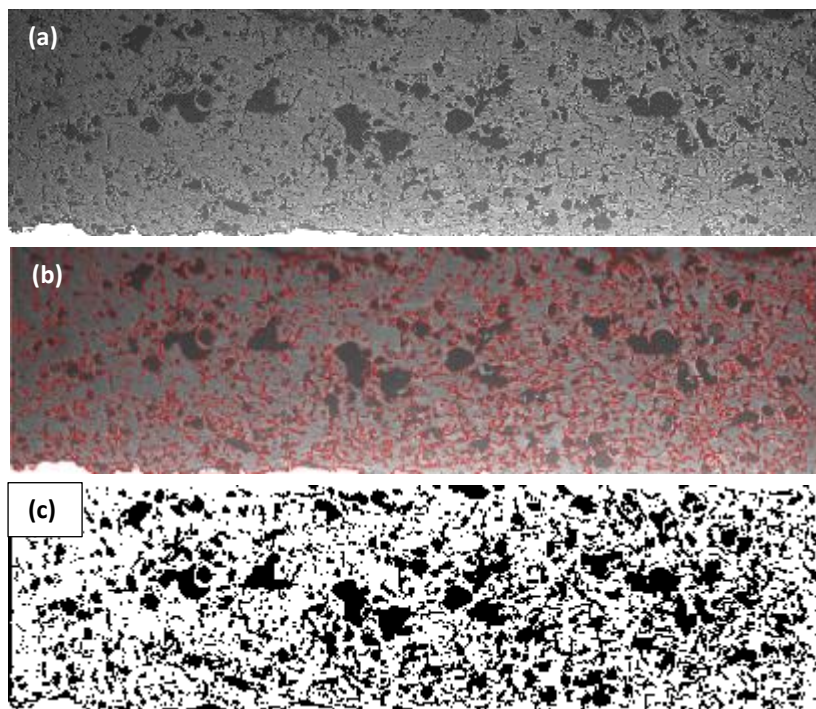


Figure 111: (a) Cropped image of the original photo for ease of processing, (b) with pore outline, (c) on black and white display.

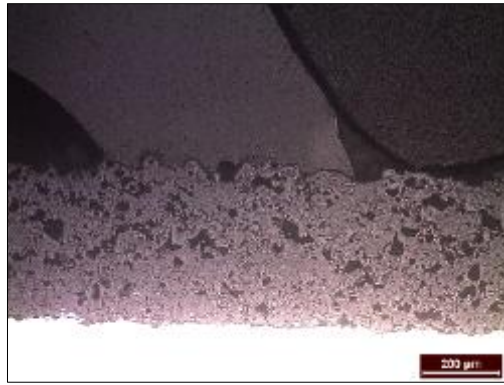


Figure 112: Original photo of sample No. 4 with PYRO 4 hydroxyapatite powder acquired by the optical microscope.

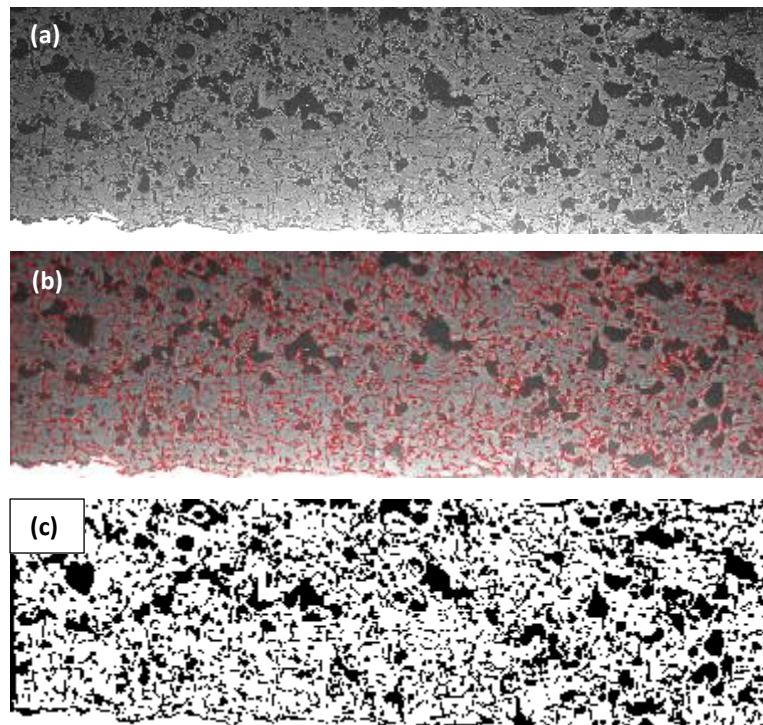


Figure 113: (a) Cropped image of the original photo for ease of processing, (b) with pore outline, (c) on black and white display.

Table 19: Porosity measurements on PYRO 4 hydroxyapatite coating of sample No. 4.

Snapshots	1	2	3
Features	954	1576	832
Area fraction of porosity (%)	34,06	35,71	34,52
Equivalent diameter (μm)	12,17 ± 9,38	8,63 ± 8,39	11,28 ± 12,48
Upper value/ Lower value of equivalent diameter	5,32/ 108,51	1,48/ 97,15	0,74/ 133,32

As it is extracted from the data referred to the samples No. 1 and 2 (tables 16 and 17), the area fraction (porosity percentage) of the sample with the commercial hydroxyapatite powder is somewhat larger than that of the nanosized hydroxyapatite powder, while the exact opposite occurs, regarding the samples No. 3 and 4. The average porosity percentages for the specimens No. 1 and 2 are 10 % for the sample covered with XPT-D-703 powder and 6,4 % for the one covered with PYRO 4 powder. The respective percentages for the samples No. 3 and 4 are 20,3 % and 34,8 %. For both types of hydroxyapatite powder the porosity percentage of the specimens No. 3 and 4 is broadly increased. This is explained if the altered spraying conditions, specifically lower spray power, are taken into consideration. As it has already been mentioned, lower spray power, results in inadequate melting of the as sprayed particles and formation of pores throughout the coating material. Thereby, porosity rises. The equivalent diameter of pores in μm , also appears elevated for the specific samples, which is expected as a fraction of the depicted pores merge and thereby, are sized as one. The total porosity percentage of the samples and the average pore diameter calculated via image analysis is presented below (table 20).

Table 20: Porosity percentage and average pore diameter (in μm) of all four specimens, acquired by image analysis.

No. of Sample	Type of Powder	Porosity (%)	Average pore diameter (μm)
1	XPT-D-703	10	7,2
2	PYRO 4	6,4	6,2
3	XPT-D-703	20,3	8,7
4	PYRO 4	34,8	10,7

4.7.2) Mercury (Hg) porosimetry

Porosity of the specimens was further examined via mercury (Hg) porosimetry method. The equipment used was a ThermoFinnigan Pascal 440 porosimeter, where the specimens were inserted after having been heated in the furnace at 60 °C for 24 hours and freeze dried for another 24 hours. The acquired diagrams of pore size distribution are presented below, one for each type of hydroxyapatite coating.

4.7.2a) Specimen No. 1

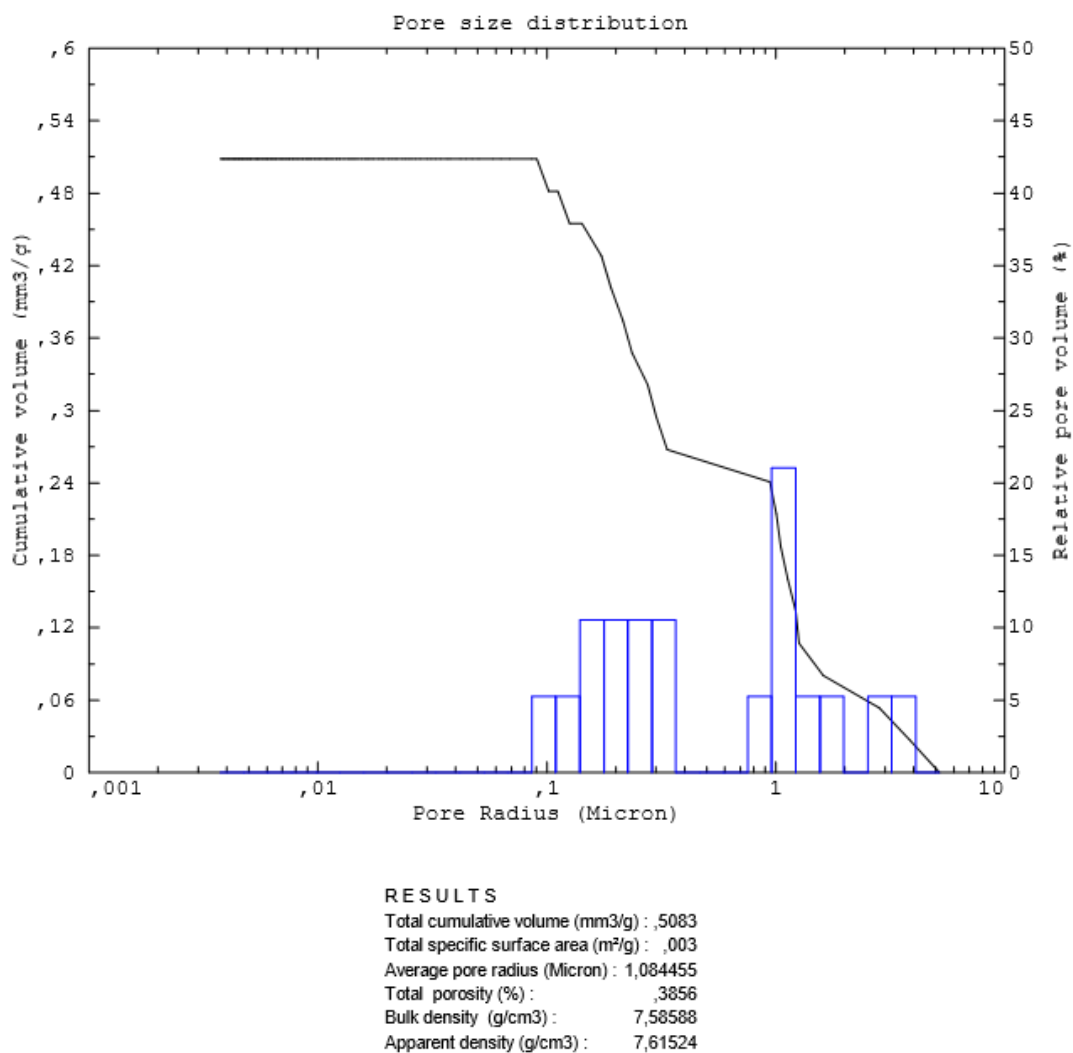
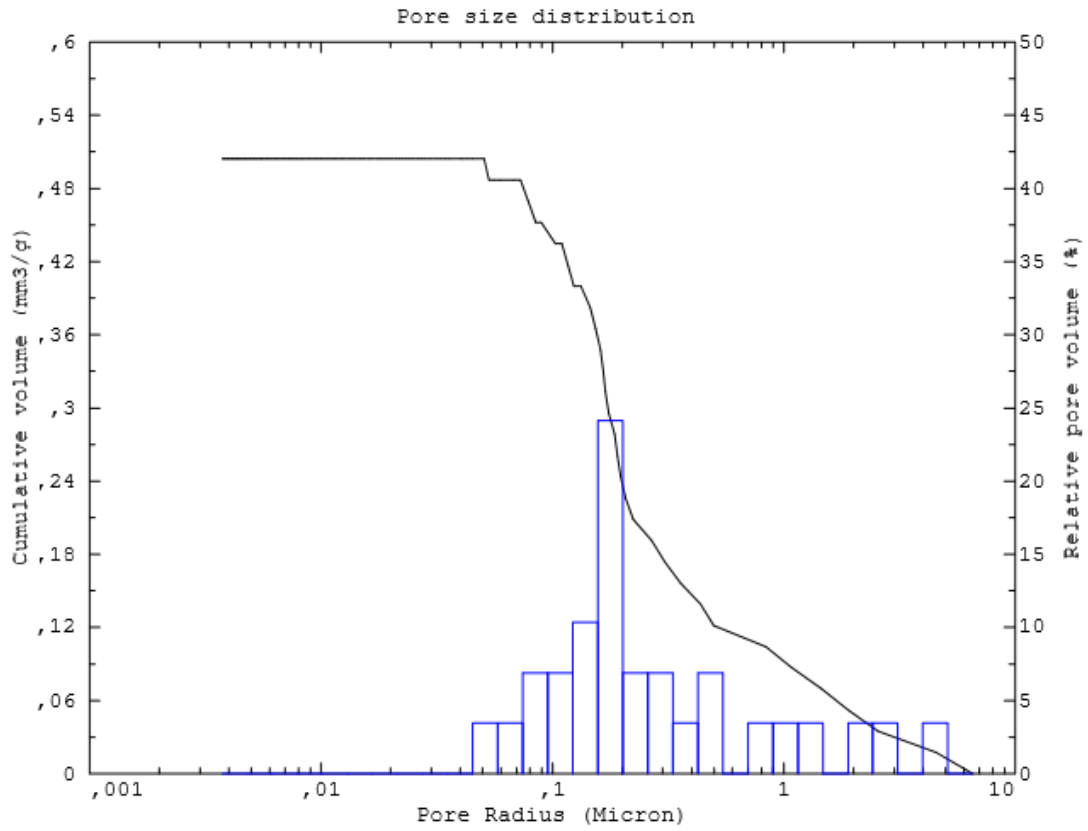


Figure 114: Pore size distribution in commercial XPT-D-703 hydroxyapatite coating.

4.7.2b) Specimen No. 2

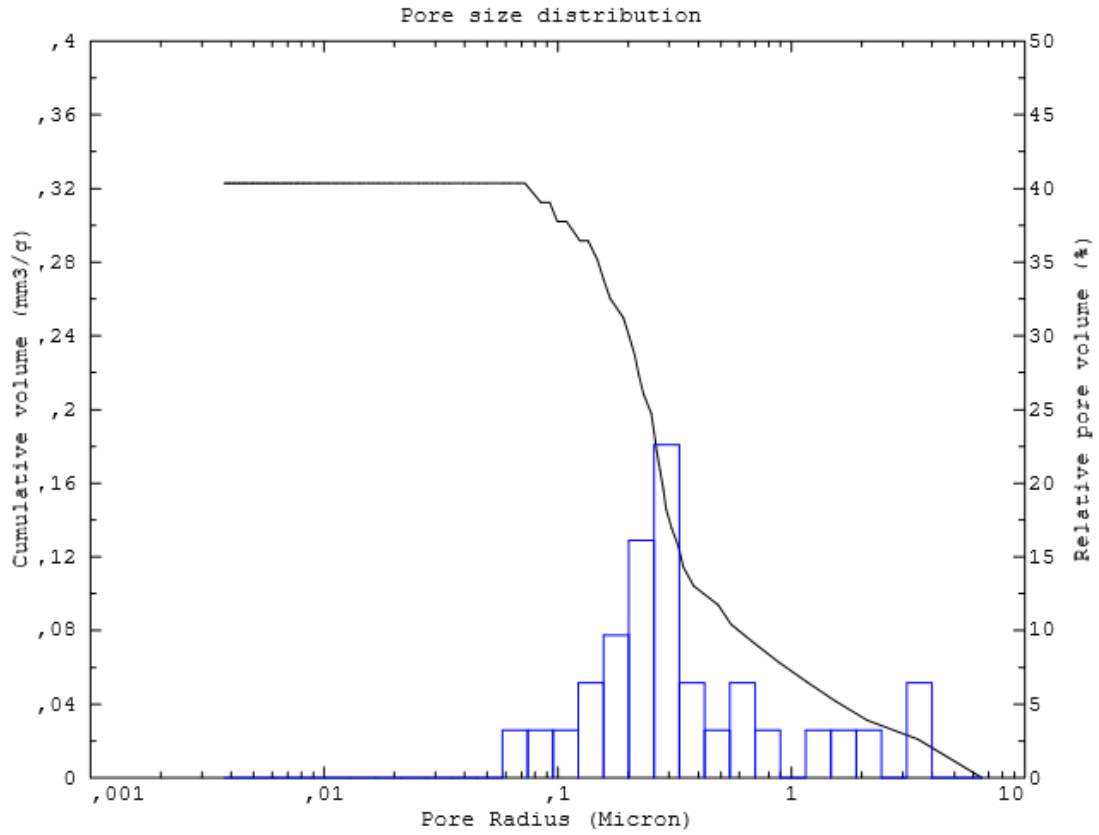


RESULTS

Total cumulative volume (mm3/g) : ,5042
 Total specific surface area (m²/g) : ,006
 Average pore radius (Micron) : ,17754
 Total porosity (%) : ,3824
 Bulk density (g/cm3) : 7,58381
 Apparent density (g/cm3) : 7,61292

Figure 115: Pore size distribution in PYRO 4 hydroxyapatite coating.

4.7.2c) Specimen No. 3



RESULTS
Total cumulative volume (mm³/g) : ,3229
Total specific surface area (m²/g) : ,003
Average pore radius (Micron) : ,29229
Total porosity (%) : ,2447
Bulk density (g/cm³) : 7,57638
Apparent density (g/cm³) : 7,59496

Figure 116: Pore size distribution in commercial XPT-D-703 hydroxyapatite coating.

4.7.2d) Specimen No. 4

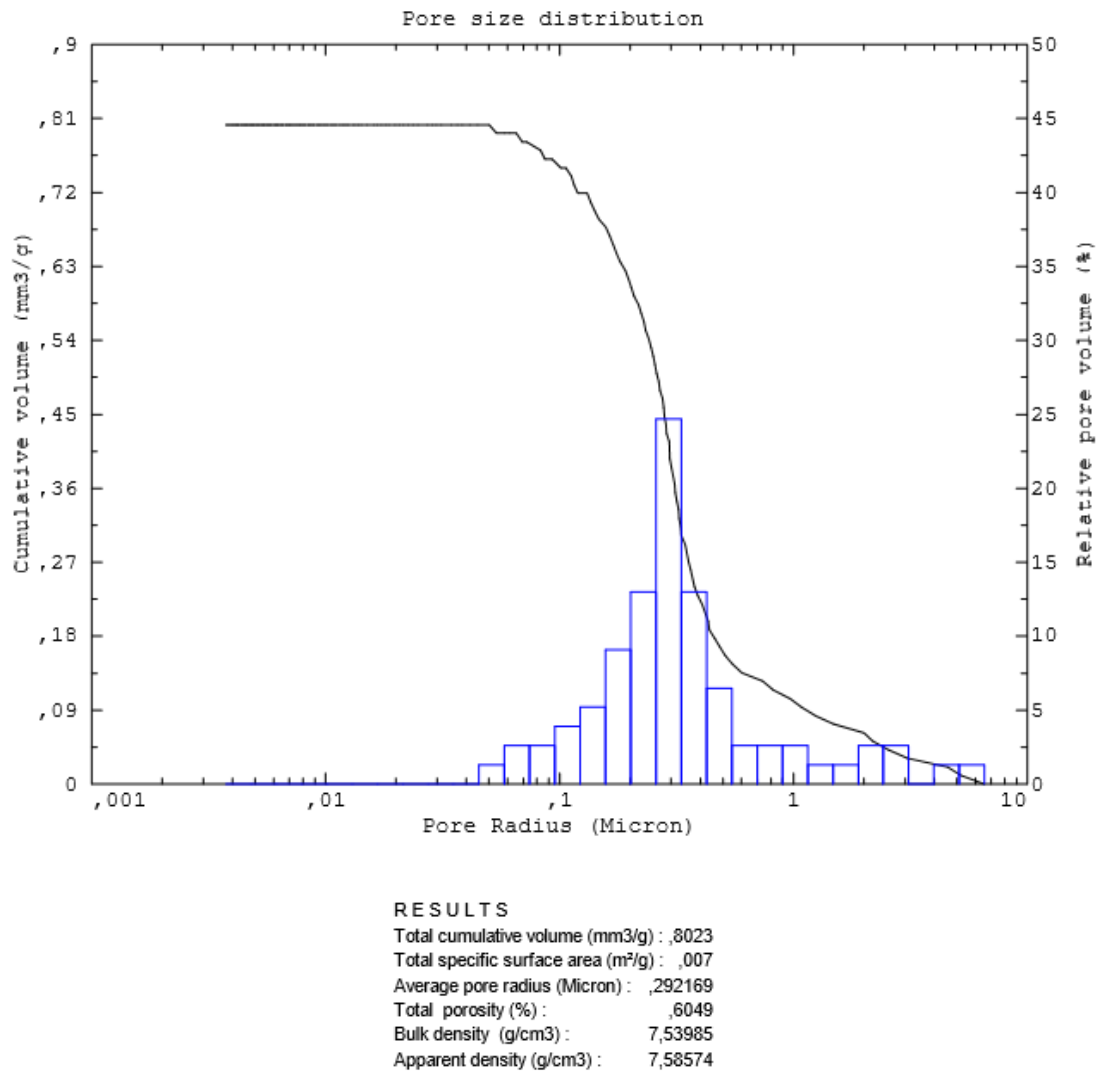


Figure 117: Pore size distribution in PYRO 4 hydroxyapatite coating.

Average pore radius and also total porosity percentage were calculated by the porosimeter software. Regarding the samples No. 1 and 2, for the commercial hydroxyapatite coating, the estimated values were 1,084 μm and 0,3856 % respectively, while for the PYRO 4 coating the corresponding estimated values were 0,178 μm and 0,3824 %. Regarding the samples No. 3 and 4, for the commercial hydroxyapatite coating, the estimated values were 0,2923 μm and 0,2447 % respectively, while for the PYRO 4 coating the corresponding estimated values were 0,2922 μm and 0,6049 %.

Based on the recently acquired data, sample No. 4, namely the one sprayed with PYRO 4 hydroxyapatite powder, displays the greatest improvement. This is

because both the average pore radius and the total porosity percentage have been increased in comparison with the relative sample No. 3. In addition, after observation of the diagrams in Figs. 114-117, pore size distribution of the specific sample seems to be the most uniform of all.

Concerning the vast difference in the results given by the two porosimetry methods, one can not exclude the other, as they both provide information about the coating. Nevertheless, the crucial information that mercury porosimetry provides, is that the total of porosity that was observed via the optical microscope and then estimated with image analysis, comprises in fact from closed pores that are not interconnected all the way through to the coating surface. The total porosity percentage of the samples and the average pore radius measured via mercury porosimetry is presented below (table 21).

Table 21: Porosity percentage and average pore radius (in μm) of all four specimens, measured by mercury porosimetry.

No. of Sample	Type of Powder	Total Porosity (%)	Average pore radius (μm)
1	XPT-D-703	0,4	1,1
2	PYRO 4	0,4	0,2
3	XPT-D-703	0,2	0,3
4	PYRO 4	0,6	0,3

4.8) Adhesion strength test

Table 22: Adhesion strength test results (in MPa) of commercial and nanostructured hydroxyapatite.

No. of measurement	Adhesion strength (MPa)	
	XPT-D-703	PYRO 4
1	12,37	21,44
2	14,45	26,76
3	13,89	25,69
4	16,77	23,12
5	15,28	24,81

As it is derived from the table above, the adhesion strength was generally greater for the PYRO 4 coating, in all five measurements and it fluctuated from 0,38 times the adhesion strength of the XPT-D-703 coating during the fourth measurement to 0,85 times during the second and the third measurement. According to the relative responses of each type of material, it is noted that PYRO 4 coating seems to be more adhesive than the XPT-D-703 coating, which comes in agreement with the absence of detachment crack at the coating-substrate interface of specimens No. 2 and No. 4.

CHAPTER 5: CONCLUSIONS

In this study, coatings prepared with commercial hydroxyapatite powder and nanostructured hydroxyapatite powder were produced through plasma spray process onto stainless steel 304 and tested concerning their structure and properties.

First of all, regarding their mechanical properties, it is mentioned that surface roughness and microhardness values were kept within the acceptable limits for all the specimens. In particular, sample No. 4 that was sprayed with PYRO 4 powder, presented the highest values for all roughness parameters. Amongst these parameters, Ra (arithmetical mean deviation of profile) was found to be 10,26 μm (measurement acquired with TR-100 roughness tester), the same with the respective roughness parameter values that accompany medical implants already accommodated on the market ($\approx 10 \mu\text{m}$). Microhardness values ranged between 2,27 and 2,73 GPa and were practically the same for all the specimens.

In addition, all specimens presented bioactivity behavior after immersion into the simulated body fluid (SBF) solution, for seven consecutive days at 40 °C. A noticeable thin layer of reaction products was detected on top of the coatings after examination with the optical microscope, while the formation of new apatite phase on the surface of the coatings was observed via scanning electron microscopy. Overall coating thickness of the samples was decreased, except for specimen No. 4, in which it was increased.

Moreover, specimen No. 4 maintained satisfying crystallinity after plasma spraying, in relation to the crystallinity of the starting PYRO 4 powder. This is shown by the relative X-ray diffraction spectra, in which the intensity of the diffracted X-rays of PYRO 4 sprayed powder and specimen No. 4 are in close proximity (940 and 900 counts respectively) and thus, crystallinity levels are close. This characteristic also contributes to the abovementioned increase in the overall coating thickness of specimen No. 4, as lower dissolution rates are noted on account of the high level of crystalline HAP present on the coating.

Furthermore, specimens No. 2 and No. 4 managed better adhesion results than the ones prepared with the commercial HAP powder. This is verified by both SEM and adhesion strength test results. During SEM examination the coating-substrate interface of specimens No. 2 and No. 4 appeared to be clear with no precipitated impurities left from either the cutting or the grinding process. Both these coatings, were also characterized by homogeneity in their thickness and consistency in their thickness and in their length, as well. Adhesion strength of the PYRO 4 coating was as much as 0,85 times greater the adhesion strength of the XPT-D-703 coating.

Specimen No. 4 bears the greater amount of porosity, compared to the rest of the samples. This statement is confirmed by both image analysis, which resulted in about 34,8 % “closed porosity” and also mercury porosimetry, which estimated “open porosity” content to be at around 0,6 %. Elevated porosity content occurs due to lower spray power utilized during preparation of specimen No. 4, which consequently results in inadequate melting of the as sprayed particles, formation of pores and voids throughout the coating material and thus, increase in the porosity content.

Generally, it has been reported that a larger pore size and higher porosity (between 46.2% and 46.9%) [97] of the scaffold result in greater bone ingrowth, by enhancement of effective nutrient supply, gas diffusion and metabolic waste removal, but leads to low cell attachment and therefore degradation of mechanical properties [17], [76]. Based on previous studies, a minimum recommended pore size is 100 μm [98]. However, better

osteogenesis results have been reported in scaffolds with pore sizes greater than 300 μm . Tabulated below are the most important values that resulted from the above work.

Table 23: Comparative table of porosity and pore diameter values, between theoretical prerequisite values and those of the four specimens.

Characteristic	Theoretical values	Specimen No. 1	Specimen No. 2	Specimen No. 3	Specimen No. 4
Porosity (%)*	40-65	10	6,4	20,3	34,8
Pore diameter (μm)*	100-300	7,2	6,2	8,7	10,7

* Porosity and pore diameter results presented above for specimens No. 1-4, are those acquired via image analysis.

Taking into consideration the information provided in table 23 it is concluded that the specimens examined did not achieve adequate porosity content, neither pore diameter in order to be used as orthopedic implants, according to the literature.

REFERENCES

- [1] B.D. Ratner, "A History of Biomaterials", in Biomaterials Science (Third Edition): An Introduction to Materials in Medicine, B.D. Ratner, A.S. Hoffman, F.J. Schoen and J.E. Lemons (eds.), 2013, pp. xli–liii, <http://dx.doi.org/10.1016/B978-0-08-087780-8.00154-6>
- [2] M. Navarro et al. / J. R. Soc. Interface 5 (2008) 1137-1158, doi:10.1098/rsif.2008.0151
- [3] L.L. Hench and J.M. Polak / Science 295 (5557) (2002) 1014-1017, DOI: 10.1126/science.106740
- [4] K. Alvarez and H. Nakajima / Materials 2 (3) (2009) 790-832, doi:10.3390/ma2030790
- [5] Liliana do Carmo dos Santos Grenho, "Nanohydroxyapatite-based antibacterial surfaces to prevent biofilm associated biomaterials bone infection" (PhD Thesis), Retrieved from <https://repositorio-aberto.up.pt/bitstream/10216/78773/2/114711.pdf>
- [6] C. Tkaczyk and M. Tabrizian, "Biocompatibility, Metals Ions, and Corrosion Products", in Materials for Medical Devices, ASM HandBook 23, ASM International, Materials Park OH, 2012, p. 47
- [7] J.L. Aranda et al. / European Journal of Cardio-Thoracic Surgery (2015) 1-3, doi:10.1093/ejcts/ezv265
- [8] C.B. Carter, M.G. Norton, "Ceramics in Biology and Medicine", Ceramic Materials: Science and Engineering, Springer, 2007, p.635
- [9] K.C. Dee, D.A. Puleo, R. Bizios, "Biomaterials", An Introduction To Tissue- Biomaterial Interactions, 2002, p. 8-12
- [10] T. Albrektsson and C. Johansson / Eur Spine J 10 (2001), 96-101, doi:10.1007/s005860100282
- [11] Eun-Jung Lee, Hae-Won Kim, and J.C. Knowles, "Ceramic Biomaterials as Tissue Scaffolds", in Stem Cell Biology and Tissue Engineering in Dental Sciences, A. Vishwakarma, P. Sharpe, S. Shi and M. Ramalingam (eds.), 2015, p. 164
- [12] P. Růžička, Fused Deposition Modeling technology, Rapid Prototyping Laboratory, The Laboratory of Biomechanics, <http://www.biomechanika.cz/departments/21>
- [13] M.F. Maitz / Biosurface and Biotribology 1 (2015) 161-176
- [14] M.M. Robbins, A.R. Vaccaro and L. Madigan / Neurosurg Focus 16 (3) (2004) 1-7, <http://thejns.org/doi/pdf/10.3171/foc.2004.16.3.2>
- [15] <https://lehighbioe.wordpress.com/2014/11/17/metals-in-artificial-joints/>
- [16] A.L. Boskey / Elements 3 (2007) 387-393
- [17] C. Liu et al. / Acta Biomaterialia 5 (2009) 661-669
- [18] M. Vallet-Regí, J.M. González-Calbet / Progress in Solid State Chemistry 32 (2004) 1-31
- [19] R. Gadov et al. / Surface & Coatings Technology 205 (2010) 1157–1164

- [20] T. Ikoma, A. Yamazaki, S. Nakamura, M. Akao / *Netsu Sokutei* 25 (5) (1998) 141-149
- [21] R.K. Brundavanam et al. / *American Journal of Materials Science* 3 (4) (2013) 84-90
- [22] S. D. Poštić / *International Journal of BioMedicine* 4(2) (2014) 109-113
- [23] N.H. de Leeuw / *Chem. Commun.* (2001) 1646-1647, DOI: 10.1039/b104850n
- [24] L. Calderín, M.J. Stott, and A. Rubio / *PHYSICAL REVIEW B* 67, 134106 (2003), doi: 10.1103/PhysRevB.67.134106
- [25] M. Sadat-Shojai et al. / *Acta Biomaterialia* 9 (2013) 7591-7621
- [26] S. Cox, "Synthesis Method of Hydroxyapatite",
<http://www.mandplabs.com/interface/uploads/files/whitepapers/hydroxyapatite-white-paper.pdf>
- [27] V.P. Orlovskii et al. / *Inorganic Materials* 38 (10) (2002) 973-984
- [28] A.K. Nayak / *Int. J. Chem Tech Res.* 2 (2) (2010) 903-907
- [29] S. Mann, *Biomaterialization: Principles and Concepts in Bioinorganic Materials Chemistry*, Oxford University Press, New York, 2001
- [30] J.J. De Yoreo and P.G. Vekilov, "Principles of Crystal Nucleation & Growth", in *Biomaterialization*, P.M. Dove, J.J. De Yoreo and S. Weiner (eds.), Mineral Soc. Am., Washington, DC, 2003, pp. 57-93,
<http://eps.mcgill.ca/~jeanep/eps/EPSC644/Principles%20Of%20Nucleation%20And%20Growth.pdf>
- [31] T.J. Webster et al. / *Biomaterials* 21 (2000) 1803-1810
- [32] S.J. Kalita et al. / *Materials Science and Engineering C* 27 (2007) 441-449
- [33] J.L. Xu et al. / *Materials Science and Engineering A* 374 (2004) 101-108
- [34] B.J. McEntire et al. / *Journal of the European Ceramic Society* 35 (2015) 4327-4369
- [35] Y. Cai et al. / *J. Mater. Chem.* 17 (2007) 3780-3787, DOI: 10.1039/b705129h
- [36] M. Rouahi et al. / *Colloids and Surfaces B: Biointerfaces* 47 (2006) 10-19
- [37] S. Bose, S.K. Saha / *J. Am. Ceram. Soc.* 86 (6) (2003) 1055-1057
- [38] L. Pawlowski, *The Science and Engineering of Thermal Spray Coatings: Second Edition*, John Wiley & Sons, Ltd, 2008, DOI: 10.1002/9780470754085,
<http://ftp.demec.ufpr.br/disciplinas/EME715/Artigos%20para%20Semin%C3%A1rio/John%20Wiley%20&%20Sons%20-%20Science%20and%20Engineering%20of%20Thermal%20Spray%20Coatings%20-%202nd%20Editon%20-%202008.pdf>
- [39] <http://mswebs.naist.jp/LABs/tanihara/ohtsuki/SBF/>
- [40] T. Kokubo, H. Takadama / *Biomaterials* 27 (2006) 2907-2915
- [41] H. Qu and M. Wei / *Journal of Biomedical Materials Research Part B: Applied Biomaterials* (2008) 204-212, DOI: 10.1002/jbm.b.31096

- [42] K. Kulpechdara et al. / Surface & Coatings Technology (2016)
- [43] <http://durametal-alloy.com/technical-resources/thermal-spray-principles-and-techniques>
- [44] A. Wank, Basics of Thermal Spray Technology: 1. Processes, GTV Verschleiss-Schutz GmbH, Luckenbach, Germany, p. 11, http://www.gtv-mbh.com/old/gtv-mbh-englisch/www.gtv-mbh.de/cms/upload/publikat/Wank/thermal_spray_basics_processes.pdf
- [45] Oerlikon Metco, Atmospheric Plasma Spray Solutions, Issue 5, 2014, <https://www.oerlikon.com/metco/en/products-services/coating-equipment/thermal-spray/processes/atmospheric-plasma/>
- [46] B. León and J.A. Jansen, "Introduction", Thin Calcium Phosphate Coatings for Medical Implants, B. León and J.A. Jansen (eds.), Springer, 2009, pp. 2-3
- [47] <https://www.oerlikon.com/metco/en/products-services/coating-services/coating-services-thermal-spray/thermal-spray-processes/processes-atmospheric-plasma/>
- [48] <http://www.flamesprayusa.com/plasma-spray-coating.php>
- [49] D.E. Crawmer, "Coatings, Equipment, and Theory", in Thermal Spray Technology, ASM HandBook, ASM International, Materials Park OH, 2004
- [50] <https://www.oerlikon.com/metco/en/products-services/coating-services/coating-services-thermal-spray/thermal-spray-processes/processes-controlled-atmospheric-plasma/>
- [51] <http://www.fst.nl/systems/hvof/>
- [52] <https://www.oerlikon.com/metco/en/products-services/coating-services/coating-services-thermal-spray/thermal-spray-processes/processes-hvof-gas-fuel/>
- [53] <https://www.oerlikon.com/metco/en/products-services/coating-services/coating-services-thermal-spray/thermal-spray-processes/processes-hvof-liquid-fuel/>
- [54] Moridi et al. / Surface Engineering 36 (6) (2014) 369-395, http://www.mit.edu/~mingdao/papers/2014_Surf_Eng_Moridi_cold_spray_coating_review.pdf
- [55] <http://csp-world.com/news/20150120/001870/irelands-trinity-college-dublin-research-cold-spray-metal-3d-printing-funded>
- [56] D.H. Barnes, A. Moavenian, A. Sharma, and S.M. Best, "Biocompatibility of Ceramics", in Materials for Medical Devices, ASM HandBook 23, ASM International, Materials Park OH, 2012, pp. 129-130
- [57] S. Chandra, P. Fauchais / J Therm Spray Tech 18 (2) (2009) 148-180, doi:10.1007/s11666-009-9294-5
- [58] H. Li et al. / Biomaterials 25 (2004) 3463-3471, doi:10.1016/j.biomaterials.2003.10.051
- [59] P. Fauchais and A. Vardelle / J. Phys. D: Appl. Phys. 44 (2011), pp. 14, doi:10.1088/0022-3727/44/19/194011
- [60] H. Liu et al. / J. Phys. D: Appl. Phys. 26 (1993) 1900-1908

- [61] S. Sampath, X. Jiang / *Materials Science and Engineering: A* 304-306 (2001) 144-150
- [62] M. Pasandideh-Fard et al. / *Journal of Thermal Spray Technology* 11 (2) (2002) 206-217
- [63] K. Alamara et al. / *Surface & Coatings Technology* 206 (2011) 1180-1187, doi:10.1016/j.surfcoat.2011.08.020
- [64] <http://www.plasmapowders.com/thermal-spray-porosity.htm>
- [65] S.A. Hacking et al. / *Clinical Orthopaedics and Related Research* 405 (2002) 24–38, DOI: 10.1097/01.blo.0000038469.05771.3d
- [66] H. Zeng et al. / *Biomaterials* 20 (1999) 377-384
- [67] G. Mabilieu and A. Sabokbar, chapter 7: “In vitro biological test methods to evaluate bioresorbability”, in *Degradation rate of bioresorbable materials-Prediction and evaluation*, Fraser J. Buchanan (ed.), Woodhead Publishing Limited, Cambridge, England
- [68] D.D. Deligianni et al. / *Biomaterials* 22 (2001) 87-96
- [69] M. Vandrovcová and L. Bačáková / *Physiol. Res.* 60 (2011) 403-417
- [70] S. Hansson, M. Norton / *Journal of Biomechanics* 32 (1999) 829-836
- [71] TwinSys® The hydroxylapatite coating, Mathys European Orthopaedics, Mathys Ltd Bettlach,
http://www.mathysmedical.com/Storages/User/Dokumente/Produktinfo/Huefte/Produktinfo_twinSys_E_V02.pdf?
- [72] P. Cheang and K.A. Khor / *Biomaterials* 17 (5) (1996) 537-544
- [73] A.S. Kang et al. / *International Journal of Surface Engineering & Materials Technology* 3 (1) 2013, ISSN: 2249-7250, <http://www.ptujournals.ac.in/PublishedJournals/Journal10.pdf>
- [74] L. Sun et al. / *J. Biomed. Mater. Res.* 62 (2) (2002) 228–236
- [75] S.R. Radin, P. Ducheyne / *JOURNAL OF MATERIALS SCIENCE: MATERIALS IN MEDICINE* 3 (1992) 33-42
- [76] V. Karageorgiou, D. Kaplan / *Biomaterials* 26 (2005) 5474-5491
- [77] <https://griekspoorthermalcoatings.com/en/theory>
- [78] L. Sun et al. / *Materials Science and Engineering A360* (2003) 70-84, doi:10.1016/S0921-5093(03)00439-8
- [79] H. Li, K.A. Khor / *Surface & Coatings Technology* 201 (2006) 2147-2154, doi:10.1016/j.surfcoat.2006.03.024
- [80] S.M. Maisara et al. / *IPCBE* vol.7 (2011), 2011 2nd International Conference on Biotechnology and Food Science, Singapore
- [81] D.N. Ungureanu, N. Angelescu, R.M. Ion, E.V. Stoian, C.Z. Rizes, Conference paper: “Synthesis and Characterization of Hydroxyapatite Nanopowders by Chemical Precipitation”, *Recent Researches in Communications, Automation, Signal Processing, Nanotechnology, Astronomy and Nuclear Physics*, 2011,

https://www.researchgate.net/publication/262322346_Synthesis_and_characterization_of_hydroxyapatite_nanopowders_by_chemical_precipitation

[82] J.M. Zielinski and L. Kettle, "Physical Characterization: Surface Area and Porosity", Intertek Chemicals and Pharmaceuticals (2013),

http://s3.amazonaws.com/academia.edu.documents/44969140/IntertekWhitepaper_Surface_Area_and_Porosity_Chemicals170613.pdf?AWSAccessKeyId=AKIAIWOWYYGZ2Y53UL3A&Expires=1494286775&Signature=FI50LSwi0jL6P5jWKwKDgVB4hk%3D&response-content-disposition=inline%3B%20filename%3DIntertekWhitepaper_Surface_Area_and_Poro.pdf

[83] H. Giesche / Part. Part. Syst. Charact. 23 (2006) 9-19, doi: 10.1002/ppsc.200601009

[84] Ilavsky et al. / J. Am. Ceram. Soc., 80 (3) (1997) 733-742

[85]

<https://www.udri.udayton.edu/nonstructuralmaterials/coatings/pages/astmd4541standardtestmethodforpull-offstrengthofcoatingsusingportableadhesiontesters.aspx>

[86] L.S. Ozyegin et al. / Materials Letters 58 (2004) 2605-2609

[87] M. Akmal et al. / Ceramics International 41 (2015) 14458-14467

[88] J. Matejicek and S. Sampath / Acta mater. 49 (2001) 1993-1999

[89] R.S. Lima and B.R. Marple / Journal of Thermal Spray Technology 16 (1) (2007) 40-63, DOI: 10.1007/s11666-006-9010-7

[90] M. Magallanes-Perdomo et al. / Journal of the European Ceramic Society 31 (2011) 1549-1561

[91] J.N. Barry and D.P. Dowling / Key Engineering Materials 493-494 (2012) 483-488, doi:10.4028/www.scientific.net/KEM.493-494.483

[92] A. Cattini et al. / Surface & Coatings Technology 240 (2014) 110 -117

[93] M. Mittal, S.K. Nath, S. Prakash / Journal of Minerals & Materials Characterization & Engineering 10 (11) (2011) 1041-1049

[94] G. Song and S. Song / Advanced Engineering Materials 9 (4) (2007) 298-302, DOI: 10.1002/adem.200600252

[95] K.A. Khor, P. Cheang / Journal of Materials Processing Technology 63 (1997) 271-276

[96] S. Pramanik, A.K. Agarwal, and K.N. Rai / Trends Biomater. Artif. Organs 19 (1) (2005) 46-51

[97] R. Obregón et al. / Chapter 13 - Gradient Biomaterials as Tissue Scaffolds, Stem Cell Biology and Tissue Engineering in Dental Sciences, Editors: Ajay Vishwakarma, Paul Sharpe, Shi Songtao and Murugan Ramalingam, 2015, p. 179

[98] S. F. Hulbert et al. / J Biomed Mater Res 4 (3) (1970) 433-456

CURRICULUM VITAE

Paraskevi Gkomoza

Tsourouktsoglou 11
Dafni-Imittos, 17237
Athens
(+30) 210-9735880
gomozae@yahoo.gr

PERSONAL PROFILE

- Extensive knowledge in the preparation and analysis of metal samples
- Ability of overall assessment of a problem
- Ability to work effectively under pressure to meet deadlines
- Ability to communicate with collaborating team members to deliver optimal results

EDUCATION

2015-today **National Technical University of Athens (NTUA), School of Chemical Engineering**
Interdisciplinary Interdepartmental Postgraduate Program (IIPP)
“Materials Science and Technology”

Master Thesis: *Comparative study of structure and properties of thermal spray coatings using conventional and nanostructured Hydroxyapatite powder, for applications in medical implants.*

2010-2015 **University of Thessaly, School of Engineering, Department of Mechanical Engineering**
Diploma Mechanical Engineering – Graduation Grade: 7.42/10 (“Very Good”)
Specialization in Mechanics, Materials & Manufacturing Processes

Diploma Thesis: *Mechanisms of Corrosion in petroleum refineries.*

2004-2010 ***2nd Gymnasium and Lychee of Imittos – Graduation Grade: 19.1/20***

WORK EXPERIENCE

2014-2014 **Technical Office “Giannis Sakellaridis and Colleagues”**
Training internship of two months in the framework of the compulsory exercise for the acquisition of a Diploma in Mechanical Engineering from the Department of Mechanical Engineering of the University of Thessaly.

- Fire safety studies
- Occupational risk assessment

ADDITIONAL SKILLS AND ACHIEVEMENTS

COMPUTER SKILLS

FORTRAN, MATLAB, Mathematica, LINGO, AutoCAD, Windows, Word, Excel, Power Point

LANGUAGES

Greek (Native Language), English (C2) – Michigan Proficiency

DRIVING LICENCE

2011 European Driving License, Category B

CONFERENCES

2016 German-Greek Workshop 2016 “Nano-structured soft materials: from polymer self-assembly to stimuli responsive materials”, National Technical University of Athens, Athens

2015 “1st Workshop on Fatigue of Materials used in Vascular Surgery”, University of Thessaly, Volos

2015 “1st Conference on Fatigue of Materials used in Vascular Surgery”, University of Thessaly, Volos

2014 “Workshop in Integrated Computational Materials Engineering (ICME)”, University of Thessaly, Volos

2013 “5th Conference of Metallic Materials”, held by the Lab of Materials of the Department of Mechanical Engineers and the Greek Metallurgical Company, Volos

2011 Awareness Workshop on "Energy Studies - Energy Inspection", University of Thessaly, Volos

MEMERSHIPS AND INTERESTS

2001-2013 & 2016-2016 Piano lessons

2007-today Member of choir “Cantus non verba”

2001-2005 Painting lessons